TABLE OF CONTENTS

Page

iii

TABLE OF CONTENTS (cont'd)

Page

NASA Contractor Report 2992

Experimental Investigation of Outdoor Propagation of Finite-Amplitude Noise

Don A. Webster and David T. Blackstock

NASA

NASA Contractor Report 2992

Experimental Investigation of Outdoor Propagation of Finite-Amplitude Noise

Don A. Webster and David T. Blackstock
The University of Texas at Austin
Austin, Texas

NASA

National Aeronautics
and Space Administration

**Scientific and Technical
Information Office**

1978

Blank Page

A series of experiments on outdoor propagation of high intensity sound is described in this report. Begun in 1975, the research was carried out in two phases. Phase I, on intense acoustic tones, was completed in 1976. Phase II, on intense noise, was finished in 1977. The report is primarily devoted to Phase II, but a review of Phase I is included.

Cosponsors of the research along with NASA were Air Force Office of Scientific Research, National Oceanic and Atmospheric Administration, and Office of Naval Research.

SUMMARY

A series of experiments have been carried out on the propagation of finite-amplitude noise outdoors. The purpose of the study was to determine the extent to which nonlinear effects influence the propagation of noise from a controlled source in the outdoor environment. A secondary purpose was to develop, if possible, a theoretical model for the noise propagation. A ground-mounted electroacoustic source transmitted broadband, octave band, or 1/3 octave band noise in the frequency range 2-10 kHz. The source level (overall sound pressure level) of the noise was in the range 121-145 dB re 20 μPa at 1 m. The propagation path was vertical and parallel to an 85 m tower, whose elevator carried the traveling microphone. The maximum propagation distance was about 80 m. The experiments were done at night during the months June through September 1977. The meteorological conditions (ground level) were as follows: temperature range 23-31°C, relative humidity range 55-90%, and wind speed range 0-24 km/h.

The measurements were compared with theoretical predictions based on linear theory. Spherical spreading, atmospheric attenuation, and, as appropriate, source diffraction were accounted for in these predictions. Predictions based on nonlinear theory were also attempted, but the particular model was based on an assumption about the noise distortion in the transmitter nearfield. As it turned out, this assumption was not justified in our experiments.

Use of an amplitude-frequency scaling law made it possible to compare the noise from our experiments with noise from a KC-135A aircraft. The importance of nonlinear effects in actual jet noise could thus be estimated.

The primary conclusions are as follows:

1.   A strong generation of high frequency noise caused by nonlinear effects was found in all the high intensity noise experiments. A very limited amount of low frequency noise was also generated. The intense, middle part of the spectrum deviated little if any from expectations based on linear theory. These observations indicate that although shocks formed in the noise waveform, distortion did not reach the stage at which shock merging was important.

2.   The spectral distortion occurred in both the transmitter nearfield and farfield. Moreover, the distortion in the nearfield was over and above the spectral changes associated with diffraction.

3.   At no measurement point was small-signal behavior established for the high frequency noise. Theoretical calculations for tone signals support the proposition that the nonlinearly generated high frequency noise never achieves a farfield where small-signal behavior is established.

4.   Comparison of the measured spectra with predictions from a model based on nonlinear theory showed poor agreement for the high frequency noise. The failure of our predictions was not due to an error in the nonlinear theory per se, but rather due to an inadequate description of the source noise waveform. In the future, use of a directly recorded input waveform should be tried.

5.   Comparison of our scaled experimental measurements with actual jet spectra show that the spectrum levels encountered in our experiments are well within the jet noise range. Indeed, the noise

measured from a KC-135A jet is roughly 10 dB higher in spectrum level than our scaled noise. One therefore concludes that nonlinear effects are probably common in jet noise.

The report also contains some information about outdoor propagation of finite-amplitude tones. Tone experiments done as a forerunner to those on noise are reviewed. Additional data on tones taken during the course of the noise study are also described. Theoretical analyses of propagation of very weak and very strong tones are presented.

CHAPTER 1

INTRODUCTION

Experiments done outdoors on the propagation of intense acoustic noise
are the subject of this report. These experiments constitute Phase II of a
research program begun in June 1975 to study outdoor propagation of finite-
amplitude acoustics waves, that is, sound so intense that nonlinear
effects are important. The ultimate application of the research is to jet
aircraft noise. In particular, the goal has been to determine whether
aircraft noise is affected by nonlinear propagation distortion. The
propagation experiments were carried out along an 85 m vertical path
parallel to a radio tower; the source was on the ground. The first phase
of the program, Phase I, was done with intense tones as a means of preparing
for the noise experiments (Phase II), which were expected to be more
difficult. Important nonlinear effects--harmonic distortion, shock formation,
extra attenuation, and an interaction between diffraction and distortion--
were observed in Phase I.[1,2] A review is given in Chapter 2. Because of
the success of the tone experiments, it was decided to proceed with Phase II.
The results are reported here.

Previous investigations of finite-amplitude noise have been largely
limited to plane waves in tubes[3-8] or to strictly theoretical calculations.[9-12]
Pernet and Payne[3-5] used a plane wave tube to measure the spectral distortion
of 1/3 octave and octave bands of cw noise (and, in one experiment, a 2.3
octave band). The sound pressure level (SPL) at the source was as high as
140 dB (re 20 μPa). They observed second and higher harmonic bands of
noise that grew and decayed with distance according to their theoretical
predictions. Later, through both theory and experiment, they showed that
the second harmonic band has an amplitude distribution quite different from

4

that of the fundamental noise band.[8] Pestorius[6,7]

also made noise propagation measurements in a plane wave tube but used generally wider bandwidths and much higher SPL's, up to 160 dB. In the main his noise was pulsed, not cw. Although we shall presently review his results in detail, it may be noted here that because Pestorius's intensity was greater than Pernet and Payne's, the low frequency end of the spectrum grew substantially as well as the high frequency end. Viewed in the time domain, the propagating noise pulse was observed to distort into a random sawtooth wave. A computer algorithm based on weak-shock theory (with modifications to account for tube wall attenuation and dispersion) was used to obtain theoretical predictions. The predictions agreed well with the experimental measurements. Later Pestorius's algorithm was extended to cover spherical and other nonplanar waves.[13] An attempt was then made to use the generalized algorithm to predict the nonlinear distortion of actual jet noise.[14] A sample of noise recorded close to a jet engine was used as the input to the computer program, and the subsequent distortion of the noise signal with distance was calculated. Although the calculation did show the importance of nonlinear effects, the study was somewhat artificial because many factors affecting the propagation of jet noise in the field--atmospheric attenuation and meteorological effects, ground reflection and absorption, and effects due to the spatial extent and moving source nature of the jet--were not included in the algorithm.

In the meantime, the Russian investigators have been very active on the theoretical front.[9-12] They have frequently employed methods developed in nonlinear statistical optics.[15] A review of their work on several topics in nonlinear distortion of random waves is given in Chap. 10 of Ref. 10. In general it is assumed that the initial spectral distribution of the noise

and its statistics are known. For several reasons it has been difficult to apply the Russian results on broadband noise to our experiments.

The previous research is sufficient to permit a qualitative description of the effect of nonlinearity on noise propagation. The propagation speed of a finite-amplitude wave is

$$\frac{dx}{dt} = c_o + \beta u \quad , \tag{1-1}$$

where c_o is the small-signal sound velocity, β is the coefficient of nonlinearity [for gases $\beta = (\gamma +1)/2$, where γ is the ratio of specific heats], and u is the particle velocity. Because of its dependence on u, the propagation speed varies from point to point on the wave. The wave therefore distorts as it travels. The compression phases of the wave steepen, and the slopes of the expansion phases become more gentle (see, for example, Fig. 7-1). Unless the smoothing effect of ordinary absorption is stronger than the steepening effect, shocks eventually form in the waveform. The result is illustrated in Fig. 1-1, which is a sequence of time waveforms (measured on the left, computed on the right) of a very intense noise pulse as it propagates down a plane wave tube.[6,7] In the first stage of the distortion process, many shocks form as a result of the overtaking of troughs by peaks; see the 12 ft waveform in Fig. 1-1. After most of the shocks have formed, the distortion process continues but in a qualitatively different way. Because each shock has its own particular propagation speed, which is determined by its peak and trough pressures, the shock positions in the waveform slowly change as the wave continues to propagate. As the shocks advance or retreat relative to their neighbors, merging takes place: the big shocks tend to "eat up" the little shocks. The noise waveform becomes simpler in appearance because the number of zero crossings is reduced.
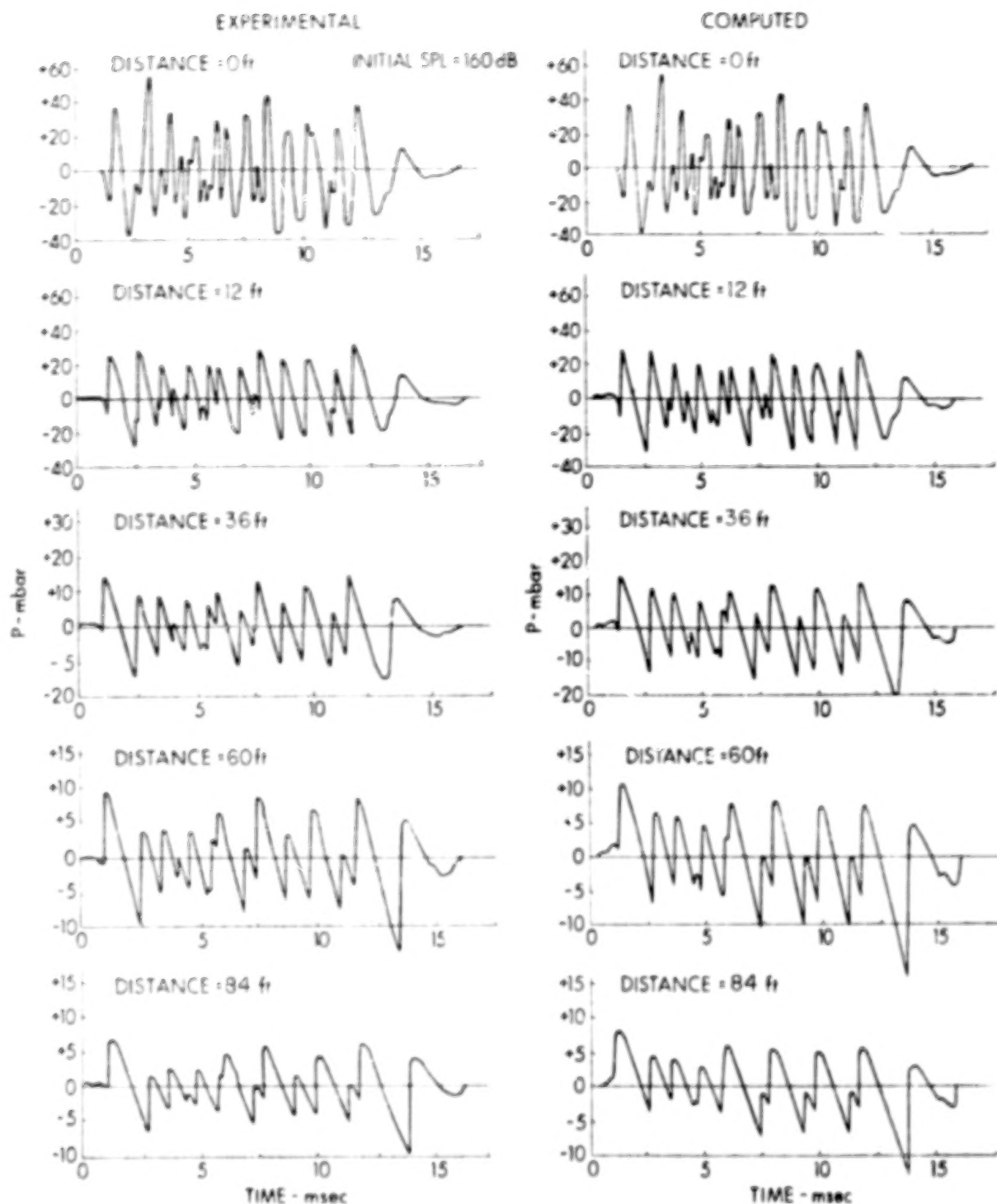
FIGURE 1-1
NOISE PULSE 1 AT VARIOUS DISTANCES

(Taken from Ref. 6; 1 ft = 0.3048 m)

For example, in Fig. 1-1 the propagation from 12 ft to 84 ft is marked by a 30% reduction in number of zero crossings. In summary, the distortion of the noise waveform has two relatively distinct stages. In Stage I shocks form but the number of zero crossings does not change very much. In Stage II shock merging occurs; accordingly the number of zero crossings is reduced.

The two stages also have markedly different properties in the frequency domain. The formation of shocks (Stage I) is accompanied by a strong growth of the high frequency end of the spectrum. In Stage II the merging of shocks, which reduces the average time between zero crossings, is associated with appreciable growth of the low-frequency end of the spectrum. (There is, of course, some low frequency energy produced during Stage I as a result of intermodulation distortion. The difference frequency component is normally generated much less efficiently, however, than the sum-frequency and harmonic components. Distortion in Stage I is therefore manifested primarily by high frequency development.) The growth at both ends of the spectrum comes, of course, at the expense of the spectral middle. Figure 1-2, which shows the results of an experimental measurement made by Pestorius with cw noise,[6,7] illustrates the phenomenon. If either of the downstream spectra (48 ft or 72 ft) is subtracted from the source spectrum (0 ft), the result is the apparent attenuation as a function of frequency. The attenuation is negative at low and high frequencies. In the midfrequency range the attenuation is much greater than it would have been had the noise been small-signal.

Note that Stage II in the distortion process is not realized unless the noise has a very high intensity. At lower intensities, as in the Pernet-Payne experiments, "steepening" type distortion (Stage I) develops
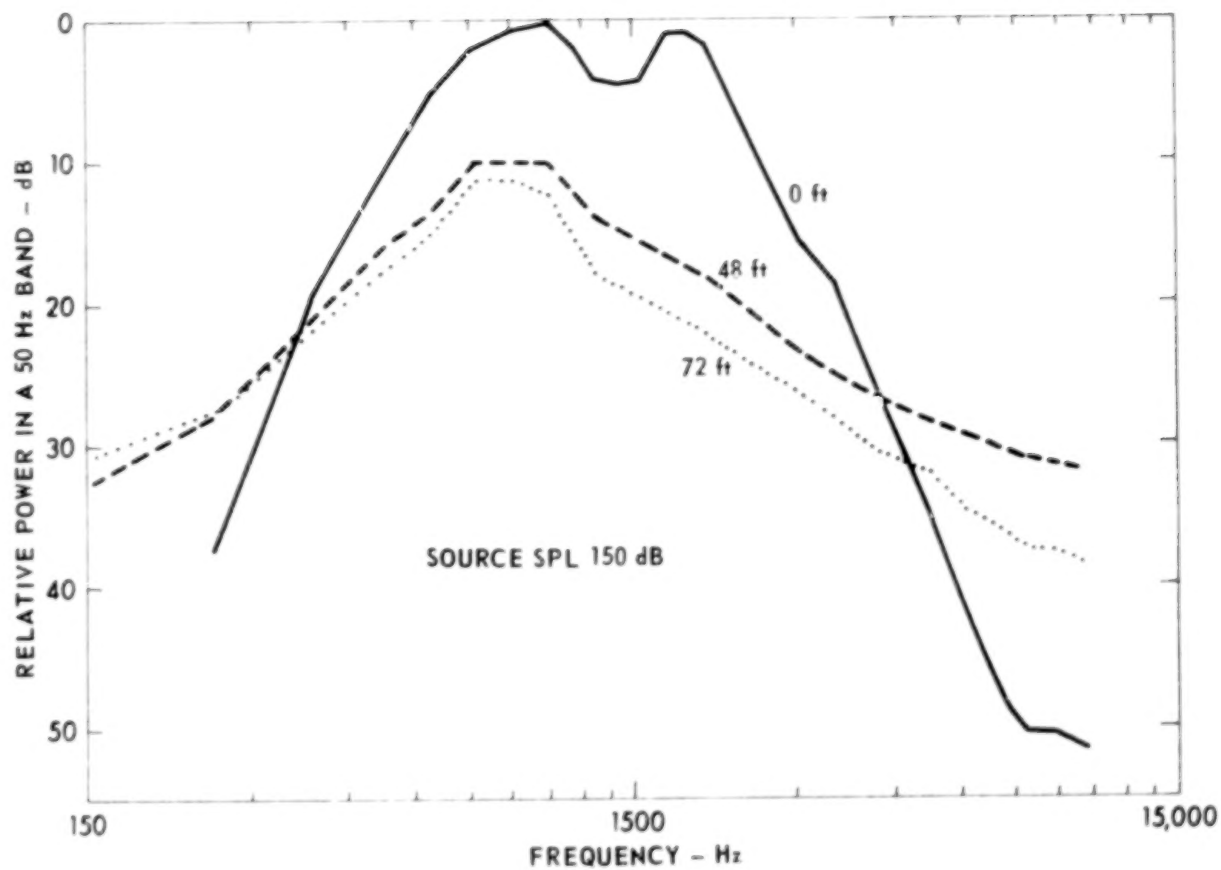
8

FIGURE 1-2
MEASURED NOISE SPECTRUM AT VARIOUS DISTANCES
(Taken from Ref. 6; 1 ft = 0.3048 m)

relatively slowly. Ordinary absorption then has ample time to exercise
its smoothing effect on the waveform. When this happens, the distortion
process slows down and eventually stops while still in Stage I. Stage II
is never reached.

What modifications to our picture of noise distortion might the
outdoor environment be expected to introduce? The most noticeable change
is brought about by the shift from plane to spherical waves. The amplitude
reduction caused by spherical spreading slows down the distortion process
considerably.[13] Thus Stage I, which lasted only a few feet in Pestorius's
plane wave experiments, is expected to stretch out over a much greater
distance when the noise is a spherical wave. As we have already seen,
ordinary absorption opposes the steepening distortion process directly.
Absorption and spherical spreading thus work in combination against the
realization of State II distortion. In fact, except for exceedingly
powerful noise sources, one may expect spectral distortion of outdoor
noise to be limited to high-frequency buildup.

Another feature of the outdoor environment that might be expected to
affect distortion of finite-amplitude noise is random inhomogeneity of the
medium (random variation in wind and temperature). Our experience in Phase I,
however, was that while random inhomogeneity definitely affected the
instantaneous time waveform of the received signal, it had little or no
residual effect on the long term average spectral content of the signal.
Random inhomogeneity would not be expected to affect finite-amplitude
noise any differently.

The attenuation properties of nonlinearly generated high-frequency
noise may be expected to differ from those of small-signal noise of the
same frequency. In studies of plane periodic waves of finite amplitude in

10

dissipative media (see, for example Refs. 3, 5), it has been found for a wide variety of cases that at great distance the second harmonic component decays asymptotically as $\exp(-2\alpha_1 x)$, not as $\exp(-\alpha_2 x)$, where α_1 and α_2 are the small-signal attenuation coefficients at the fundamental and second harmonic frequencies, respectively. Since generally $2\alpha_1 < \alpha_2$, this means that the nonlinearly generated second harmonic component decays more slowly than might have been expected from linear theory. Moreover, no distance is ever reached at which the second harmonic does decay as $\exp(-\alpha_2 x)$, i.e., as a small signal. This peculiar behavior is a result of the way the second harmonic sound is generated. It is produced not back at the source but by nonlinear interaction that takes place over the entire travel path between source and observation point. Furthermore, the third harmonic component is found to decay asymtotically as $\exp(-3\alpha_1 x)$, not $\exp(-\alpha_3 x)$, and the higher harmonics behave similarly. In other words the higher harmonic sound never establishes a propagation region in which traditional small-signal absorption laws take over.

How does this peculiar propagation behavior apply to aircraft noise? Although the decay laws for spherical waves are different from those for plane waves (see Appendix A and Eqs. 2-3 and 2-4 in Chapter 2), it still turns out that nonlinearly generated higher harmonics decay less rapidly than small-signal sound of the same frequency. This means that although high frequency aircraft noise generated at the source decays according to small-signal laws, high frequency noise generated nonlinearly in the course of propagation decays less rapidly. As distance from the source increases, at first the small-signal portion of the high frequency noise masks the nonlinearly generated portion. At sufficiently great distances, however,

on y the nonlinearly generated portion survives, and it does not decay at the rate expected from small-signal theory. Whether this effect is important in practice depends on the distance and amplitude at which the nonlinearly generated portion becomes dominant. It does seem clear, however, that the commonly held belief that nonlinear effects in aircraft noise may be ignored past a given distance is at best an oversimplification.

Although this report is primarily devoted to experiments on high intensity noise, some data on intense tones are also included. As already mentioned, Phase I, which was devoted entirely to tone measurements, is reviewed in Chapter 2. Theoretical analyses to support this review are given in Appendix A. Some tone measurements were also made during the course of Phase II. Data in Appendix C show how SPL of a tone fluctuates with time. Finally, one of the sources used for the noise experiments, the Applied Electro Mechanics (AEM) 20 Driver Loudspeaker Array, was, at the time of our experiments, being evaluated by the Electrical Engineering Department for possible use by the Coast Guard as a fog signaling device. We carried out tests with high-intensity tones as a contribution to the evaluation process. Since the measurements are closely related to those made with noise, the results are included in Appendix D.

The theoretical models used to obtain predictions for comparison with the experimental data are described briefly in Chapter 3. Chapter 4 is devoted to apparatus and procedure. Eleven noise propagation experiments were completed. The data, along with linear theory predictions for comparison, are presented in Chapter 5. The results are analyzed, interpreted, and discussed in Chapter 6. In Chapter 7 an application of the measurements to jet noise is given. Here the most important general technological conclusion of the project

is drawn: nonlinear propagation distortion is apparently important for the noise produced by many jet aircraft. Chapter 8 is a summary.

Certain ancillary results deemed important enough to report are presented in the appendices. As already mentioned, the material in Appendices A, C, and D pertains to tones. Appendix B gives a theoretical analysis of the amplitude density of finite-amplitude noise. It is shown that, prior to shock formation, the amplitude density does not change while the wave undergoes nonlinear propagation distortion.

REVIEW OF PHASE I

In Phase I the outdoor propagation of high-intensity tones was studied. The purpose was to determine the extent to which the outdoor environment, especially random inhomogeneity of the medium, affects nonlinear propagation distortion. Most previous experiments on finite-amplitude propagation in air had been carried out indoors under highly controlled laboratory conditions, either in tubes (see, for example, Ref. 3, 5, and 6 and the earlier works referred to therein) or in anechoic enclosures.[16-18] The outdoor tone measurements were also intended to serve as a stepping stone to similar experiments with intense noise (Phase II).

A.   EXPERIMENT DESIGN, APPARATUS, AND THEORY

   1.   Experiment Design

Propagation distortion in a spherical wave produced by a monochromatic source of radius r_o depends on the source pressure amplitude p_{10}, source frequency $f = \omega/2\pi$, propagation distance r, coefficient of nonlinearity β and ordinary absorption of the medium. When ordinary absorption is not important, the distortion depends only on the following dimensionless combination of factors:[19]

$$\sigma = \beta \epsilon k r_o \ln(r/r_o) \quad , \tag{2-1}$$

which is called the distortion range variable. Here $\epsilon = p_{10}/\rho_o c_o^2$ is the dimensionless source amplitude, ρ_o is the static density, c_o is the small-signal sound speed, and $k = \omega/c_o$ is the wave number. The fact that σ is proportional to the product of source amplitude and frequency gives us a very useful scaling law: if frequency and amplitude are scaled inversely with

respect to each other, all other things being held constant, the amount of nonlinear distortion in the wave (e.g., the percent second-harmonic distortion, percent third-harmonic distortion, etc.) remains the same. When ordinary absorption in the medium is important, the amount of distortion also depends on the dimensionless parameter αr_o, where α is the amplitude attenuation coefficient at the source frequency. Because α depends on frequency, the amplitude-frequency scaling law given above is actually only an approximation. Even so, the law is still very useful for rough design purposes.

For more accurate assessment of the ability of a source to produce finite-amplitude sound, we developed a graphical method based on the values of the two dimensionless parameters $\beta \epsilon k r_o$ and αr_o.[20] See Fig. 2-1, which we call a source-frequency level (SFL) chart. The abscissa is αr_o, and the ordinate is SFL, whose definition is

$$SFL = SPL_{1m} + 20 \log_{10} f_{kHz} \quad (dB \text{ re } 20 \ \mu Pa\text{-}kHz\text{-}m) . \quad (2\text{-}2)$$

In this formula SPL_{1m} is the source level at 1 m (farfield SPL extrapolated to 1 m) and f_{kHz} is the frequency in kHz. Source-frequency level is a convenient measure of $\beta \epsilon k r_o$.[21] The lower curve on the SFL chart represents source operating conditions that lead to a wave whose calculated shock formation distance $\bar{r}$ (found by setting $\sigma = 1$ in Eq. 2-1) is the same as the distance r_{max} beyond which the fundamental is predicted to decay as a small signal. The upper curve is for a much stronger wave, one for which the calculated well-formed sawtooth distance $\hat{r}$ (found by setting $\sigma = 3$ in Eq. 2-1) equals r_{max}. (Formulas for $\bar{r}$, $\hat{r}$, and r_{max} are given, for example, in Ref. 19.) The SFL chart is used as follows: A source whose operating point falls below the lower curve is classified as weak in the sense that its radiation is subject to only weak nonlinear effects. Shock formation is not expected
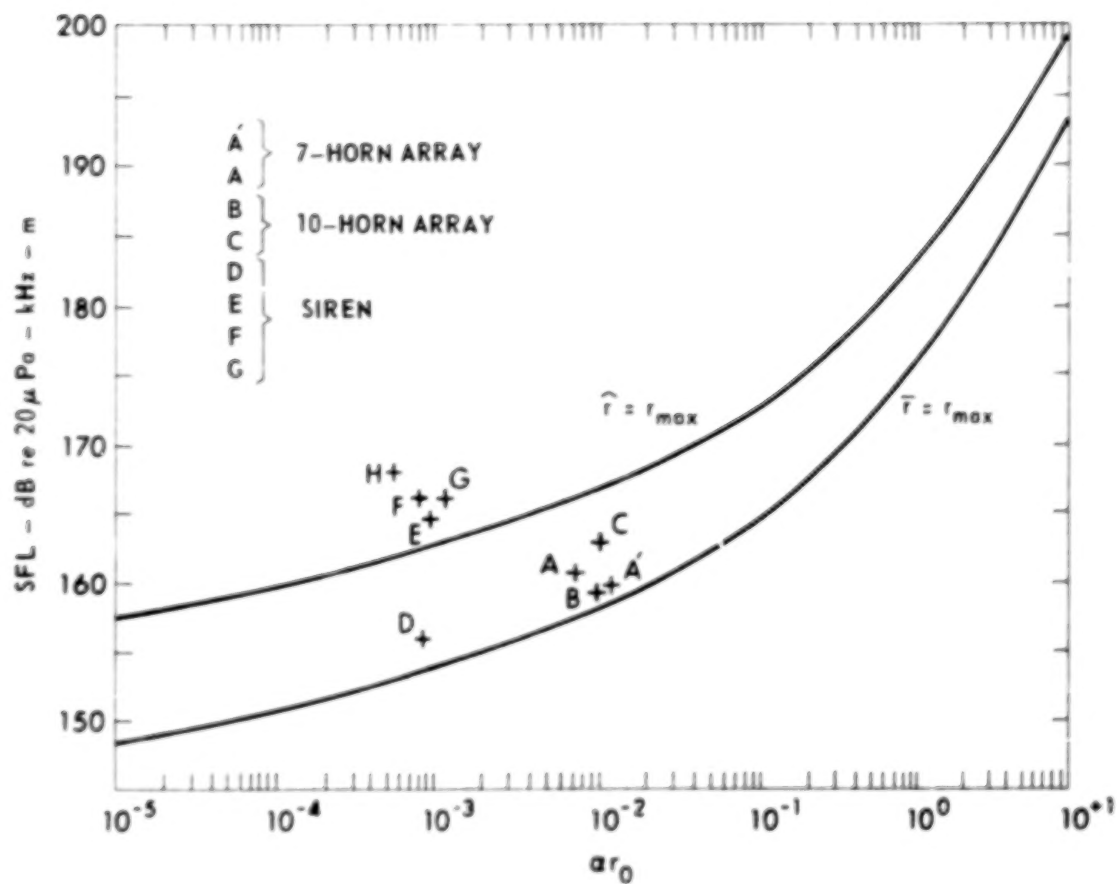
FIGURE 2-1
DESIGN CURVE TO ASSESS THE IMPORTANCE OF
NONLINEARITY ON SPHERICAL WAVE PROPAGATION IN AIR.
(TAKEN FROM Refs. 1,2)

nor much, if any, extra attenuation of the fundamental. Harmonic
distortion may develop, the amount depending on the proximity of the
the operating point to the lower curve. Conversely, if the operating point
lies above the upper curve, the source is classified as strong. Rapid
distortion, shock formation, the development of a full-fledged sawtooth
waveform, and significant extra attenuation of the fundamental is expected.
Finally, an operating point lying between the two curves denotes a
moderate source because it has only moderate ability to generate finite-
amplitude sound. The various lettered points plotted on the chart are
operating points of experiments carried out during Phase I. The intensity
of nonlinear effects observed in these experiments correlated very well
with the positions of the points relative to the two curves. The SFL
chart therefore proved to be a valid design tool.*
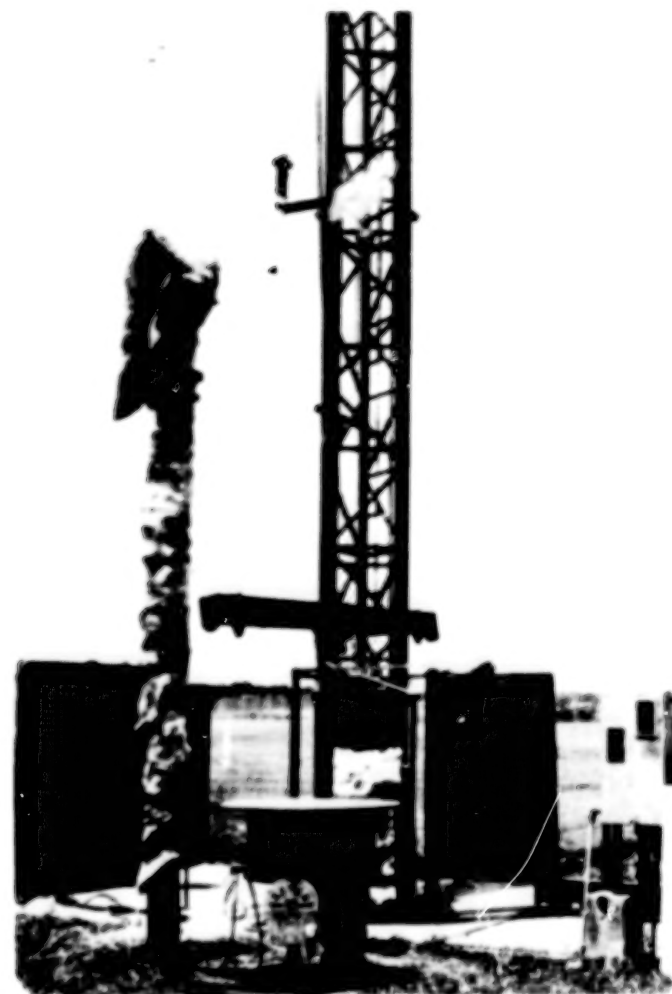
2. Apparatus and Measurement

The experimental facility is now described briefly. To avoid inter-
ference effects due to ground reflection, we used a vertical propagation
path that was parallel to a radio tower whose height is 85 m. The source was
on the ground. After passing through a relatively short nearfield, the waves
spread spherically over the remainder of the propagation path. The receiving
microphone was mounted at the end of a 2.6 m boom, which was carried by
the tower elevator. See Fig. 2-2a. A detailed block diagram of the experiment
is given in Ref. 1. Alternatively, because the transmit and receive systems
were similar to the ones used in Phase II, the reader may simply refer to
Fig. 4-1.

---

*To apply the SFL chart to fresh water at 20°C, use 1 µPa-kHz-m as the
reference for SFL and increase the numbers on the ordinate scale in Fig. 2-1
by 113.2 dB, e.g., 150 dB becomes 263.2 dB. To allow for salinity and
temperature changes, make use of information given in Table I of Ref. 21.

(a) TOWER AND ELEVATOR
WITH MICROPHONE BOOM

(b) BASE OF TOWER, INDEXING
TABLE, AND 7-HORN ARRAY
(WITH BAFFLE ATTACHED)

FIGURE 2-2
TOWER

Three different sources were employed. A 7-element array of exponential horns (Fig. 2-3a) was used for weak-wave and moderate-wave experiments; the horns were driven by JBL 375 horn drivers. The array is shown on its mount, a heavy indexing table, in Fig. 2-2b (the baffle visible in the picture was not used in any of the propagation experiments). Slightly more intense waves were radiated by a 10-horn array (Fig. 2-3b); see, for example, point C in Fig. 2-1. To produce truly strong waves, however, we had to construct a siren (Fig. 2-4). With it, experiments with operating points in the strong wave region (Fig. 2-1) were possible.

It was found early that random inhomogeneity of the medium, presumably due to velocity and temperature variations, caused fluctuations in the received signal. Not surprisingly, the fluctuations increased with propagation distance. At the same time, however, it was found that long term averaging (the averaging time of the analyzer was selectable) provided SPL data that agreed well with predictions based on homogeneous media theory. The required averaging time varied from 0.1 sec close to the ground to a maximum of 100 sec at the greatest distances. An important measurement that could not be averaged was waveform. Waveforms were recorded with the oscilloscope camera, but they are only samples at specific instants. A discussion of fluctuations in Phase II is given in Chapter 4 of this report, and some pure tone data showing the increase in fluctuation with receiver height are presented in Appendix C.

3. Theory

Three different methods were used to obtain theoretical curves to which the experimental data could be compared. First, for weak-wave experiments, a perturbation solution of Burgers' equation for spherical waves was obtained.[2] All terms through fourth order were found and also
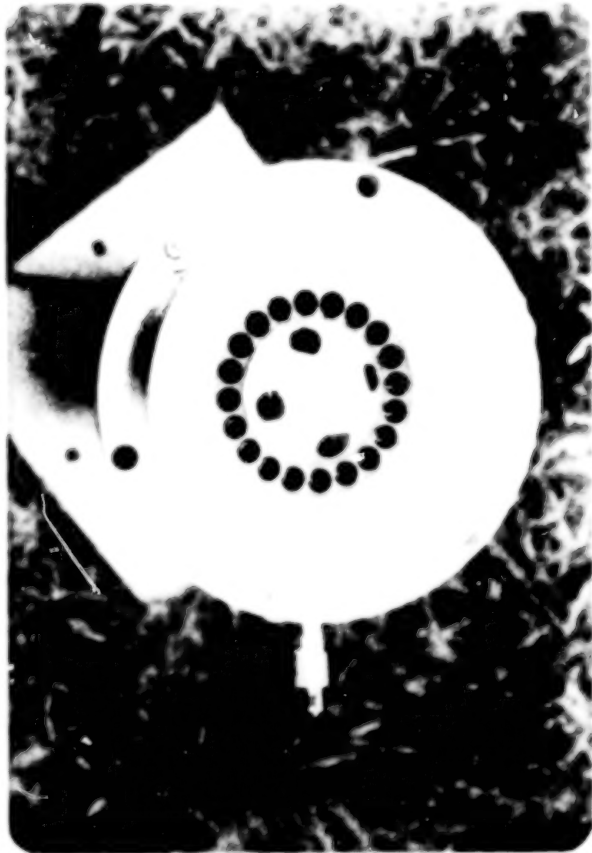
-HORN ARRAY

(b) 10-HORN ARRAY

FIGURE 2-3
HORN ARRAYS

(a) SIDE VIEW

(b) VIEW OF SIREN PORTS
AND CONICAL HORN

FIGURE 2-4
SIREN WITH HORN

Taken from Ref. 28

some of the fifth-order terms. Although Burgers' equation applies only to a medium whose attenuation coefficient α is proportional of f^2, the atmosphere has this property over limited frequency ranges. The perturbation solution is given in Appendix A. Second. an amplitude decay equation that had been postulated several years ago[*] for the fundamental component in a sawtooth wave was solved (again, see Appendix A).[2] Spherical spreading, atmospheric attenuation, and losses due to nonlinear effects (pumping of energy to the higher harmonics) are accounted for in this equation. Finally, Pestorius's computer algorithm,[6] generalized to apply to spherical waves in the atmosphere, was used to generate theoretical predictions for several of the experiments.[1] The algorithm is basically the same as the one discussed in Chapter 3. Whenever predictions were computed for a given experiment, all the necessary atmospheric attenuation coefficients were calculated by the method described in the new proposed standard.[24]

From the perturbation solution, an important conclusion may be drawn about how the harmonic distortion components decay with distance. The leading term in the expression for p_2, the amplitude of the second harmonic component, is (see Eq. A-14 or Refs. 5 and 27)

$$p_2 = p_{10} \; \frac{\beta k r_o}{2} \; \frac{r_o}{r} \; e^{-4\alpha(r - r_o)} \; I_{22} \; (\alpha r_o, \alpha r) \quad , \qquad (2\text{-}3)$$

where I_{22} is the integral

$$I_{22} = \int_{r_o}^{r} \frac{e^{2\alpha(r' - r_o)}}{r'} \; dr' \quad ,$$

which can be expressed as the difference of two Ei functions.[34] Note that I_{22} increases monotonically with distance. Although the second harmonic component has some resemblance to a small-signal wave of frequency $2f$

---

* D. T. Blackstock, unpublished research (1971).

(notice the factors denoting ordinary spherical spreading and exponential attenuation in Eq. 2-3), it really behaves differently. After first increasing with distance, p_2 reaches a maximum and then decreases. The decay region is particularly interesting. Because of the monotonically increasing property of I_{22}, the second harmonic never reaches a point at which its decay approaches that of a small signal. It always decays less rapidly than a small-signal wave of the same frequency. In particular, at great distances, the formula for p_2 is

$$p_2 = p_{10} \frac{\beta \epsilon k}{4\alpha} \left(\frac{r_o}{r} \right)^2 e^{-2\alpha(r - r_o)} \qquad , \qquad (2-4)$$

which deviates markedly from what would be expected on the basis of linear theory. It will be seen that p_2 is proportional to p_1^2, where $p_1 = p_{10}(r_o/r)e^{-\alpha(r - r_o)}$ is the local amplitude of the fundamental. Similarly it can be shown that the third harmonic amplitude p_3 never behaves as a small signal of frequency 3f; in fact, at great distances p_3 is proportional to p_1^3. The deviation from small-signal behavior therefore increases with harmonic number. The application of this result to aircraft noise was discussed in Chapter 1.

Although the theoretical models proved generally successful in explaining the experimental measurements, there was one recurring problem: how to account for nearfield distortion. Our theoretical models are for true spherical waves, which emanate from a source of radius r_o. Although sources of the type used in our experiments do produce spherical radiation, there is first a nearfield. Spherical spreading begins at approximately the Rayleigh distance ($R_o = S/\lambda$, where S is the radiating area of the source and λ is the wavelength). Because some distortion takes place in

the nearfield, the wave is not monochromatic, as assumed in our simple

theory, when spreading begins. A rigorous analytical treatment of finite-

amplitude distortion in the nearfield was out of the question. Our near-

fields were too complicated. At the same time, nearfield distortion was too

large to be ignored. We therefore accounted for it empirically. One empiri-

cal method that has been used successfully in the past[19] is to replace the real

source and its nearfield by an equivalent spherical source that matches

directly to an inward extension of the farfield. The radius r_o of the

equivalent source is taken to be a fraction of the Rayleigh distance.

The fraction is to be chosen so that the equivalent spherical wave distorts

as much in traveling from r_o to R_o as the real wave does in traveling

through the nearfield. In the past, giving the fraction a value in the

range 1/3 to 3/4 has worked well.[19] An arbitrary choice, such as

$r_o = R_o/2$, is useful for design purposes, for example, for specifying an

operating point on the SFL chart. For application to a particular experiment,

however, once the data have been taken, the values of p_1 and p_2 measured

at a single point in the farfield can be used to compute the value

of r_o for that experiment. We used this procedure to obtain values of r_o

for our theoretical predictions.

The equivalent spherical source model has several drawbacks, however.

The nearfield phase changes, which can be large, are ignored in the model.

The fact that r_o is frequency dependent makes the model difficult to apply

when the source signal itself is distorted or broadband.* Finally, in

practice we found that r_o varies with source amplitude as well as frequency.

_____

*In fact, the model proved to be of little use in Phase II, where the source

signal was noise.

Therefore, despite its conceptual simplicity, the model leaves much to be desired. It is useful for design calculations and for providing an initial match between theory and measurement for a specific experiment. It is not however, worthy of blind faith.

B. EXPERIMENTS

1. Weak Waves

Figure 2-5 shows the results of an experiment done with the 7-horn array at 8.25 kHz. All data points shown are in the farfield; the Rayleigh distance was 3.2 m. On the SFL chart (Fig. 2-1) the operating point for the experiment is A' (SFL = 160 dB, αr_o = 0.012, where for this purpose the value $R_o/2$ is used for r_o). Although A' falls slightly above the lower curve, for simplicity we call this a weak-wave experiment. For theoretical calculations the equivalent spherical source model was not used to compensate for nearfield distortion. Instead, r_o was taken to be the initial measurement distance (6.1 m). The distorted signal measured at this point was specified as the boundary condition for the perturbation solution of Burgers' equation.* The three curves pertaining to p_2 are explained as follows: The dotted curve represents the component of the second harmonic generated nonlinearly in the region $r > r_o$ (Eq. A-9a). The solid curve represents the small-signal decay of the second harmonic component initially present at $r = r_o$. When the two components are combined according to Eq. A-21 (in this case the phase angle ϕ was approximately $0°$), the result is the dashed curve, which accounts very well for the measured data. As for the fundamental, the solid curve represents the linear theory prediction. The dashed curve includes the reduction of the fundamental caused by its nonlinear interaction with the initial second

---

* Burgers' equation is suitable for predicting p_1 and p_2 because, for the conditions of the experiment, $\imath_2 = 4\imath_1$.
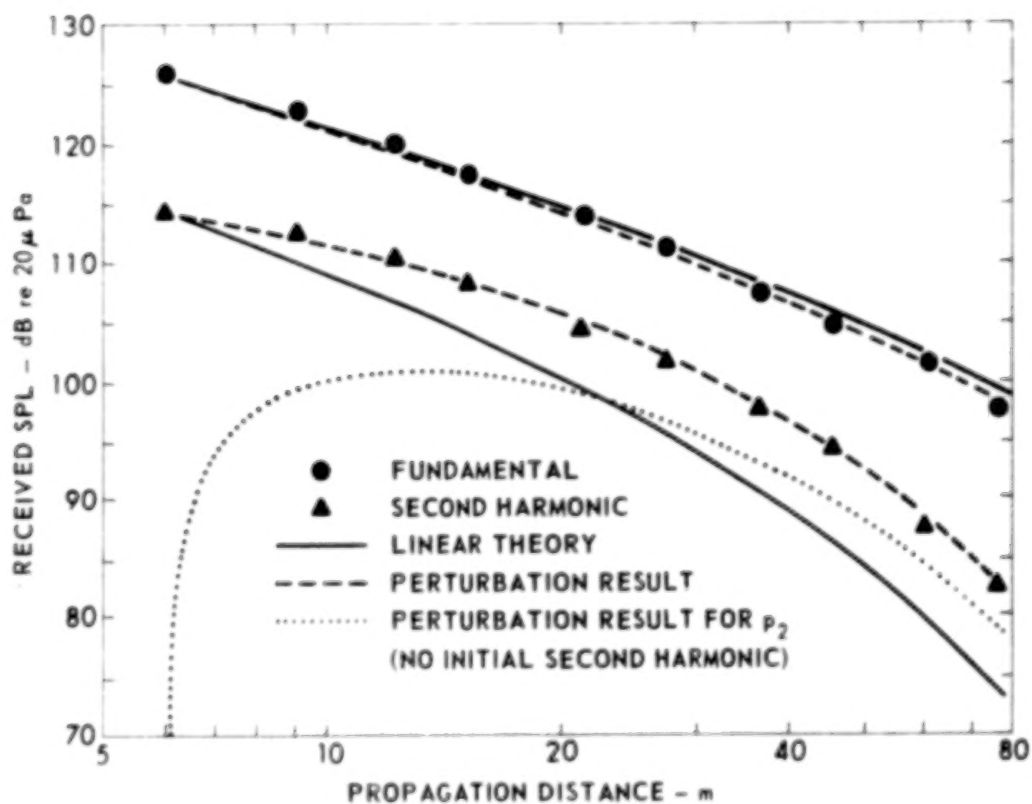
25

FIGURE 2-5

PROPAGATION DATA, WEAK-WAVE EXPERIMENT
SPL_{1m} = 141.5 dB, f = 8.25 kHz, TEMP = 27°C
RH = 72%, α = 0.0076 Np/m.
(POINT A IN Fig. 2-1)

harmonic (see Eq. A-20). The dashed curve seems to fit the data slightly better than the solid curve. In summary, second-order perturbation theory provides an excellent explanation of both propagation curves. Moreover, the mildness of the nonlinear effects observed in this experiment correlates well with the relative position of point A' on the SFL chart.

Notice how the second harmonic signal generated nonlinearly in the region $r > r_o$ (dotted curve) eventually overtakes and masks the second harmonic that was initially present at r_o. Although the latter was itself non-linearly generated in the region $r < r_o$, it is small enough in amplitude to decay as a small signal in the region $r > r_o$ (note that the decay factor is $e^{-\alpha(r-r_o)}$, not $e^{-\alpha r}$). Considering r_o as the effective source radius, therefore, we see that the behavior of the data in this experiment supports an assertion made in Chapter 1: When a nonlinearly generated second-harmonic sound is masked by a small signal of the same frequency, the propagation will eventually be dominated by the nonlinearly generated component because of its less rapid decay. Unfortunately, our range of measurement distance did not extend far enough to test the asymptotic formula Eq. 2-4.

2. Moderate Waves

The results shown in Figs. 2-6 and 2-7 are for an experiment done with the 10-horn array. The Rayleigh distance was 3.6 m, the frequency was 6.6 kHz, and the source level was 146.5 dB. The experiment is represented on the SFL chart (Fig. 2-1) by point C (SFL = 163 dB, αr_o = 0.0096), which is right in the middle of the moderate-wave region. The theoretical predictions were obtained by using the computer algorithm. The measured waveform at 6.1 m (Fig. 2-7a) was used as the initial signal for the computation.
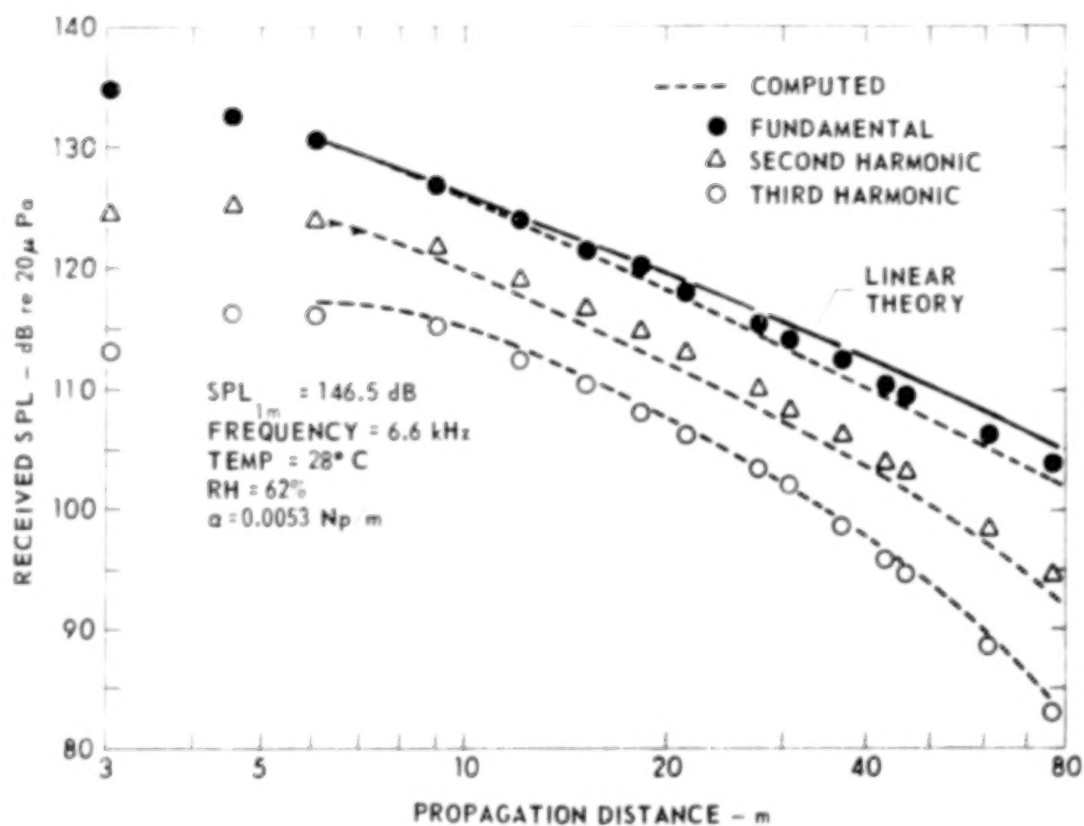
FIGURE 2–6
PROPAGATION DATA, MODERATE–WAVE EXPERIMENT
(POINT C ON Fig. 2–1)

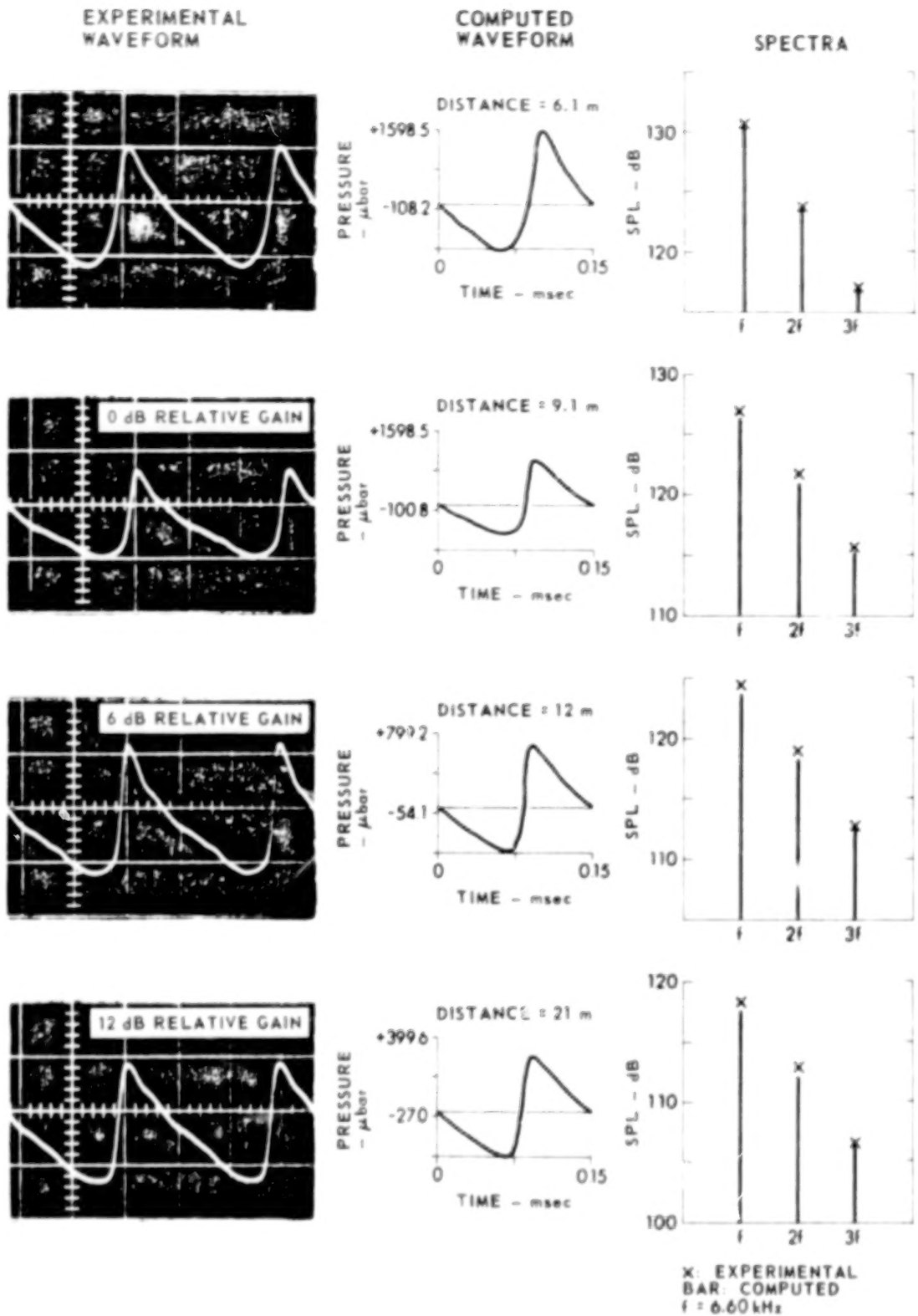EXPERIMENTAL WAVEFORM   COMPUTED WAVEFORM   SPECTRA

FIGURE 2-7a
WAVEFORMS AND SPECTRA, MODERATE-WAVE EXPERIMENT

EXPERIMENTAL
WAVEFORM

COMPUTED
WAVEFORM

SPECTRA

FIGURE 2-7b
WAVEFORMS AND SPECTRA, MODERATE-WAVE EXPERIMENT

X: EXPERIMENTAL
BAR: COMPUTED
f = 1.60 kHz

During the course of the measurements the atmosphere was very calm. There was no wind at all on the ground and the anemometer read only 0-4 km/hr at the top of the tower.

Nonlinear distortion in this experiment is seen to be appreciably greater than in the previous one. The fundamental clearly suffers extra attenuation, albeit not large. Shock formation is indicated by the crowding together of the propagation curves in Fig. 2-6 and is confirmed by the waveforms in Fig. 2-7. In fact, the waveforms at 12 m and 21 m have a nearly sawtooth shape. When this experiment is contrasted with the previous one, it is interesting to note that the large increase in nonlinear effects is due to an increase of only 3 dB in SPL (compare the positions of points A' and C in Fig. 2-1). The relatively sharp onset of finite-amplitude behavior was noticed repeatedly throughout the project. Nonlinearity in spherical waves seems to be almost a threshold phenomenon. An increase of 3 dB in source level can have either a small effect or a large effect, depending on the starting point.

Except at the greatest distances, the waveforms in Fig. 2-7 are asymmetric. The peaks are sharp and the troughs are round. Deviation of this sort from the ideal sawtooth shape is probably caused by diffraction effects, which are not included in the simple spherical wave models dis-cussed thus far. There are at least two sources of diffraction in our experiments. First there is piston type diffraction. If the mouth of a horn is likened to a radiating piston, the following result from linear piston radiation theory may be used: on axis the farfield signal is proportional to the time derivative of the piston velocity.* In this

_____

* In Chapter 3 we discuss the frequency domain version of this result, which is that the farfield spectrum has a 6 dB/octave boost relative to the mouth spectrum.

31

experiment the mouth signal is not a sinusoid. In traveling through the horn, the wave suffers some finite-amplitude distortion. It arrives at the mouth with a waveform similar to the last measured waveform in Fig. 2-7b. Given this shape, differentiation will produce a waveform that is asymmetric like the one at 6.1 m in Fig. 2-7a. This effect was observed and reported early in Phase I.[20,2] Another diffraction effect, which also produces the same kind of waveform asymmetry, is associated with narrow beams. This effect has been analyzed by the Russian investigators.[23] Although our beam does not have quite the same characteristics as the beam they have analyzed, our beam was relatively narrow (3 dB beamwidth of about 6° in this experiment). Some of the asymmetry evident in Fig. 2-7 may therefore be due to narrow beam diffraction.

Two further aspects of the asymmetry may be noted. First, although the asymmetry eventually disappears as propagation distance increases, the disappearance is faster in the computed waveforms than in the measured waveforms. The computed waveforms become symmetric more rapidly because (1) no diffraction effect is included in the algorithm to perpetuate the initial asymmetry, and (2) ordinary nonlinear steepening tends to wash out the asymmetry. The fact that in the measured waveforms the asymmetry seems to first increase (or at least hold its own) with distance supports the speculation that narrow beam diffraction may have been important while the beam diameter was still small. Second, as noted in the footnote on the preceding page, the differentiation operation, which accounts for the asymmetry (no matter whether the asymmetry is due to source diffraction or beam diffraction), gives the higher harmonics a boost. This may help explain why the second harmonic data lie somewhat above the computed propagation curve in Fig. 2-6. In fact, at 12 m the separation between

data points for the fundamental and second harmonic signals is slightly less than 6 dB. A separation of less than 6 dB is not expected for an ordinary sawtooth wave, but as Fig. 2-7 shows, the waveform at 12 m is a peaked sawtooth.

Finally, the discrepancy in Fig. 2-7 between predicted and measured waveforms at 76 m, and to a lesser extent at 61 m, is probably due to inhomogeneity of the medium. Although each data point in Fig. 2-6 represents a time average measurement, the waveforms in Fig. 2-7 are single samples. As the fluctuations increase with propagation distance, so does the possibility of recording a sample that varies considerably from the average.

3.   Strong Waves.

Propagation data for one of the siren experiments are shown in Fig. 2-8. The short conical horn (diameter 0.152 m) fitted to the end of the siren (see Fig. 2-4) was designed to convert the siren from a ring source into a piston-like source. The operating conditions for the experiment described here, f=6.33 kHz, SPL_{1m} = 150 dB, and α = 0.0070 Np/m -- define point G on the SFL chart (Fig. 2-1). The transmitted sound had a wide beam, approximately 40° between 3 dB down points, and a short nearfield (the computed value of R_o was 0.33 m).

The sound generated in this experiment was very intense. The magnitude of the intensity may be judged in several ways. First, the crowding together of the propagation data for the fundamental, second harmonic, and third harmonic, even at distances less than 1 m, suggests that the wave formed a sawtooth very close to the source. Indeed this was the case, as oscillograms of the waveform show.[1] Second, the propagation data for the fundamental deviate markedly from the linear theory curve. At 30 m the deviation, or extra attenuation, is 10 to 11 dB. Third, from

about 3 m on, the data are only 1 to 2 dB less than their predicted saturation values. At saturation the received level is at an absolute maximum value that cannot be exceeded no matter how high the source level is raised.[19,24] Therefore, raising the source level of the siren from 150 dB to, say, 156 dB (a quadrupling of the source power), would not be expected to change the propagation data much from that shown in Fig. 2-8.

Although not shown in Fig. 2-8, theoretical predictions obtained by means of the computer algorithm provided a reasonably good fit to the propagation data. Predictions based on a simple amplitude decay rate model, explained in Section II or Appendix A (where a second siren experiment is also described), were found to agree very well with the data for the fundamental. See Eq. A-28, from which it is a simple matter to obtain predictions of both extra attenuation and saturation amplitude.

The sawtooth waveforms in this experiment were also observed to be asymmetric.[1] The asymmetry was strong up close to the source but tended to die out monotonically and more rapidly than in the 10-horn array experiment (Fig. 2-7). This behavior is consistent with the difference between the sources in the two experiments. Because the siren produced a very broad beam, asymmetry was limited to that caused by source diffraction. Because of the greater intensity in the siren experiment, the asymmetry was more quickly overcome by nonlinear steepening.

C. Summary

In summary, the tone experiments covered a wide range of wave strengths, from very weak to very strong. The classical nonlinear propagation phenomena that are well known from indoor experiments -- harmonic distortion, shock formation, and extra attenuation (to the brink of saturation) -- were observed
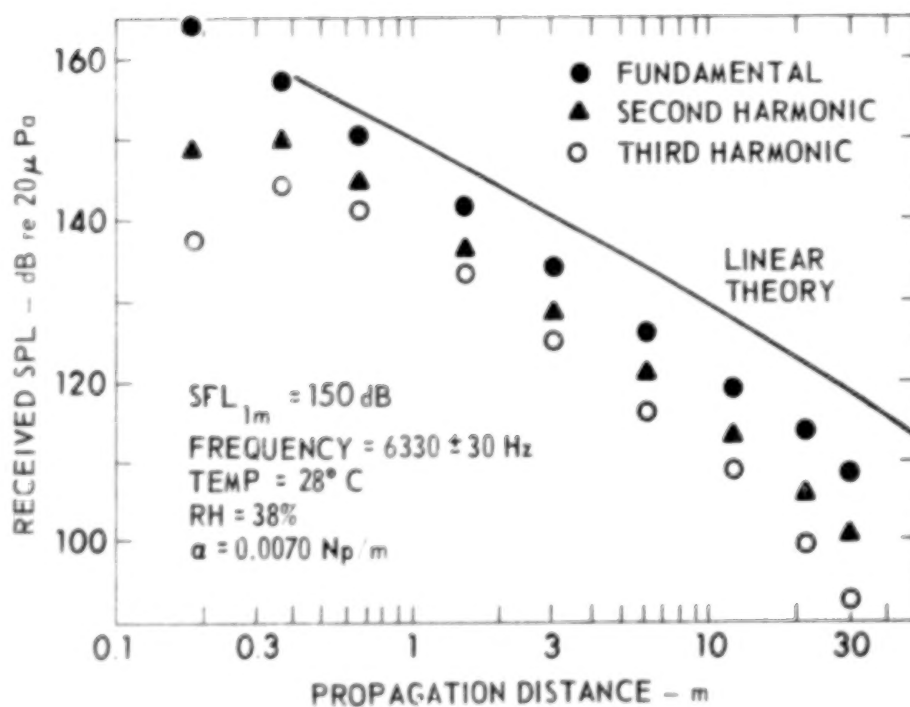
FIGURE 2-8
PROPAGATION DATA, STRONG-WAVE EXPERIMENT
(POINT G ON Fig. 2-1)

in the outdoor environment. Moreover, provided sufficient averaging time was allowed for the measurements, theory and measurements were found to be in good agreement even though the theory was for a homogeneous medium. Asymmetric waveforms qualitatively attributed to diffraction effects were observed.

CHAPTER 3

THEORY

In this chapter the theory of freefield propagation of finite-amplitude noise in the atmosphere is considered. Although the atmosphere is actually inhomogeneous, our experience in Phase I showed that, for our experimental conditions, the assumption that the medium is quiet and homogeneous works well if sufficient signal averaging is employed. In our discussion we therefore consider freefield propagation in a homogeneous, quiet medium.

A. LINEAR THEORY

Let $F(r_o, \omega)$ be the noise power spectrum at range $r_o \geq R_o$, where the Rayleigh distance R_o marks the beginning of the transmitter farfield. If the subsequent propagation is dominated by spherical spreading and atmospheric absorption, the power spectrum at range $r \geq r_o$ is given by

$$F(r, \omega) = \frac{r_o^2 e^{[-2a(\omega)(r - r_o)]}}{r^2} F(r_o, \omega) , \qquad (3-1)$$

where $a(\omega)$ is the atmospheric absorption coefficient at angular frequency ω. In this report absorption coefficients are calculated according to the new proposed standard.[22] We shall frequently use the term "linear theory" to characterize computations based on Eq. 3-1.

Nothing has been said so far about the source of the farfield spectrum $F(R_o, \omega)$. We take the source to be a circular horn or aperture. The geometry is shown in Fig. 3-1. The wavefront is assumed
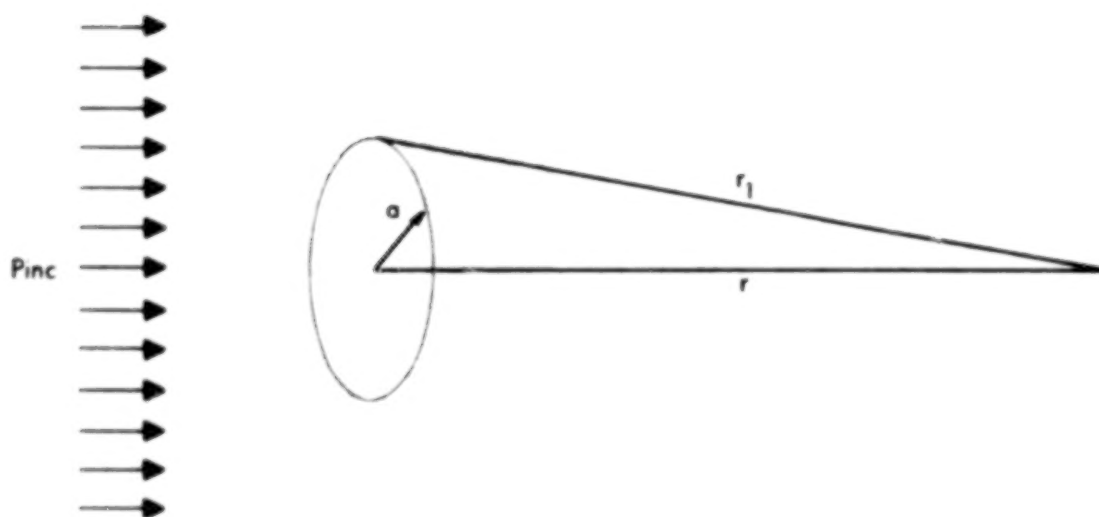
FIGURE 3-1
GEOMETRY OF THE DIFFRACTION OF SOUND
BY A CIRCULAR APERTURE

to be plane in the aperture; the power spectrum there is given by $F(0,\omega)$. The spectrum at any point r on the axis in front of the aperture is

$$F(r,\omega) = \left| \; e^{-(jk+\alpha)r} - e^{-(jk+\alpha)r_1} \; \right|^2 F(0,\omega) \quad , \tag{3-2}$$

where $j=(-1)^{1/2}$ and $r_1=\sqrt{r^2+a^2}$ is the distance from the aperture edge to the observation point (see Fig. 3-1). In the farfield ($r \gg a$), $r_1 \doteq r + a^2/2r$ and Eq. 3-2 reduces to

$$F(r,\omega) = \left(\frac{R_o(\omega)}{r}\right)^2 \left(1 + \frac{\alpha^2}{k^2}\right) e^{-2\alpha r} \; F(0,\omega) \quad ,$$

$$\doteq \left(\frac{R_o(\omega)}{r}\right)^2 e^{-2\alpha r} F(0,\omega) \tag{3-3}$$

since $\alpha/k \ll 1$ for $f < 1$ MHz. In terms of the aperture area $S=\pi a^2$, the Rayleigh or farfield distance is

$$R_o(\omega) = \frac{S\omega}{2\pi c_o} \quad . \tag{3-4}$$

Because the farfield distance increases with frequency, the farfield spectrum has a high frequency boost compared to the source spectrum. Provided the observation point is not deep in the farfield, $F(r,\omega) \propto \omega F(0,\omega)$, i.e., the boost is 6 dB/octave. The farfield distance for the entire spectrum is $R_o(\omega_m)$ where ω_m corresponds to the highest frequency of interest in the source spectrum $F(0,\omega)$. For other sources of interest, e.g., a rectangular aperture, Eqs. 3-3 and 3-4 may be used by taking S to be the radiating area of the source. If the source is an array of apertures, S is the total area of all apertures. We shall refer to computations based on Eqs. 3-2 and 3-3 as "linear diffraction theory."

B. NONLINEAR THEORY

In the previous section we presented results valid in both the trans-
mitter nearfield and farfield. As noted in Chapter 2, there is no well-
developed theory for the nearfield of finite-amplitude waves. In analyzing
propagation of finite-amplitude waves, therefore, we have to restrict our
attention to the farfield problem.

Our approach to the problem of finite-amplitude spherical noise
waves is similar to that of Pestorius, who developed a computer algorithm
to treat plane waves of noise.[6] The analysis we present here is valid
prior to shock formation, although it can easily be extended beyond by using
the relations of weak-shock theory.[6] The plane wave algorithm is based on
the solution of the nonlinear wave equation for plane progressive waves in
a lossless gas. The equation is $c_o{}^2 u_x + c_o u_t - \beta u u_t = 0$, where x is
propagation distance and t is time. or, if the retarded time $t' = t - x/c_o$
is introduced,

$$c_o{}^2 u_x - \beta u u_{t'} = 0 \quad . \tag{3-5}$$

This equation is the mathematical embodiment of the distortion process,
wherein the compression phases of a wave tend to steepen; see
Chapter 1. For a boundary condition of the form

$$u \Big|_{x=0} = g(t) = g(t') \quad , \tag{3-6}$$

the exact solution of Eq. 3-5, called the Earnshaw solution, is

$$u = g(\tau) \quad , \tag{3-7a}$$

where

$$t' = \tau - \frac{\beta x u(\tau)}{c_o{}^2} \quad . \tag{3-7b}$$

The parameter τ is the time base for the source signal, that is, $\tau=t'=t$ when $x=0$. Although it is difficult to obtain analytical results from the Earnshaw solution, the solution may easily be implemented as a computer algorithm. The waveform at any desired distance x is computed simply by distorting the time base according to Eq. 3-7b. However, ordinary absorption, which is frequently important, is not included in the Earnshaw solution. In order to account for ordinary absorption, we assume that even when the medium is lossy, Eqs. 3-7 may be used to propagate the wave a suitably small distance Δx. After a transformation to the frequency domain, absorption corrections appropriate for the distance Δx are applied. There follows a transformation back to the time domain, where another short propagation step is made. The process is repeated until the desired propagation distance is reached.

For spherical waves, the computation is much the same. The wave equation for spherical waves reduces to Eq. 3-5 if one makes the changes of variable

$$w = \frac{r}{r_0} u \quad , \tag{3-8a}$$

and

$$x = r_0 \ln(r/r_0) \quad . \tag{3-8b}$$

In terms of distortion, spherical wave propagation from r to $r + \Delta r$ is equivalent to plane wave propagation from x to $x + \Delta x$ if Δx is given by

$$\Delta x = r_0 \ln[1 + \frac{\Delta r}{r}] \quad . \tag{3-9}$$

A block diagram of the computational procedure for spherical waves, which is based on Eqs. 3-7 and 3-8, is shown in Fig. 3-2. It is assumed here that we wish to propagate the wave from $r = r_0$ to $r = r_1$, where $r_1 \geq r_0$. The input
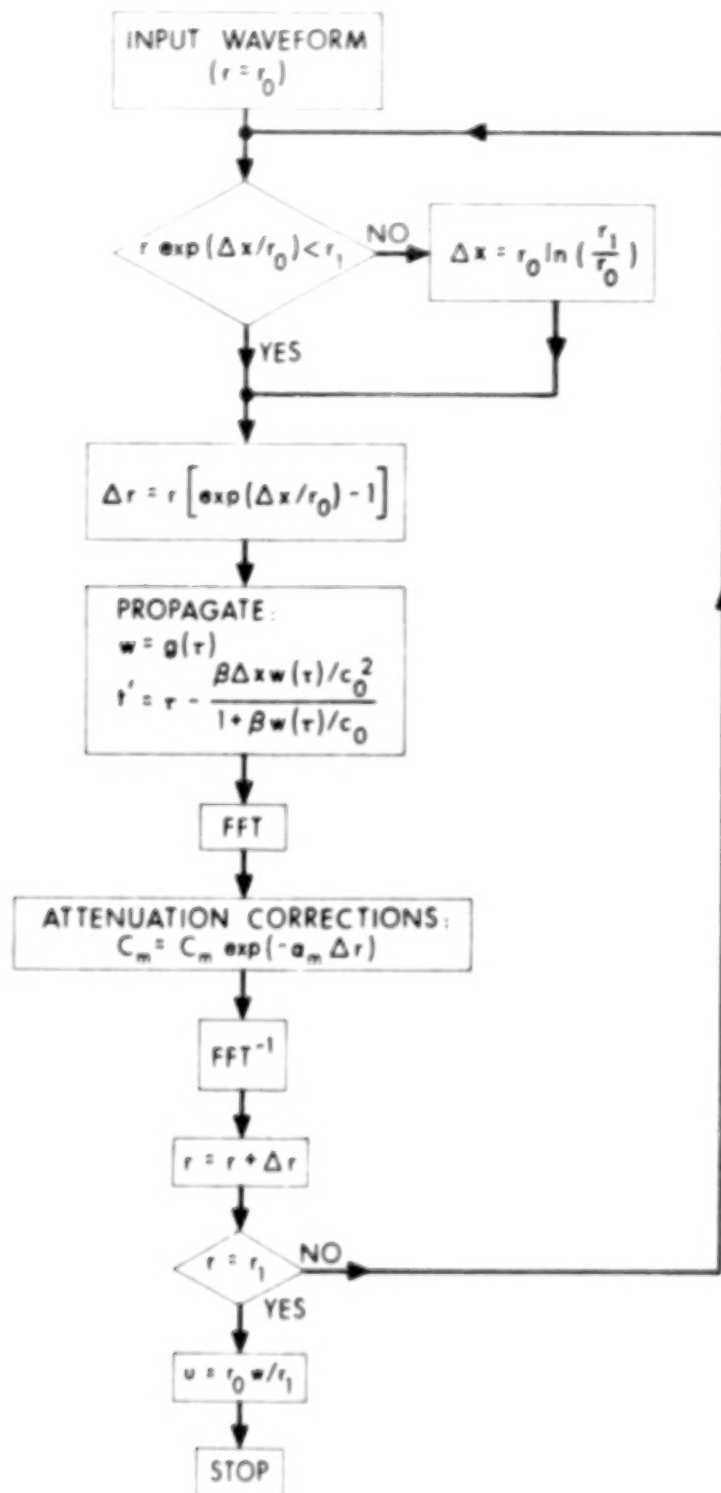
INPUT WAVEFORM
$(r = r_0)$

$r \exp(\Delta x/r_0) < r_1$ — NO → $\Delta x = r_0 \ln\left(\dfrac{r_1}{r_0}\right)$

YES

$\Delta r = r\left[\exp(\Delta x/r_0) - 1\right]$

PROPAGATE:
$w = g(\tau)$
$t' = \tau - \dfrac{\beta \Delta x w(\tau)/c_0^2}{1 + \beta w(\tau)/c_0}$

FFT

ATTENUATION CORRECTIONS:
$C_m = C_m \exp(-a_m \Delta r)$

FFT^{-1}

$r = r + \Delta r$

$r = r_1$ — NO

YES

$u = r_0 w / r_1$

STOP

FIGURE 3-2
BLOCK DIAGRAM OF THE COMPUTATIONAL PROCEDURE
FOR SPHERICAL WAVES

(NOTE THAT IF SHOCK FORMATION IS POSSIBLE, THE
BLOCK LABELED PROPAGATE COULD BE REPLACED
WITH THE WEAK SHOCK PROPAGATION MODEL OF Ref. 6)

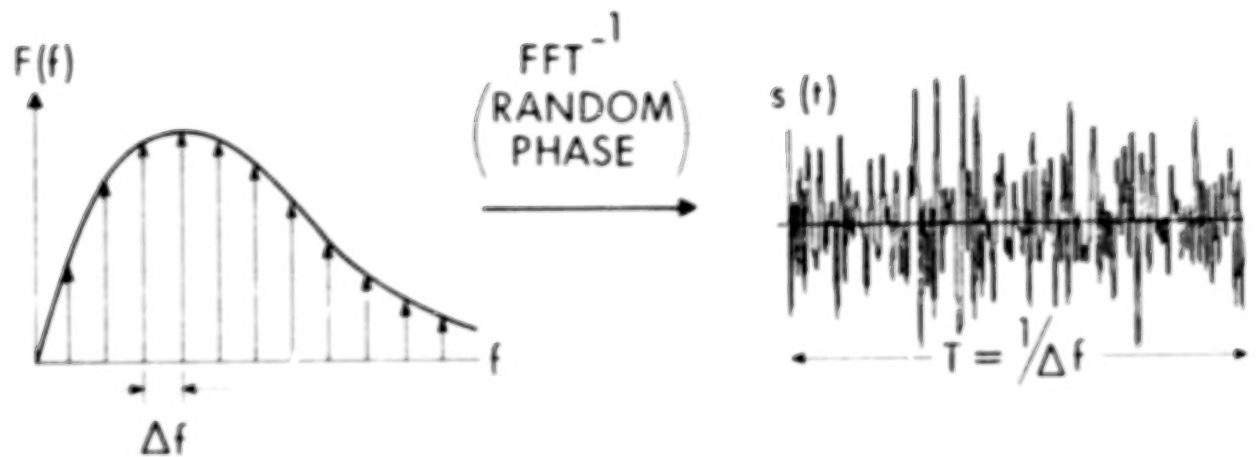waveform w is specified at $r = r_o$, as is the incremental step size Δx.[*]
A check is performed to determine whether propagation over Δx will exceed the
desired range r_1. If so, Δx is set to a value such that $r + \Delta r = r_1$. If not,
the current value of Δx is used. The equivalent spherical wave step size Δr
is computed, and the wave is propagated the equivalent plane wave distance
Δx according to Eqs. 3-7. We next transform to the frequency domain in order
to make absorption corrections. After a transformation back to the time
domain, the current value of r is incremented. When the desired propagation
distance is reached ($r = r_1$), the correction for spherical spreading is
made (see Eq. 3-8a) and the computation is complete.

In order to use the computational procedure described in the previous
paragraphs, we must have a representation of the source waveform $u(r_o, t)$.
One approach would be to record a sample waveform of the noise at $r = r_o$
and use this as the source waveform. There are practical problems a' ciated
with this approach, however. First, the sample length must be sufficiently
long to reflect both the statistical and spectral properties of the noise.
In an outdoor environment, signal fluctuations caused by the randomness
of the medium may make the required sample length prohibitively long.
Second, recording equipment is required. Finally, even in field studies
in which recording equipment is used, the results are almost always
reported in terms of spectra, not waveforms. Developing an input
waveform from a spectral measurement therefore seemed to be an attractive
alternative to recording the waveform directly.

A method for constructing a suitable source waveform $s(t) = u(r_o, t)$ given

---

[*]The step size Δx is typically chosen as some fraction (say 0.1) of the
shock formation distance appropriate for a lossless medium. See Ref. 6
for further details.

just the power spectrum $F(r_o, \omega)$ is given in Ref. 25. We start with a

line spectrum of closely spaced components at the harmonic frequencies $n\Delta f$.

The envelope is a replica of the given average power spectrum $F(r_o, \omega)$,

scaled so that the mean square values of the two signals are equal (see

Fig. 3-3). If it is assumed that the given noise is Gaussian, the phase of

each component in the given noise is a random variable ϕ whose probability

density is uniform over the range $-\pi \leq \phi \leq \pi$.[25] In order that $u(r_o, t)$ have

the same property, we assign a random phase with a uniform probability

density to each of the harmonic components. Now having a complete frequency

domain description of the desired noise, we use an FFT^{-1} operation to

obtain the time waveform $u(r_o, t)$. The difficulty with this method is, of

course, that there are an infinite number of signals $u(r_o, t)$ with the same

power spectrum, i.e., there exist an infinite number of ways to assign

the random phase ϕ. Clearly the success of our method for representing

$u(r_o, t)$ depends upon the sensitivity of the computations to the particular

function $u(r_o, t)$ chosen. In a study of the interaction of an intense

tone with low level noise, Webster and Blackstock[25] found that the method

described here worked quite well. For the case of intense noise, however,

the validity of the model rests on comparison with the experimental data.

$$\int_0^\infty F(f)\,df = \frac{1}{T}\int_0^T s^2(t)\,dt$$

FIGURE 3-3

CONSTRUCTION OF THE SOURCE WAVEFORM GIVEN THE
POWER SPECTRUM F(f)

CHAPTER 4

EXPERIMENTAL APPARATUS AND PROCEDURE

In this chapter we describe the equipment and procedures used to make the experimental measurements reported in Chapter 5 and Appendices C and D. The experimental arrangement is much the same as that used in Phase I of the project.[1] We shall therefore give only a general description of the apparatus and procedures and point out the changes instituted for Phase II. For a more detailed account, the reader should consult Ref. 1.

A. EXPERIMENTAL APPARATUS

A general schematic of the experimental apparatus is given in Fig. 4-1. The electroacoustic source was either a 20-element horn array manufactured by Applied Electro-Mechanics (AEM) or a horn array driven by JBL 375 horn drivers. The AEM array (shown in Fig. 4-1) is described in detail in Appendix D. The JBL arrays were like the 7- and 10-element sources used in Phase I (Fig. 2-3), but single-element and 3-element arrays were also used. The indexing table on which the source was mounted (see Figs. 2-2b and 2-3) could be rotated and tilted for alignment and beam pattern measurements. The propagation distance was varied by moving the elevator car, on which the microphone boom was mounted, up and down the tower. In addition to the traveling microphone (1/4 in.) shown in Fig. 4-1, a monitor microphone (1/4 in. or 1/8 in.) was used for measurments near or inside the horn array. For all measurements taken with the traveling microphone, however, the monitor microphone was removed so that it did not affect the wave field.

A list of the more important equipment used is given below. For a more detailed list, see Ref. 1.

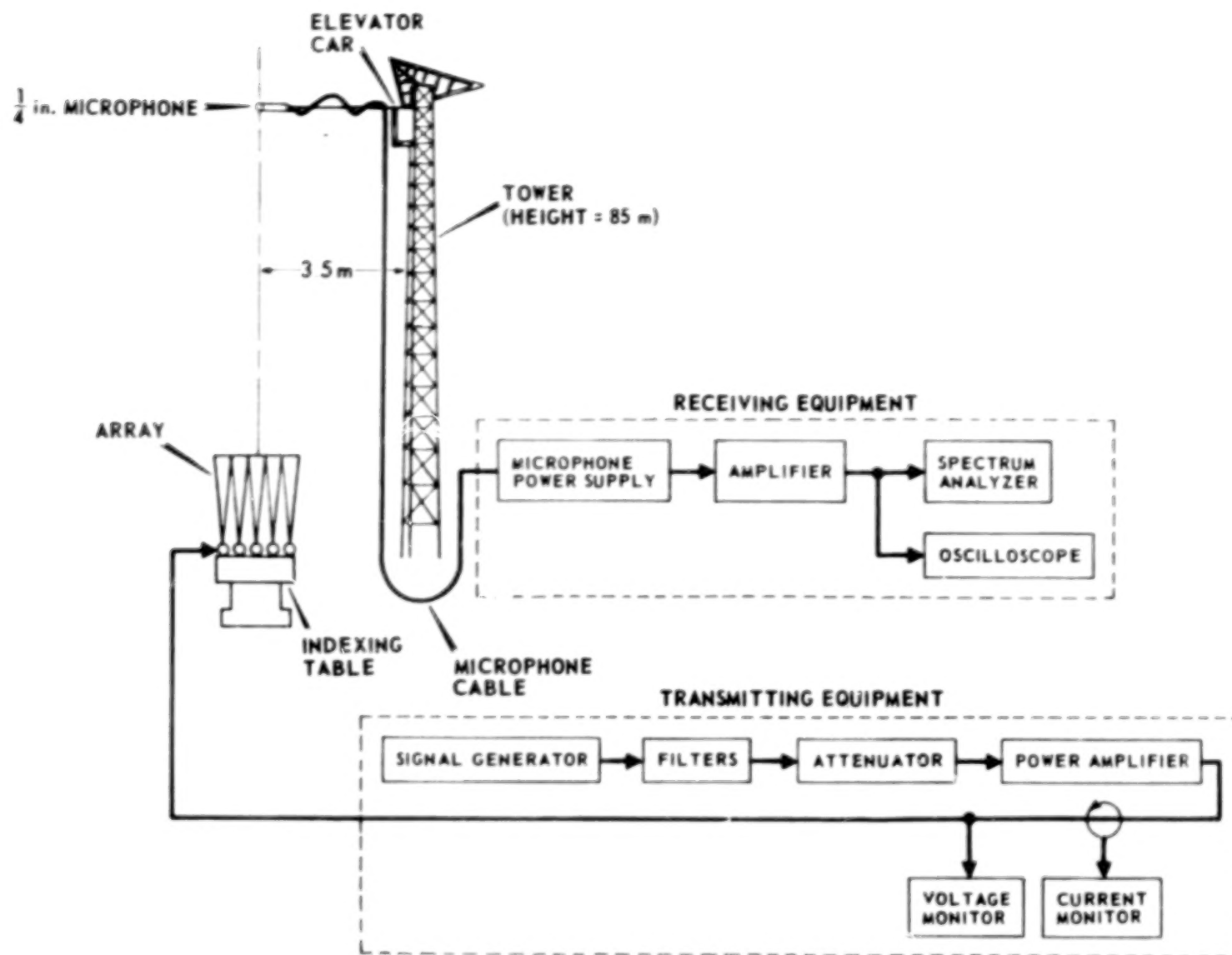(1) Microphone. B & K type 4136, 1/4 in. The pressure response is

46

FIGURE 4-1
BLOCK DIAGRAM OF THE EXPERIMENTAL ARRANGEMENT

nominally flat from 50 Hz to 50 kHz (1 dB down points) for grazing (90°) incidence. If the microphone is used under freefield conditions, the manufacturer's rated corrections to be added to the pressure response are -0.2 dB for the frequency range 9-14 kHz and +0.5 dB for the range 19-35 kHz.[26] All other components in the receiving system have a pass band at least as wide as 20 Hz to 100 kHz. The microphone is therefore the limiting element in the receiving system.

(2) Microphone. B & K Type 4138, 1/8 in. The 4138 microphone response was rated as flat to within ±1 dB from 20 Hz to 100 kHz. No free-field corrections were required to 70 kHz.[26] This microphone was used as a monitor only.

(3) Microphone Preamplifier. B & K Type 2619.

(4) Microphone Preamplifier and Power Supply. B & K Type 2801.

(5) Microphone Cables. B & K Type AO 0029 (30 m) and AO 0028 (10 m).

(6) Pistonphone (microphone calibrator). B & K Type 4220.

(7) Spectrum Analyzers. B & K Type 2010, H-P Model 3580A and G-R Type 1900-A.

(8) Power Amplifier. CML McCarr 5 kW.

(9) Current Transformer. Pearson Electronics Model 110.

(10) Signal Generators. B & K Type 1022 Oscillator or Elgenco Gaussian Noise Generator.

(11) Filters. B & K Type 2112 Audio Spectrometer and K-H Model 335R or 310-AB Band Pass Filters.

B. EXPERIMENTAL PROCEDURES

In this section we describe the procedures used in equipment checkout and calibration and also in the actual data acquisition. The procedures were the same for both noise and tone signals.

1.   Equipment Checkout and Calibration

Prior to and following each of the experiments, the following tasks were performed. First, the particular spectrum analyzer used was calibrated in both frequency and amplitude. Second, the pistonphone was used to make an absolute calibration of the receive system. The calibration was done first with the microphone connected directly to the microphone power supply and then with the 100 m cable (composed of three 30 m cables and one 10 m cable) inserted between the two (see Fig. 4-1). Comparison of the two calibration values indicated whether the cable and its connections were sound. If the two calibration values differed by more than 0.2 dB (the accuracy of the pistonphone output), cable repair was in order. Moreover, comparison of day to day calibration values was made to detect possible equipment malfunctions. Again, if deviation of more than 0.2 dB was observed, each component in the receive system was checked to determine the cause.

2.   Data Acquisition

The procedure was as follows. First, the elevator was moved to the desired position. The source was then activated and the received spectrum recorded. For the noise measurements, both the H-P 3580A and B & K 2010 analyzers were used. The H-P analyzer was used to record the continuous spectrum, while the B & K analyzer was used to measure the overall sound pressure level (OASPL). As a crosscheck on the measurements, the B & K analyzer was also used to record 100 Hz band levels at specific frequencies (usually 5, 10, and 20 kHz). These measurements were then compared with those recorded by the H-P analyzer. If the two measurements differed by more than 1 dB, the measurements were rejected and the cause of the discrepancy

was found. The rms input voltage and current to the array were also monitored during the measurement period. After all data were recorded at each of the desired ranges, the elevator car was moved back to the first measurement position. A new spectrum was recorded and checked against the spectrum previously recorded there. If the two spectra differed by more than 1 dB, the data were rejected and the cause of the difference was identified. The system of checks described here proved invaluable in assuring the internal consistency of the data.

Some mention should also be made of the averaging time used for the spectral measurements. In addition to the averaging required because of the statistical nature of the signal (noise), inhomogeneous medium effects (gusting winds and temperature variations) caused severe fluctuation in short-term average levels (see Appendix C). The averaging time of the H-P analyzer could be increased by increasing the RC time constant of the postvideo detector filter (the constant was adjustable via a front panel knob). The "maximum smoothing" setting (maximum averaging time) was found to be quite adequate when the 100 Hz bandwidth was used. The averaging time for the B & K analyzer was adjustable from 0.1 sec to 100 sec. For OASPL measurements averaging times of 1 sec to 3 sec were used; for 100 Hz band measurements the 100 sec position was chosen.

C. SUMMARY OF EXPERIMENTAL CONDITIONS

A catalog of the conditions for the experiments conducted in the Phase II research is given in Table 4-1. For the noise measurements the spectrum band limits correspond roughly to the most intense portion of the spectrum. The source level ($OASPL_{1m}$) is the farfield OASPL extrapolated (by spherical spreading) to 1 m. For the tone measurements $OASPL_{1m}$ is the extrapolated farfield SPL of the fundamental frequency component.

The characteristic ground level wind speeds observed roughly divide the experiments into two groups. During experiments JBL 3, 4, and 7 and AEM 1, 2, 5, 6, 8, and 9 wind speeds generally ranged from 13 to 24 km/h. For the remainder of the experiments wind speeds were between 7 and 10 km/h.

Finally, the experiments were performed at night during the period June-September 1977.

TABLE 4-1

CATALOG OF EXPERIMENTS

Experiment		Figure Number	$OASPL_{1m}$ * dB	Input Spectrum Band Limits, kHz	R_o m(kHz)	Temp. (°C)	RH (%)
JBL	1	5-6	121	1 - 7	0.53 (10)	23	75
	2	5-7	127	3 - 5.5	1.06 (20)	26	73
	3	5-8	132	3.5 - 6.6	3.18 (20)	24	90
	4	5-9	144	3.5 - 7	7.42 (20)	24	86
	5	5-5	140	2.8 - 5.6	7.42 (20)	26	73
	6**						
	7	5-10	142	5.8 - 7	7.42 (20)	28	55
	8	5-11	141	3.5 - 6.5	7.42 (20)	27	65
	9	5-1	145	3 - 8	10.60 (20)	29	61
AEM	1	D-5	127	5.33 (Tone)	4.06 (5.33)	26	82
	2	D-6, D-7	143	5.33 (Tone)	4.06 (5.33)	28	61
	3	5-12, 6-2	132/142	2 - 5	7.60 (10)	27	72
	4	5-2, 5-3, 5-4	123/142	2.8 - 5.6	7.60 (10)	26	82
	5	D-1, D-2	128/146	1.5 (Tone)	1.14 (1.5)	28	72
	6	D-3, D-4	125/144	3.55 (Tone)	2.71 (3.55)	31	57
	7**						
	8	D-9	127/147	5.33 (Tone)	4.06 (5.33)	28	73
	9	5-13	133	2.8 - 5.6	7.60 (10)	29	61

*   When both low level and high level measurements were done, both source levels are given.

**   Experiment not completed.

CHAPTER 5

EXPERIMENTAL RESULTS AND COMPARISON WITH LINEAR THEORY

A. INTRODUCTION

In this chapter we present the results of the noise measurements.
Two experiments, JBL9 and AEM4, which exhibit the main features of the
nonlinear phenomena, are described in detail in the text. The novel
features of the remaining nine experiments are discussed. In each case
the measurements are compared with predictions based on linear theory
(Chapter 3). A comparison of the data with predictions based on nonlinear
theory (Chapter 3) is made in Chapter 6.

Several properties of the spectral information and its presentation
(see, for example, Fig. 5-1) are common to all the sets of data. First,
the spectra were obtained with a fixed bandwidth (typically 100 Hz)
spectrum analyzer (HP-3580A). As is always the case with such an analyzer,
measurements within a few bandwidths of zero frequency are not reliable.
Moreover, wind generated noise often contaminated measurements below
500 Hz. For these two reasons, the lower limit of useful data is about
500 Hz. When a measured spectrum was used as the starting point for a
theoretical prediction, the lower (suspect) end of the spectrum was
replaced by a gradual extrapolation to zero. Second, at high frequencies
the lower (SPL) limit of useful measurements is either 30 dB below the
middle horizontal grid line (indicated by tick marks) or the absolute level
SPL = 25 dB (100 Hz band), whichever is higher. The first limit is set by the
dynamic range of the spectrum analyzer, the second by other instrumentation noise
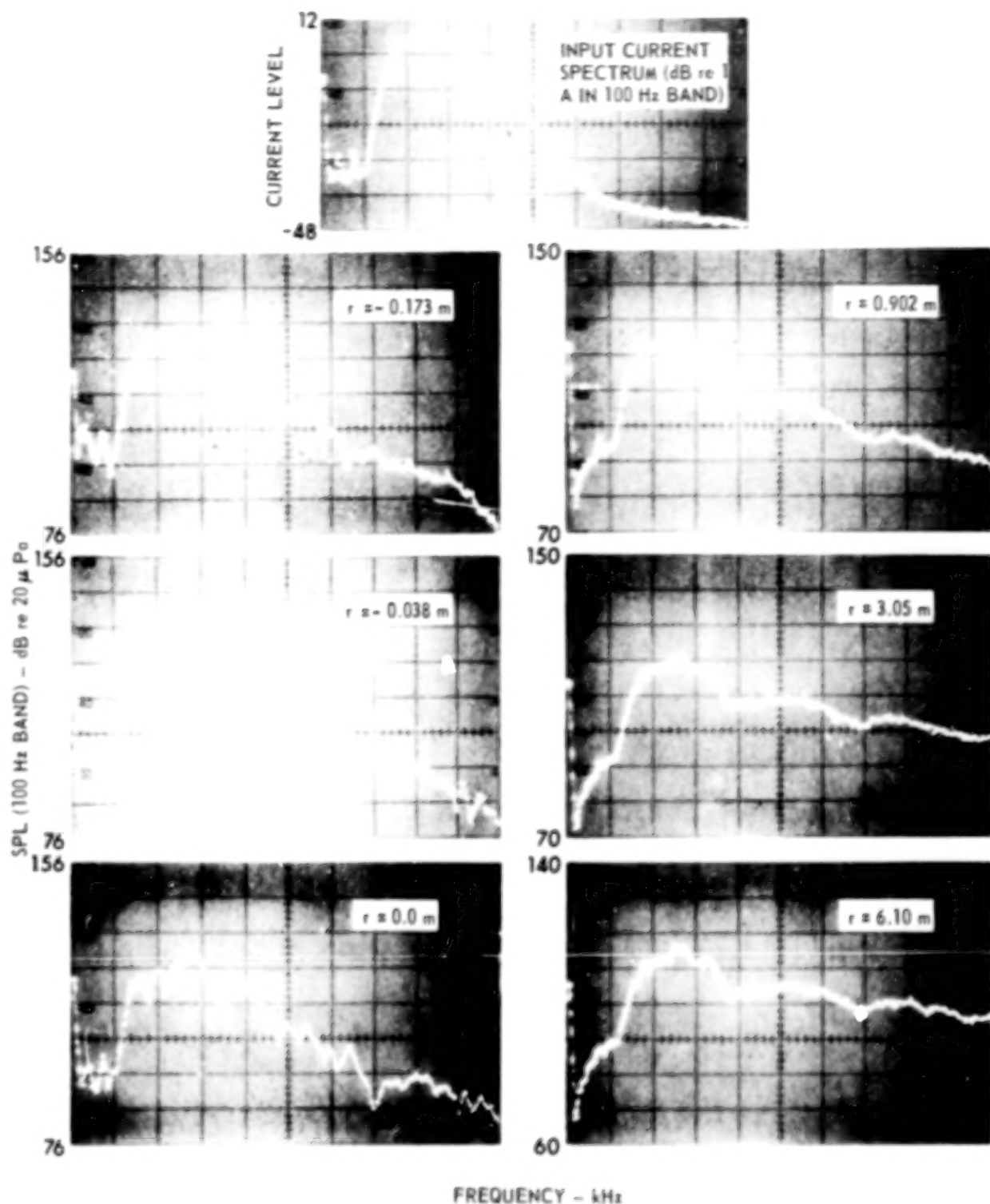in combination with ambient acoustic noise. Third, the distance $R_o(f_m)$ is

FIGURE 5-1a

SPECTRUM OF NOISE AS A FUNCTION OF RANGE r

TEN DRIVERS (EXPERIMENT JBL9)

R_0 (20 kHz) = 10.6 m, OASPL = 145 dB re 20 μPa at 1 m
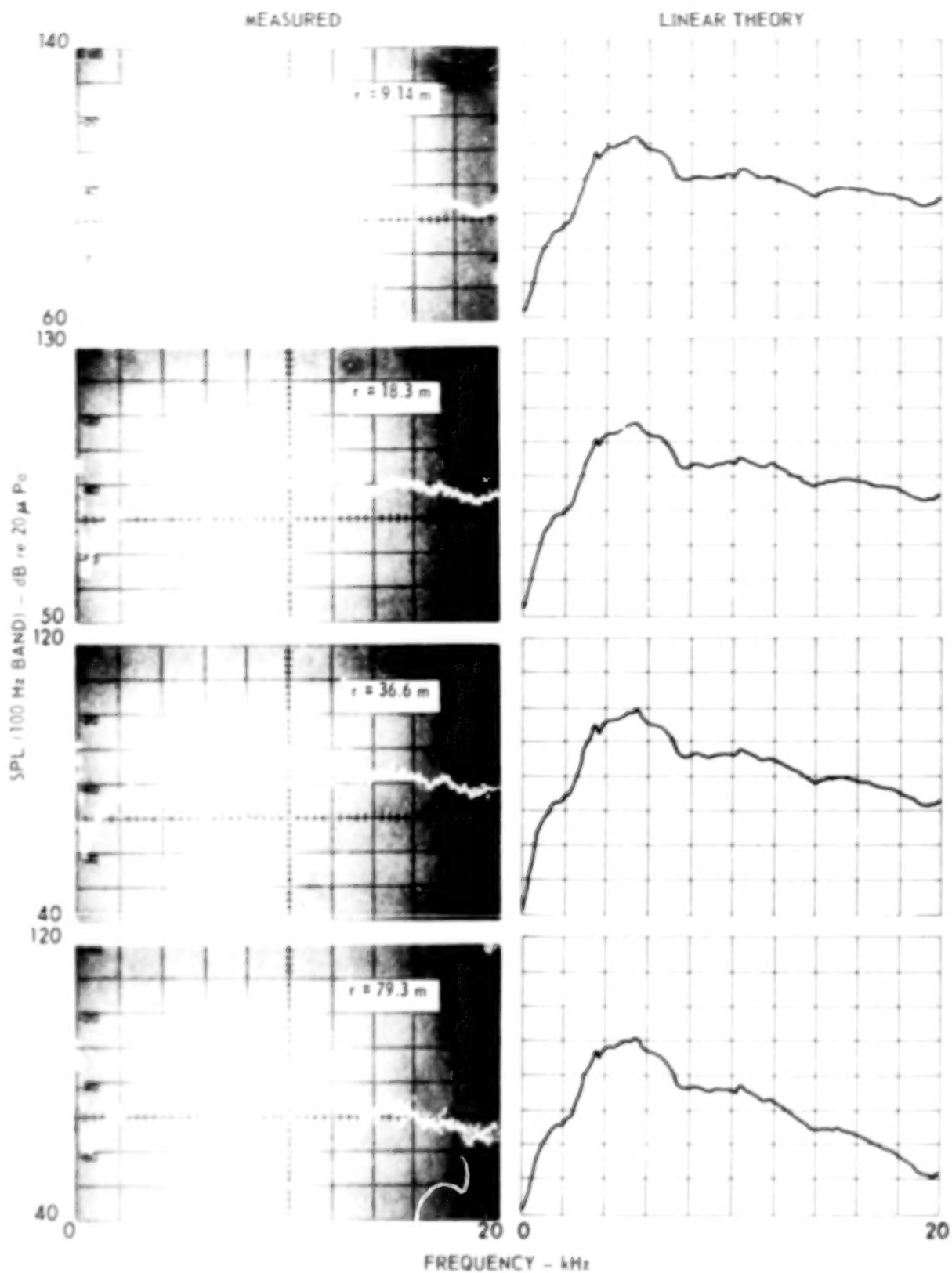
NOTE THAT EXPERIMENTAL DATA IS
SHOWN IN BOTH COLUMNS

FIGURE 5-1b
NOISE SPECTRUM AS A FUNCTION OF RANGE r
TEN DRIVERS (EXPERIMENT JBL9)
R_0 (20 kHz) = 10.6 m, OASPL = 145 dB re 20 μPa at 1 m

meant to represent the nearest point at which all significant spectral
components radiated by the source have reached the farfield. Since R_o
increases with frequency (see Eq. 3-4), f_m should be chosen to be the
highest frequency of interest present in the noise spectrum at the
aperture, in this case, the face of the transmitting array. In cases
where the aperture spectrum had been measured, f_m was so chosen. If
the aperture spectrum had not been measured, f_m was taken to be the
highest frequency in the spectrum analysis. Fourth, the indicated
value of OASPL is an effective source level at 1 m. It is equal
to $\text{OASPL}|_{r_o} + 20 \log_{10} r_o$, where r_o is normally the distance (in m) of the
first measurement point beyond $R_o(f_m)$. We justify the use of spherical
spreading to extrapolate back to 1 m by assuming that although the noise
wave distorts as it travels to r_o, little energy is actually lost.
That is, few if any shocks form, and ordinary absorption is small over that
distance. Finally, two different procedures were used in computing the
predictions based on linear theory, depending on whether the effect of
diffraction was included. When only spherical spreading and atmospheric
attenuation were taken into account, the starting spectrum for the calculations
had to be one measured in the farfield. The spectrum measured at r_o was used.
This procedure was followed for Figs. 5-1, 5-4 through 5-11, and 5-13.
When diffraction was also included, as in Figs. 5-3 and 5-12, the starting
spectrum was one measured inside one of the horns. Ordinary linear horn theory
was used to extrapolate to the horn mouth (the aperture), and Eq. 3-3 was used
to bridge the nearfield. Predictions are limited to ranges $r \geq r_o$.

B. EXPERIMENTAL RESULTS

A typical set of spectral measurements is shown in Fig. 5-1. The
spectrum of the array input current is shown at the top of Fig. 5-1a.

Because range was measured from the face of the array, negative values of
r signify points inside one of the horns. For the acoustic measurements
the ordinate is the SPL in a 100 Hz band (the indicated bandwidth in all
measurements reported here is the equivalent filter noise bandwidth) and
the abscissa is the filter center frequency. The data in the left column
of Fig. 5-1a are for points inside the horn. In the right column
the measurement point was in the nearfield for most of the spectral components.
For Fig. 5-1b all the points were in the farfield. In the horn and in
the nearfield, the growth with distance of the high frequency portion
of the spectrum is evident. The growth is caused by both nonlinear
distortion and diffraction. In Fig. 5-1b a comparison is made of the
farfield data with linear theory [in this case 9.14 m was used as
the value of r_o even though that value is slightly less than $R_o(f_m)$].
The linear theory predictions of the most intense part of the spectrum
(approximately 3 kHz to 7 kHz) agree well with the measurements. At
higher frequencies however, the data rise above the predicted levels;
the discrepancy increases with range and frequency. At the 79.3 m point,
for example, the measured level exceeds the predicted level by 2 dB
at 10 kHz, 6 dB at 15 kHz, and 15 dB at 20 kHz. This behavior is typical
of that observed in all the experiments. A slight amount of low frequency
growth may also be noticed even though the spectral range over which
comparisons may be made is very limited. At 1 kHz, for example, the
measured level is about 5 dB above the prediction based on linear theory.

A comparison of low and high level noise spectra is shown in Fig. 5-2.
The low level spectra are on the left, the high level on the right.
The same input noise, a 1/2 octave band centered at 4 kHz (first row in
Fig. 5-2a), was used for both sets of measurements, but the input level
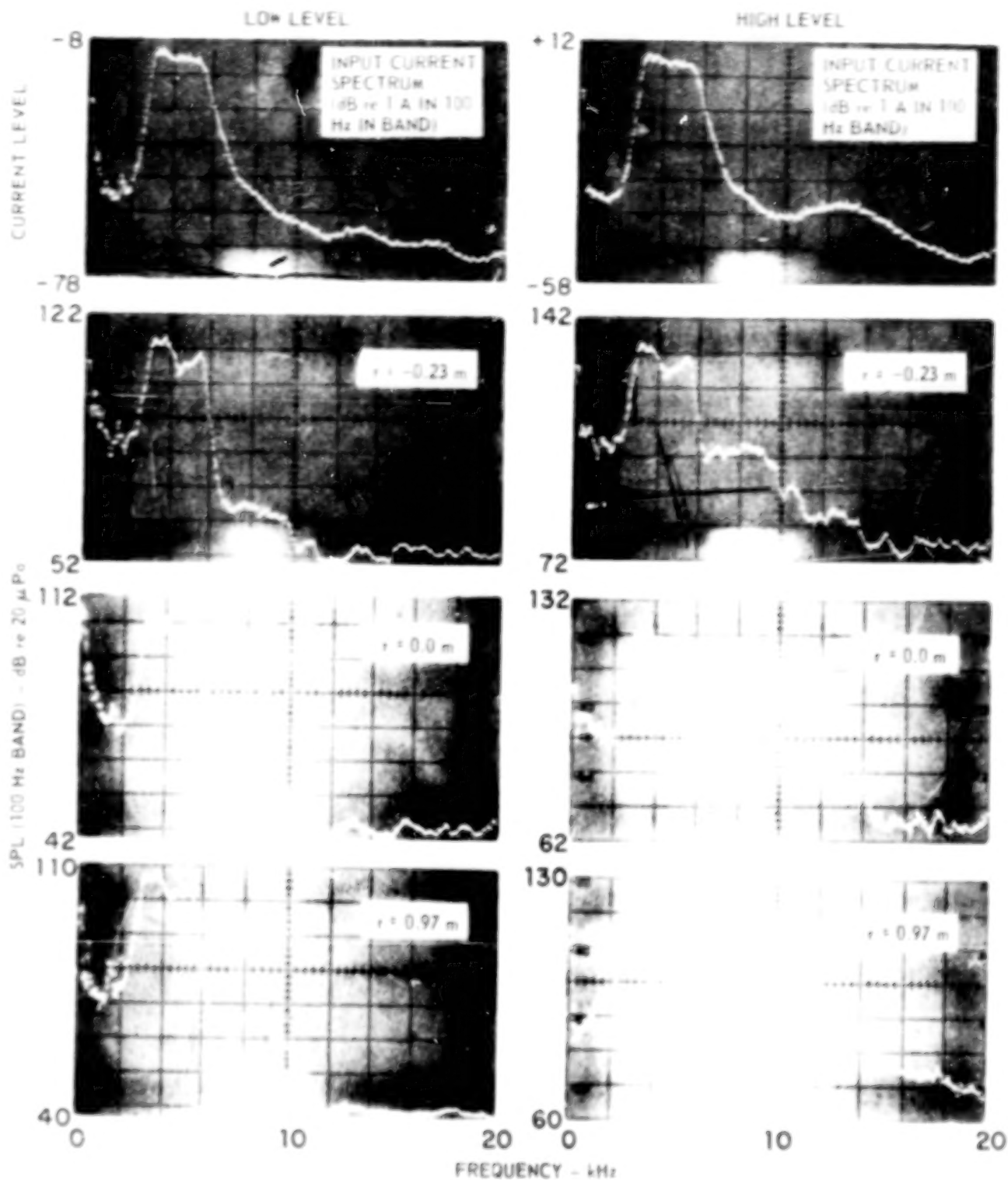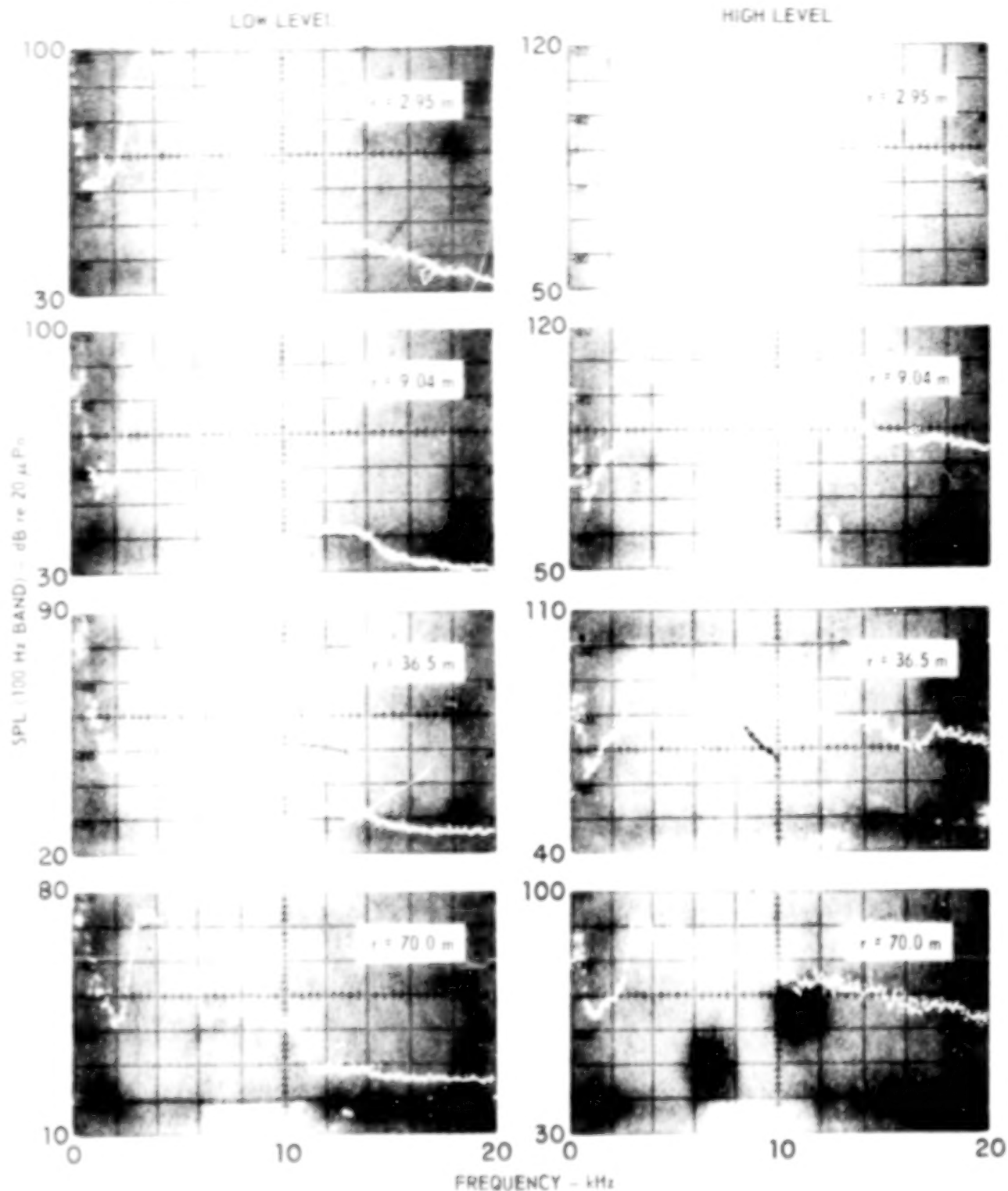was raised approximately 20 dB for the high level set.

FIGURE 5-2a
COMPARISON OF MEASURED LOW AND HIGH LEVEL NOISE
SPECTRA (EXPERIMENT AEM4). THE MAXIMUM AMBIENT
NOISE LEVEL FOR FREQUENCIES GREATER THAN 1 kHz
IS APPROXIMATELY 25 dB (100 Hz BAND) re 20 μPa

R_0(10 kHz) = 7.6 m
LOW LEVEL   OASPL = 123 dB at 1 m
HIGH LEVEL   OASPL = 142 dB at 1 m

FIGURE 5-2b

COMPARISON OF MEASURED LOW AND HIGH LEVEL NOISE
SPECTRA (EXPERIMENT AEM4). THE MAXIMUM AMBIENT
NOISE LEVEL FOR FREQUENCIES GREATER THAN 1 kHz
IS APPROXIMATELY 25 dB (100 Hz BAND) re 20 μPa

R_0(10 kHz) : 7.6 m

LOW LEVEL   OASPL : 123 dB at 1 m

HIGH LEVEL   OASPL : 142 dB at 1 m

The second row shows the acoustic spectra inside one of the horns (r = -0.23 m);
the OASPL there was 126 dB for the low level noise and about 145 dB for
the high level noise. Inspection of the remaining spectra in Fig. 5-2
shows the following. Even for the low level noise, nonlinear propagation
distortion was not negligible. There is a clearcut growth of the second
harmonic band and even a development of a third harmonic band. Inside
the horns the second harmonic band is about 45 dB below the fundamental
band; at 70 m the two bands are only 20-25 dB apart. The high level
data shows a much greater effect of nonlinearity. There is a robust
growth of the entire spectrum above the original 4 kHz band. Even at
20 kHz, where atmospheric absorption is strong, the growth is impressive.
Inside the horns the signal at 20 kHz is in the instrumentation noise,
at least 60 dB below the fundamental band. At 70 m, however, the 20 kHz
signal is within 30 dB of the fundamental band. To put it another way,
the 20 kHz level is about the same at 70 m as it seems to be at 0 m.
Again a small but noticeable low frequency growth may be discerned. A'
70 m the 1 kHz level is closer to the spectral peak in the measurement
made at high level than in the one at low level.

Thus far we have said that both diffraction and nonlinear effects
are responsible for forming the broadband spectrum observed at the end of
the array nearfield. To quantitatively assess the importance of
each of these effects, we have computed farfield spectra based on linear
diffraction theory (see Eq. 3-3). The results of the computation are
compared with data in Fig. 5-3. (The data are simply a repeat of the last
three rows in Fig. 5-2b plus a measurement at 18.2 m that was omitted from
Fig. 5-2.) In both the low and high level cases, the prediction matches the
data well within the original octave band. At higher frequencies, however,
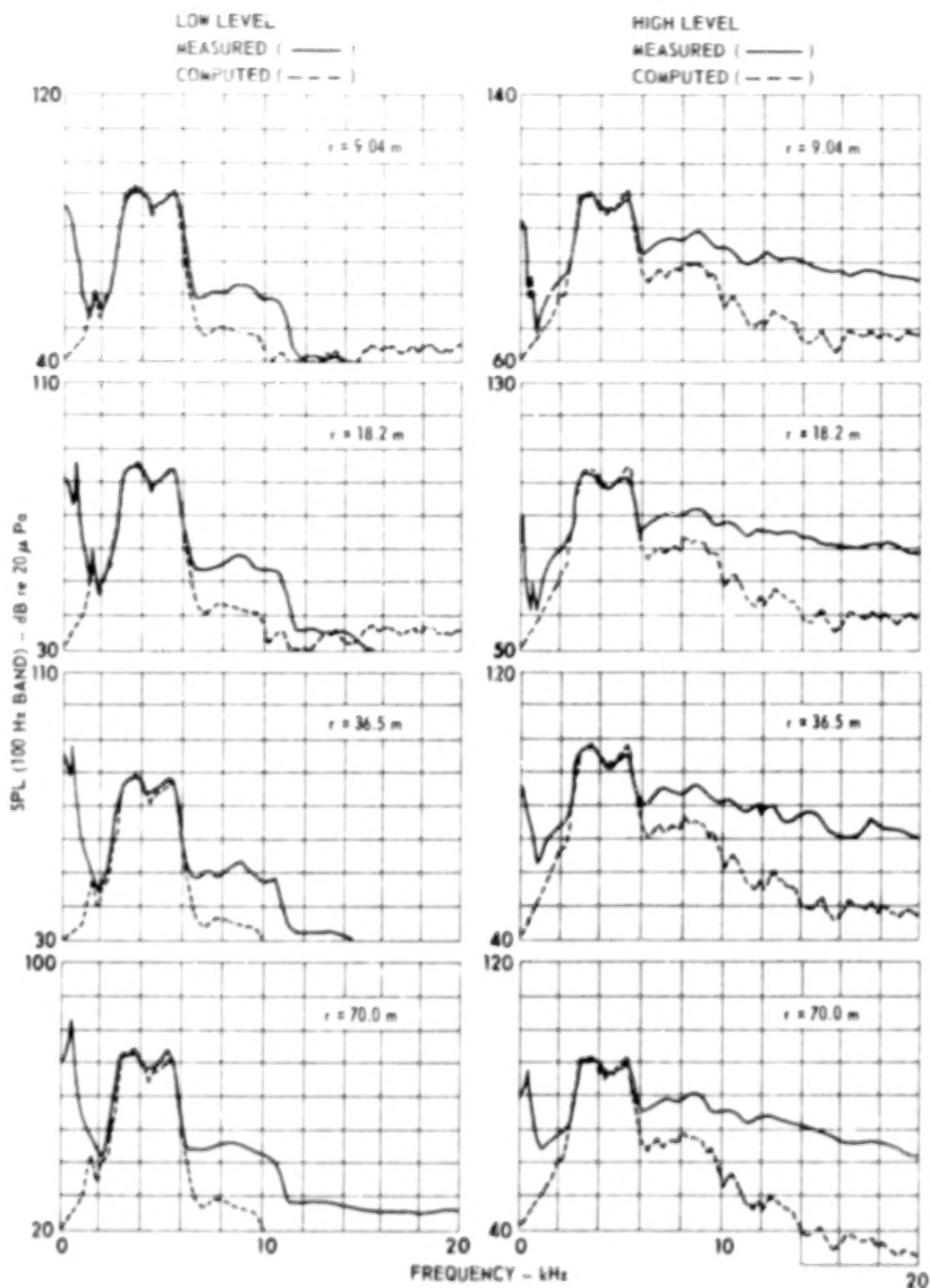
FIGURE 5-3
ESTIMATES OF THE EFFECT OF DIFFRACTION
ON FARFIELD SPECTRA (EXPERIMENT AEM4)

THE COMPUTED SPECTRA WERE OBTAINED BY
APPLYING LINEAR HORN AND DIFFRACTION
THEORY TO THE r = 0.23 m SPECTRUM OF Fig. 5-2

the prediction falls well below the data. On the basis of this observa-
tion, we conclude that the observed spectral growth in the nearfield far
exceeds that which would be due to diffraction alone. Furthermore, because
the spectral growth is much more pronounced for the high level data, we
conclude that it is caused by nonlinear propagation distortion.

Another view of the same experiment (high level measurements only)
is presented in Fig. 5-4. Here propagation curves for specific 100 Hz
bands are shown. The data were obtained from the high level spectrograms
by reading the band levels as a function of range. The solid curves are
predictions based on linear theory (spherical spreading and atmospheric
attenuation). The 3.8 kHz band (approximately the spectral peak) decays
in accordance with the prediction. For the higher frequency bands, however,
the agreement becomes progressively poorer with both frequency and distance.
At 70 m, for example, the bands at 8, 14, and 20 kHz are approximately 3, 9,
and 15 dB, respectively, above the linear theory predictions. It is also
significant that the divergence between data and linear theory shows no
sign of slackening, even at the greatest range. In other words, there
is no evidence in this experiment that small-signal theory will eventually
triumph.

Figure 5-5 shows noise spectra recorded to 50 kHz. The input signal
to the array was a 1/1 octave band of noise centered at 4 kHz. Once more,
linear theory provides a good description of the behavior of the original
octave band but a poor one of the behavior of the high frequency noise.
Moreover, the discrepancy between linear theory and measurement again gets
progressively worse with both increasing frequency and distance. For
example, holding distance fixed at 79.3 m, we find the discrepancy is about
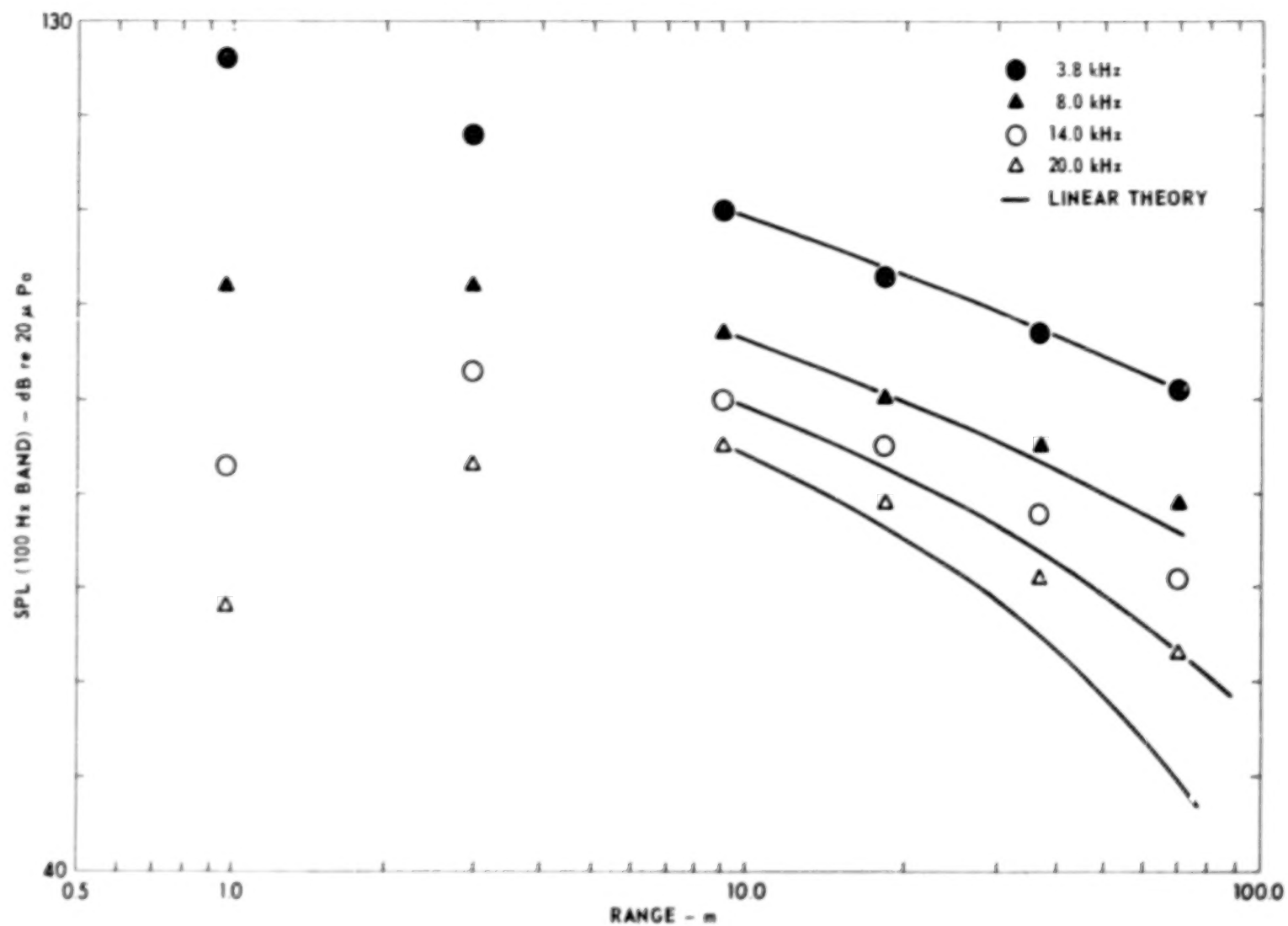4 dB at 10 kHz, 15 dB at 20 kHz, 30 dB at 30 kHz, and 40 dB at 35 kHz.

FIGURE 5-4
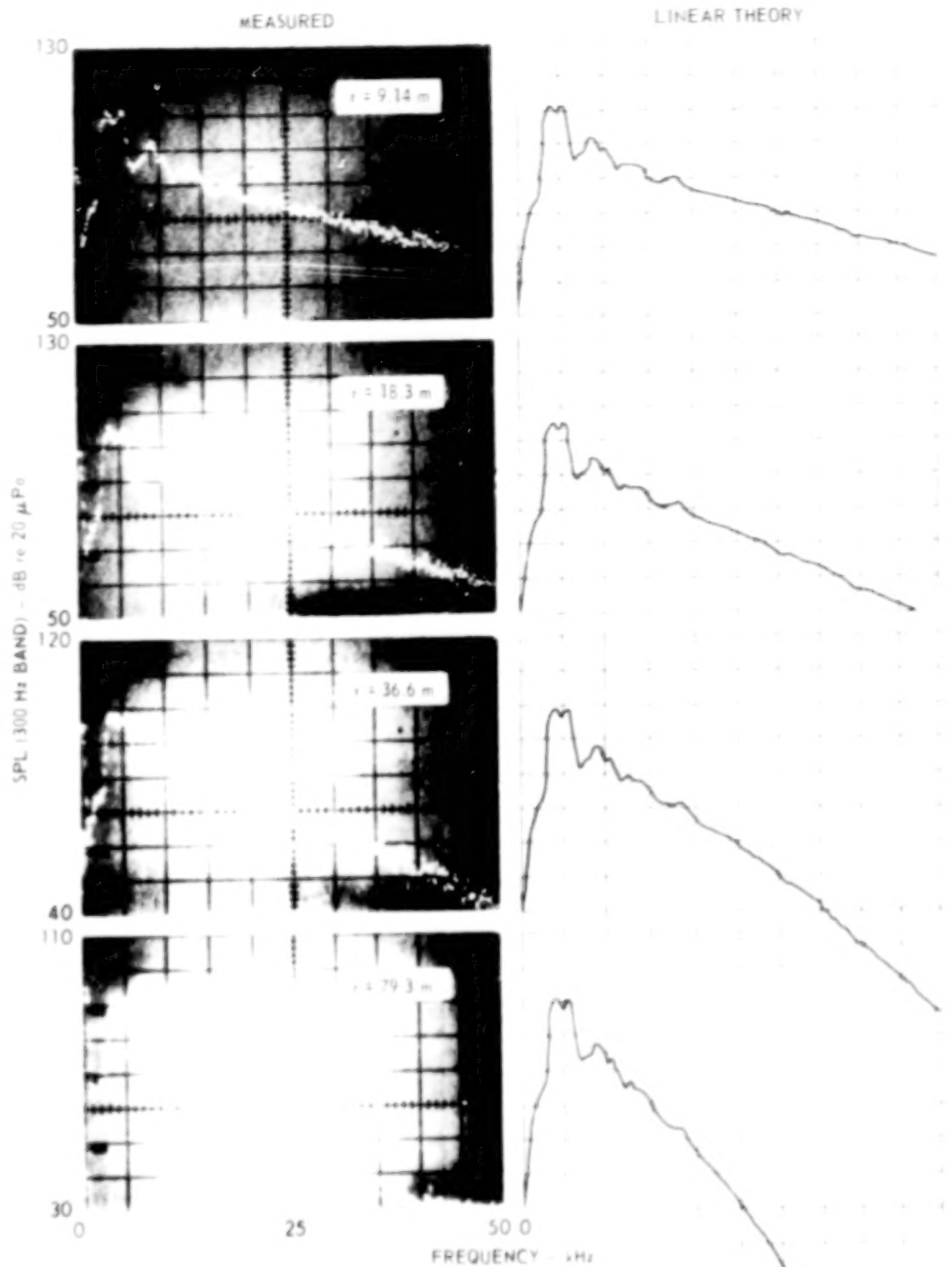PROPAGATION CURVES FOR EXPERIMENT AEM4 (HIGH LEVEL)

SPL (300 Hz BAND) - dB re 20 μPa

FIGURE 5-5
NOISE SPECTRUM AS A FUNCTION OF RANGE r
SEVEN DRIVERS (EXPERIMENT JBL5)
R_0 (20 kHz) = 7.42 m, OASPL = 140 dB re 20 μPa at 1 m

At fixed frequency, say 25 kHz, the discrepancy is about 5 dB at 18.3 m, 10 dB at 36.6 m, and 20 dB at 79.3 m. In other words, even at the greatest distance, the divergence between linear theory and measured data continues to increase.

Figure 5-6 shows results for the first experiment done. A single horn driver was used. Because of the broad initial spectrum, the low source level, and the low upper limit of the spectrogram, only minor non-linear distortion is visible, and it is restricted to the very upper limit of the spectrum, 7.5 to 10 kHz. This result is not surprising. Because the source level is low, the distortion components are weak. Moreover, the broad initial spectrum serves to mask the distortion components produced. The good agreement of the linear theory prediction and data within the original spectral band (approximately 1 to 7 kHz) shows that the linear theory model is suitable for low level signals.

In Figs. 5-7, 5-8, 5-11, and 5-9 the initial spectral bands are approximately the same but the value of source OASPL gradually increases: 127 dB, 132 dB, 141 dB, and 144 dB, respectively. As the source level is increased, it is apparent that the distortion occurring in the trans-mitter nearfield is increased. For example, at 9.14 m the 20 kHz level is about 35 dB below the spectral peak in Fig. 5-7, but only 19 dB below in Fig. 5-9. An observation that is puzzling at first glance is that linear theory seems to work better for the higher level experiments than for the lower level ones. Compare, for example, the difference between the linear theory predictions and the measurements at 20 kHz for the 77 m and 79.3 m data of Figs. 5-7 and 5-9, respectively. The difference is about 17 dB for Fig. 5-7 but only 10 dB for Fig. 5-9. The reason for this apparent anomaly is that the nearfield distortion, which is much greater in the high level experiment, tends to partially mask the distortion

65

components produced in the farfield. Although the farfield distortion components are much weaker in the low level experiment (Fig. 5-7), they have comparatively good visibility because the spectrum emerging from the nearfield (1.07 m) is much "cleaner" than in the high level experiment.

The results of a narrowband experiment (a 1/3 octave band at 6.3 kHz) are shown in Fig. 5-10. The successive major spectral peaks are those of the fundamental, second, and third harmonics. Notice how well developed are the higher harmonic bands when the noise emerges from the nearfield. The discrepancy between linear theory and measurement is not large in this experiment, but it does increase with harmonic number; at 73.2 m it is about 4 dB for the second harmonic band and about 10 dB for the third harmonic band. The behavior of this discrepancy is in line with predictions based on the perturbation solution for tones. A weak difference frequency band centered at about 700 Hz may also be seen. At r = 9.14 m this signal was at least partly due to direct radiation from the electroacoustic source. The signal is, however, augmented (relative to the linear theory prediction) as it propagates from 9.14 m to 73.2 m.

The data shown in Fig. 5-12a are similar to those in Fig. 5-2 except that in Fig. 5-12a the difference in OASPL between the low and high level experiments is 10 dB, not 20 dB. In addition, the initial bandwidth of the noise was somewhat narrower than in the other experiment. The spectra in the bottom row of Fig. 5-12a are overlays of spectra measured inside the horn and at 9.04 m; they show how extensive the nearfield distortion becomes when the level is raised just 10 dB. Figure 5-12b shows the farfield spectra but only for the high level expeirment. The spectra in the right column were obtained by applying linear horn
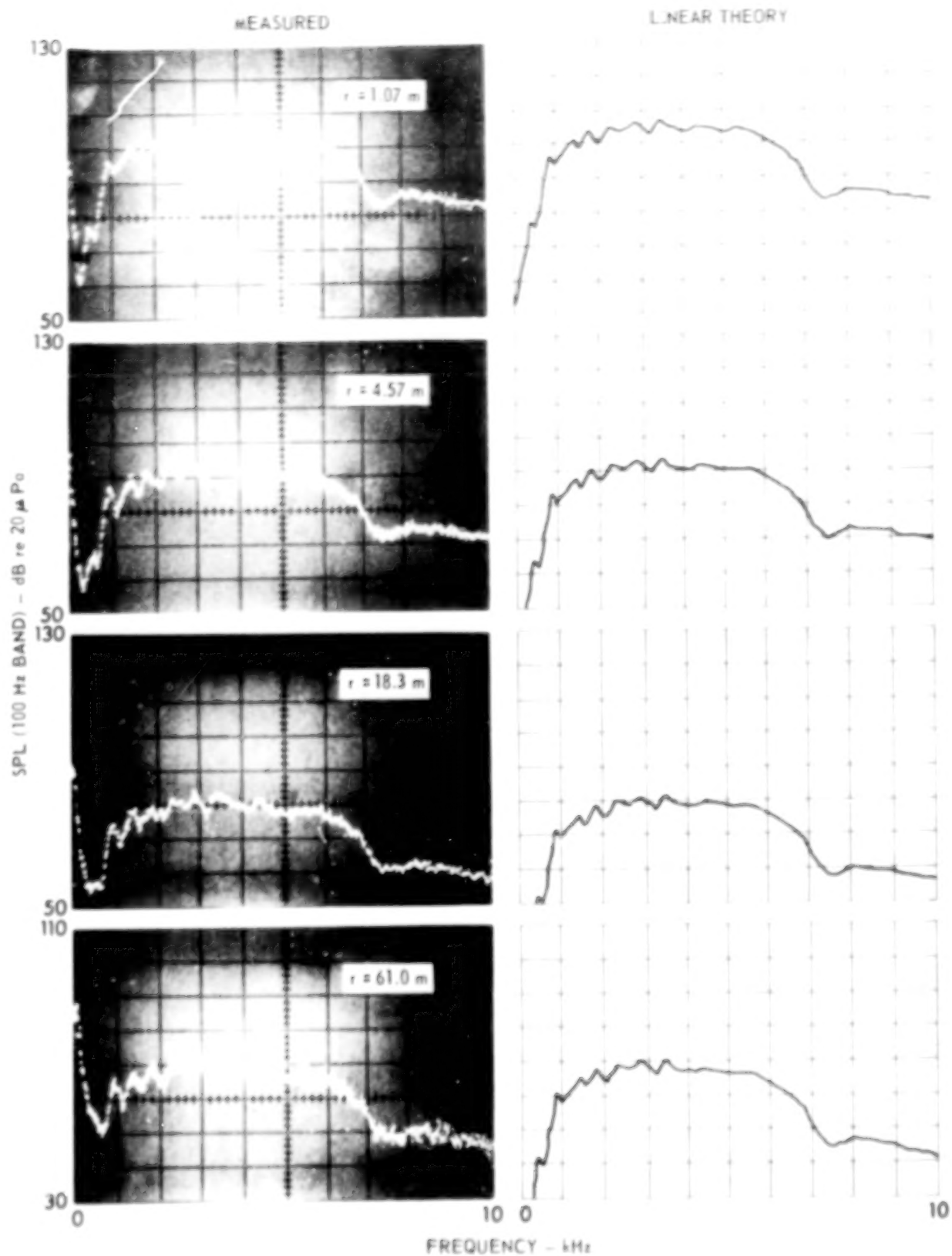
FIGURE 5-6
NOISE SPECTRUM AS A FUNCTION OF RANGE r
SINGLE DRIVER (EXPERIMENT JBL1)
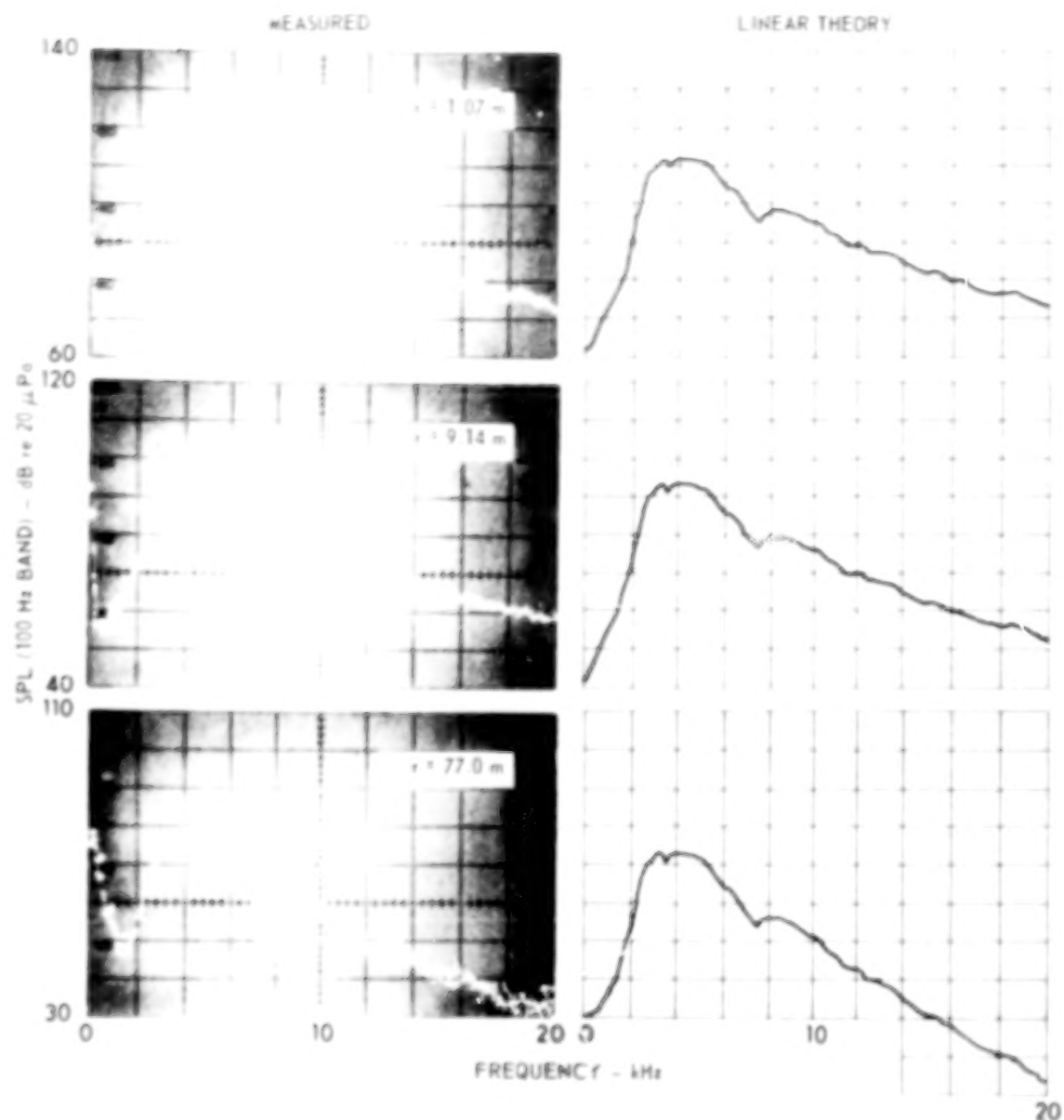
R_0 (10 kHz) = 0.53 m, OASPL = 121 dB re 20 μ Pa at 1 m

67

FIGURE 5-7
NOISE SPECTRUM AS A FUNCTION OF RANGE r
SINGLE DRIVER (EXPERIMENT JBL2)
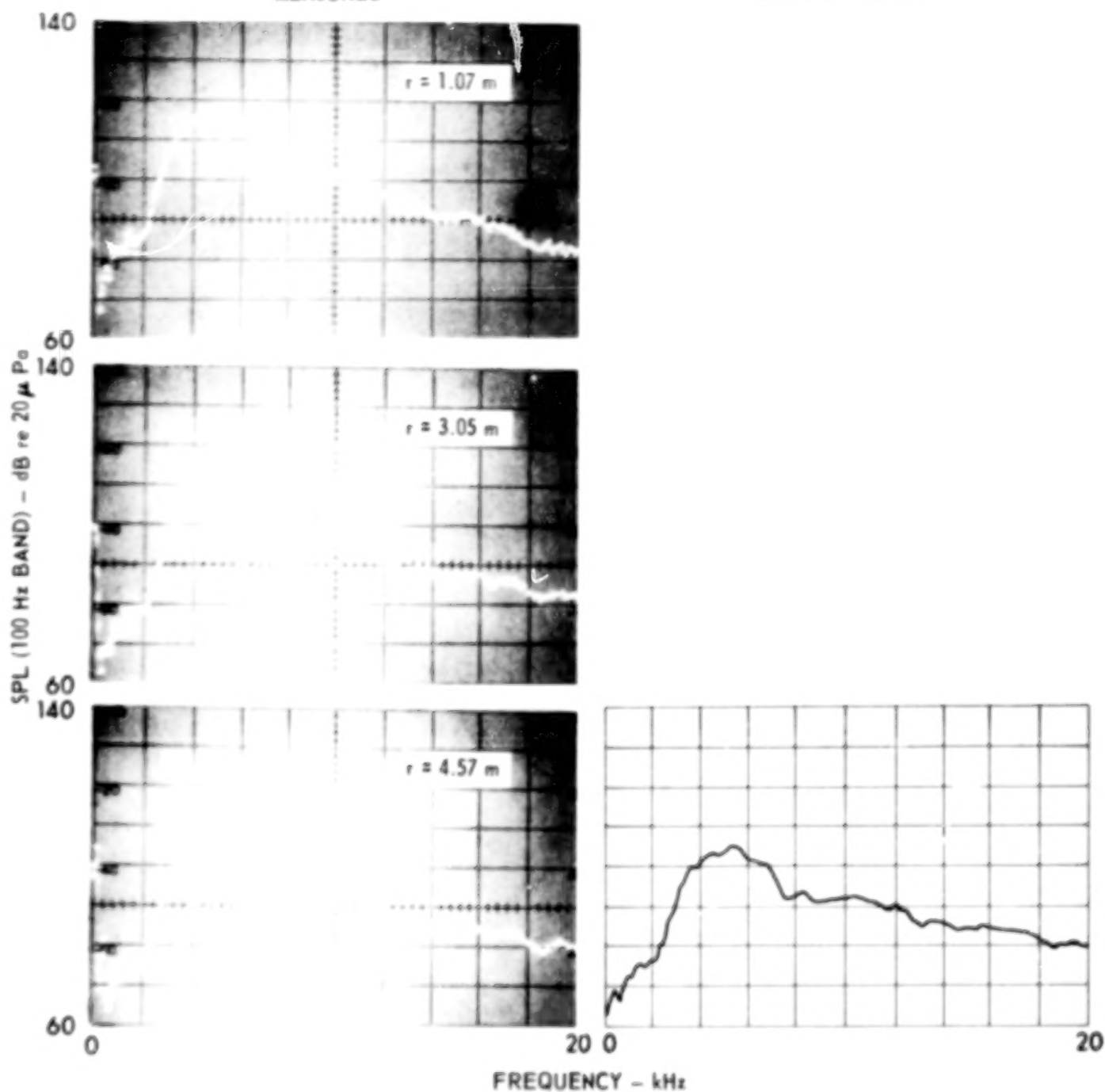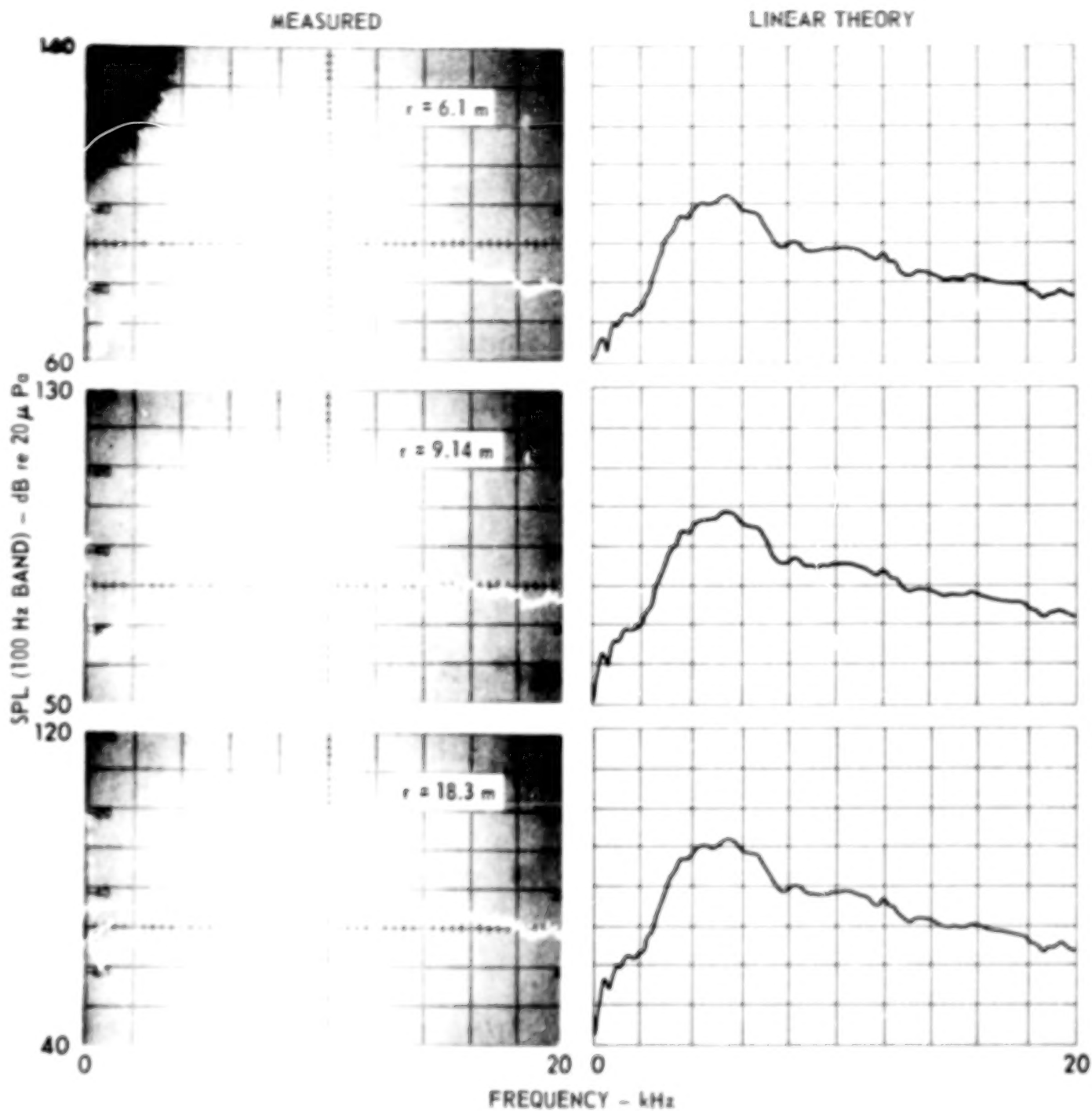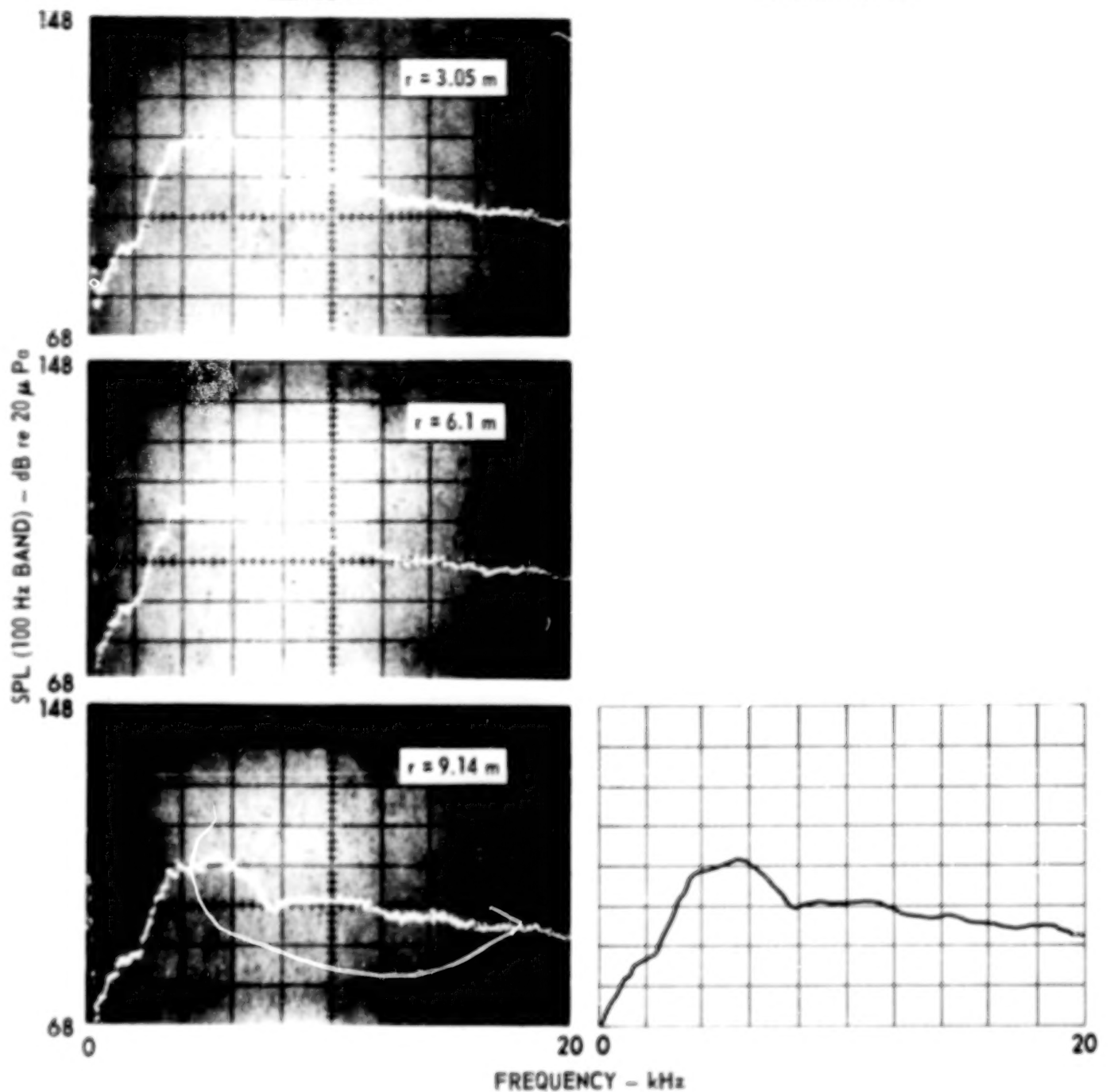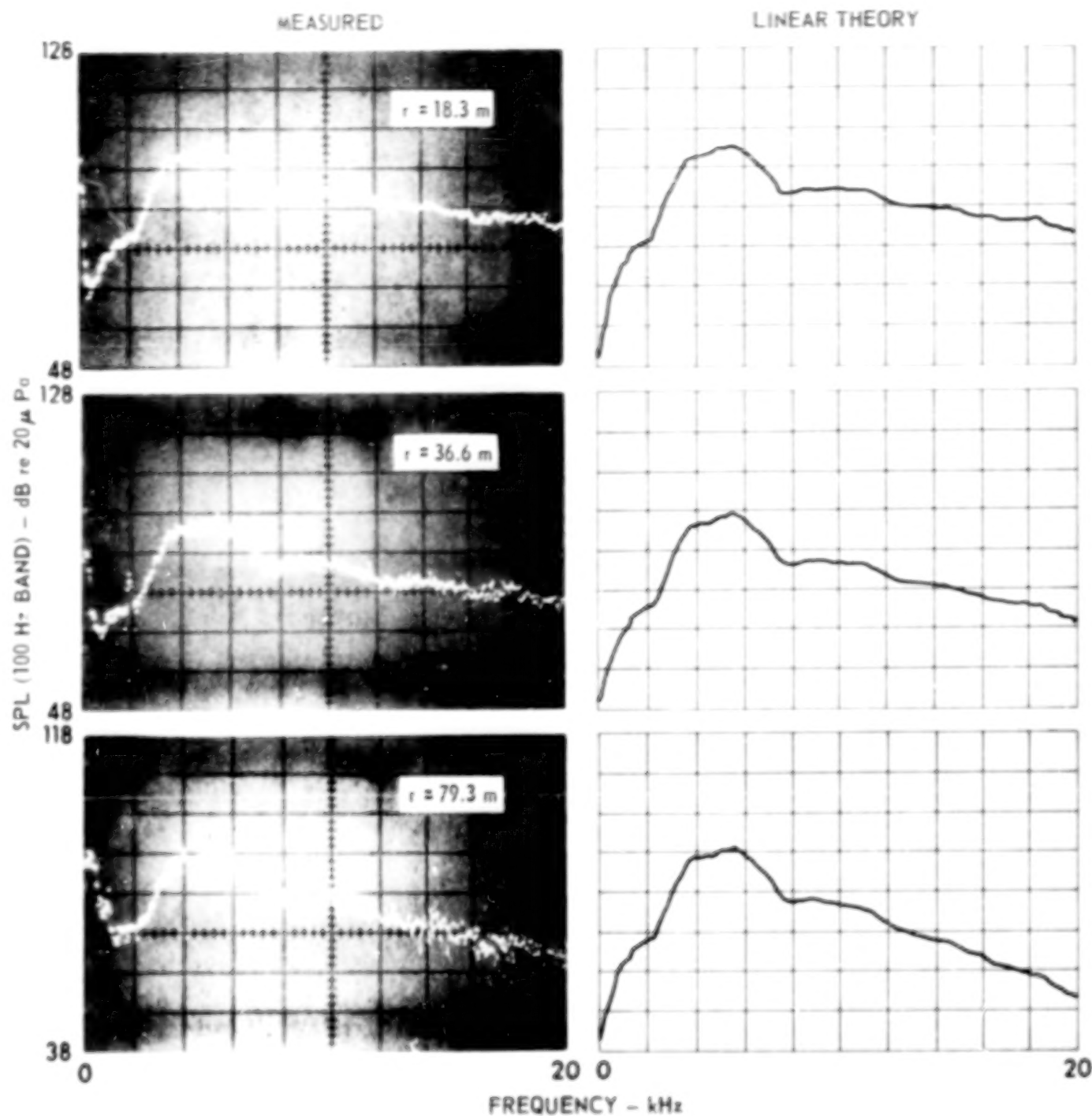R_0 (20 kHz) = 1 06 m, OASPL = 127 dB re 20 μPa at 1 m

FIGURE 5-8a

NOISE SPECTRUM AS A FUNCTION OF RANGE r
THREE DRIVERS (EXPERIMENT JBL3)

R (20 kHz) = 3.18 m, OASPL = 132 dB re 20 μPa at 1 m

FIGURE 5-8b
NOISE SPECTRUM AS A FUNCTION OF RANGE r
THREE DRIVERS (EXPERIMENT JBL3)
R_0 (20 kHz) = 3.18 m, OASPL = 132 dB re 20 μPa at 1 m

FIGURE 5-9a
NOISE SPECTRUM AS A FUNCTION OF RANGE r
SEVEN DRIVERS (EXPERIMENT JBL4)
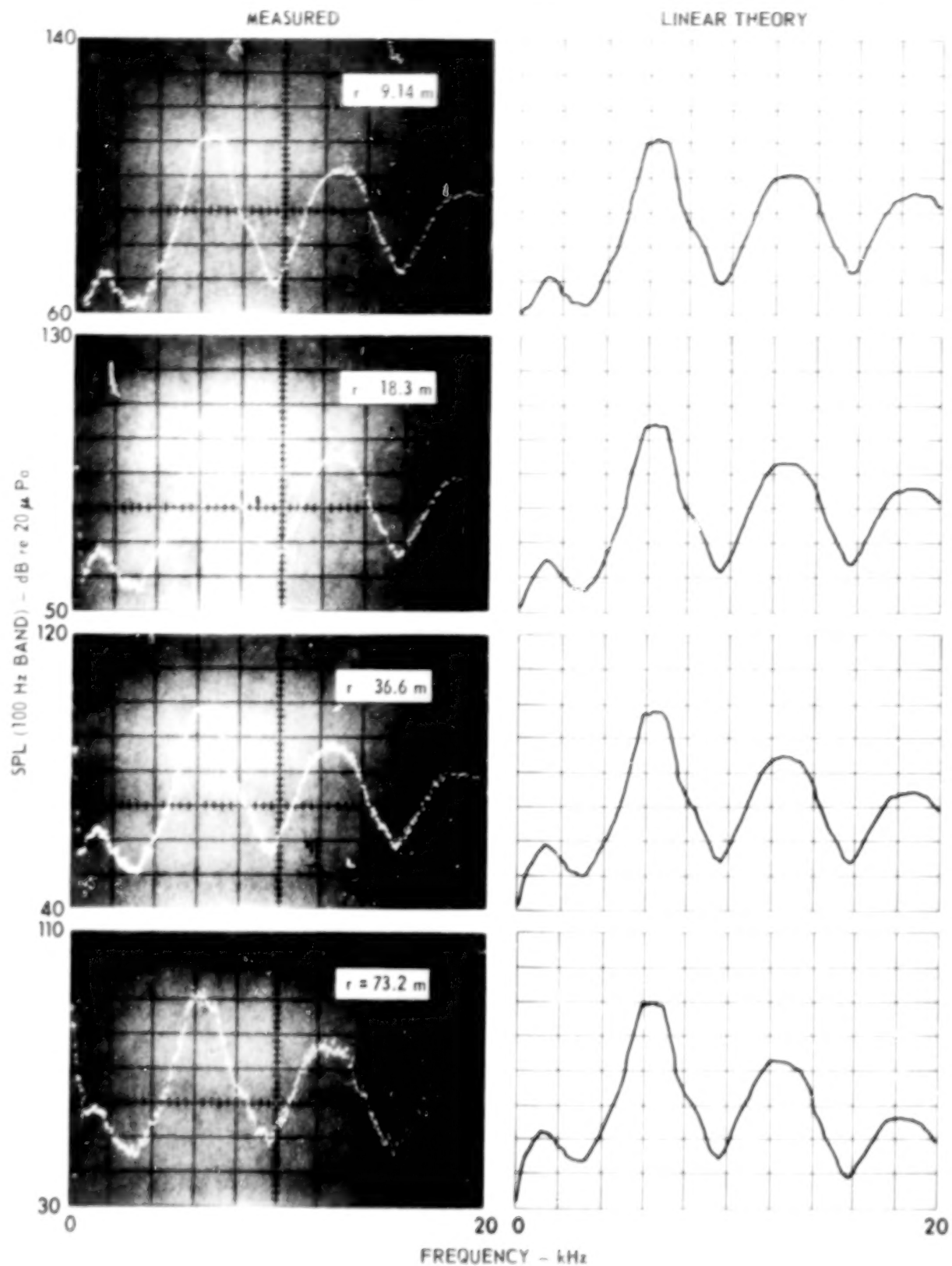R_0 (20 kHz) = 7.42 m, OASPL = 144 dB re 20 μ Pa at 1 m

FIGURE 5-9b
NOISE SPECTRUM AS A FUNCTION OF RANGE r
SEVEN DRIVERS (EXPERIMENT JBL4)
R_0 (20 kHz) = 7.42 m, OASPL = 144 dB re 20 μPa at 1 m

FIGURE 5-10
NOISE SPECTRUM AS A FUNCTION OF RANGE r
SEVEN DRIVERS (EXPERIMENT JBL7)

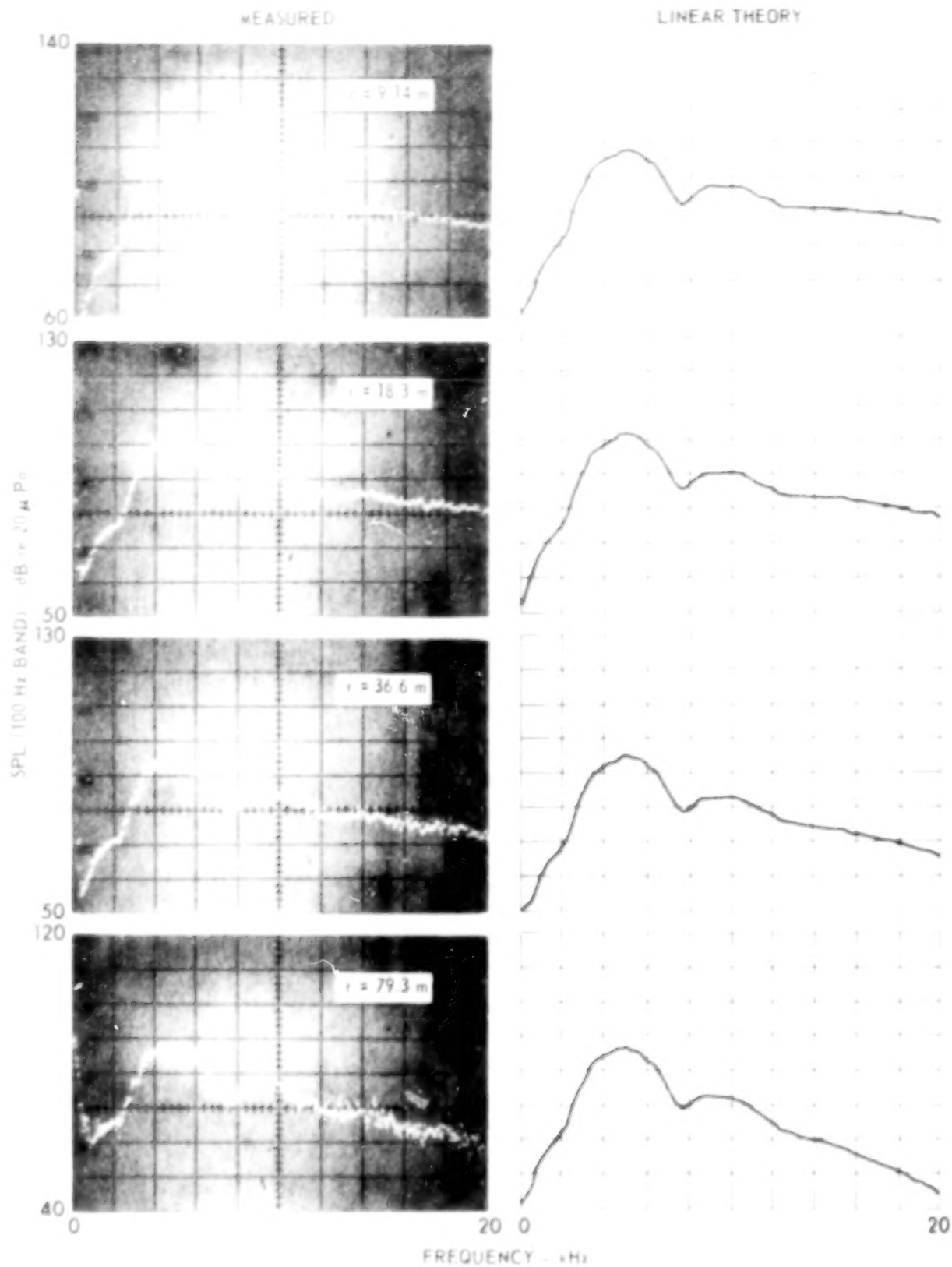R_0 (20 kHz) = 7.42 m, OASPL = 142 dB re 20 μPa at 1 m

73

FIGURE 5-11

NOISE SPECTRUM AS A FUNCTION OF RANGE r

SEVEN DRIVERS (EXPERIMENT JBL8)

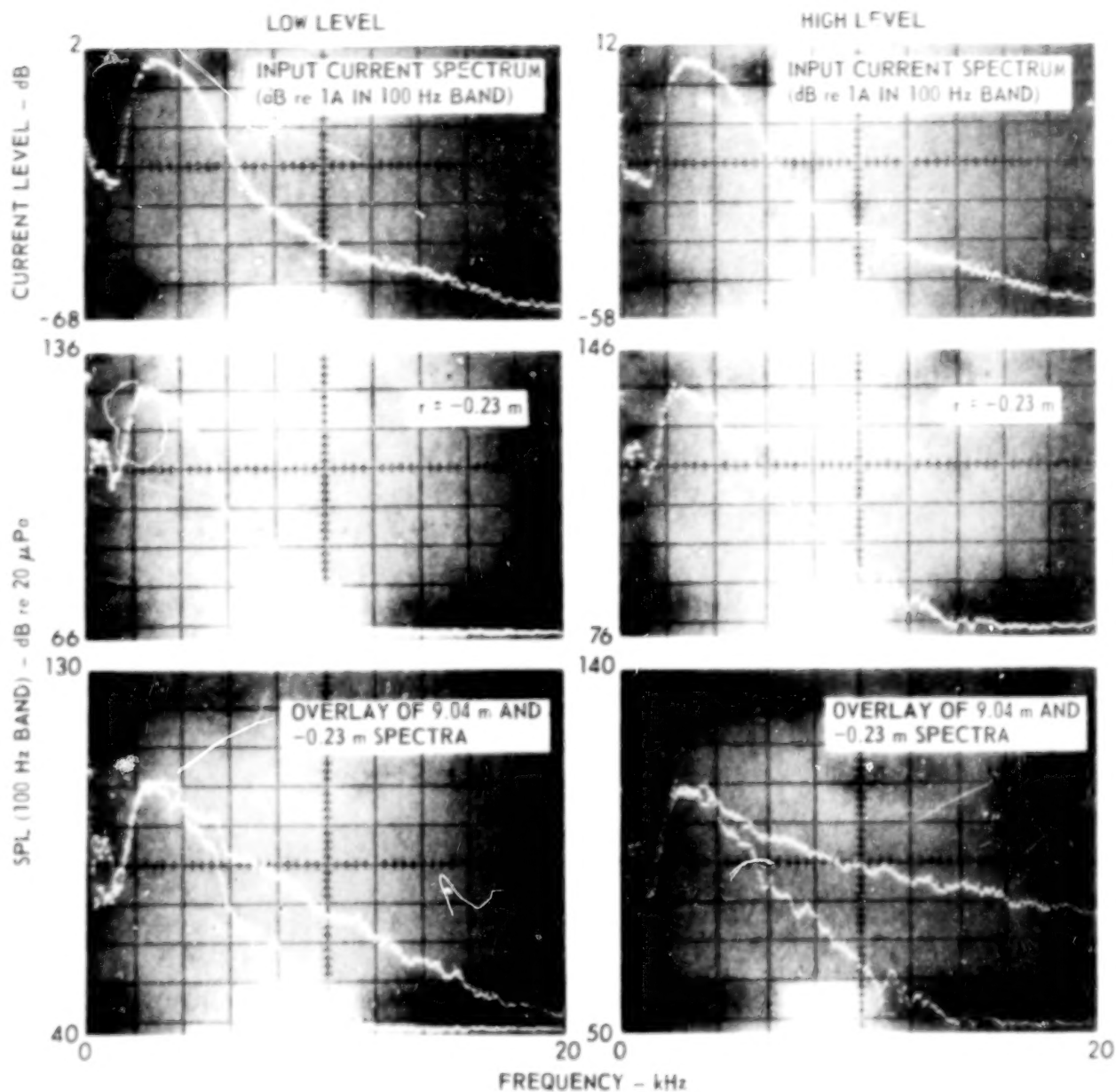R_0 (20 kHz) = 7.42 m, OASPL = 141 dB re 20 μPa at 1 m

FIGURE 5-12a
COMPARISON OF MEASURED LOW AND HIGH
LEVEL NOISE SPECTRA (EXPERIMENT AEM3)

FOR THE DATA IS THE LAST ROW THE $r = -0.23$ m SPECTRA
HAVE BEEN SHIFTED UPWARD FOR COMPARISON PURPOSES

R_0 (10 kHz) = 7.6 m
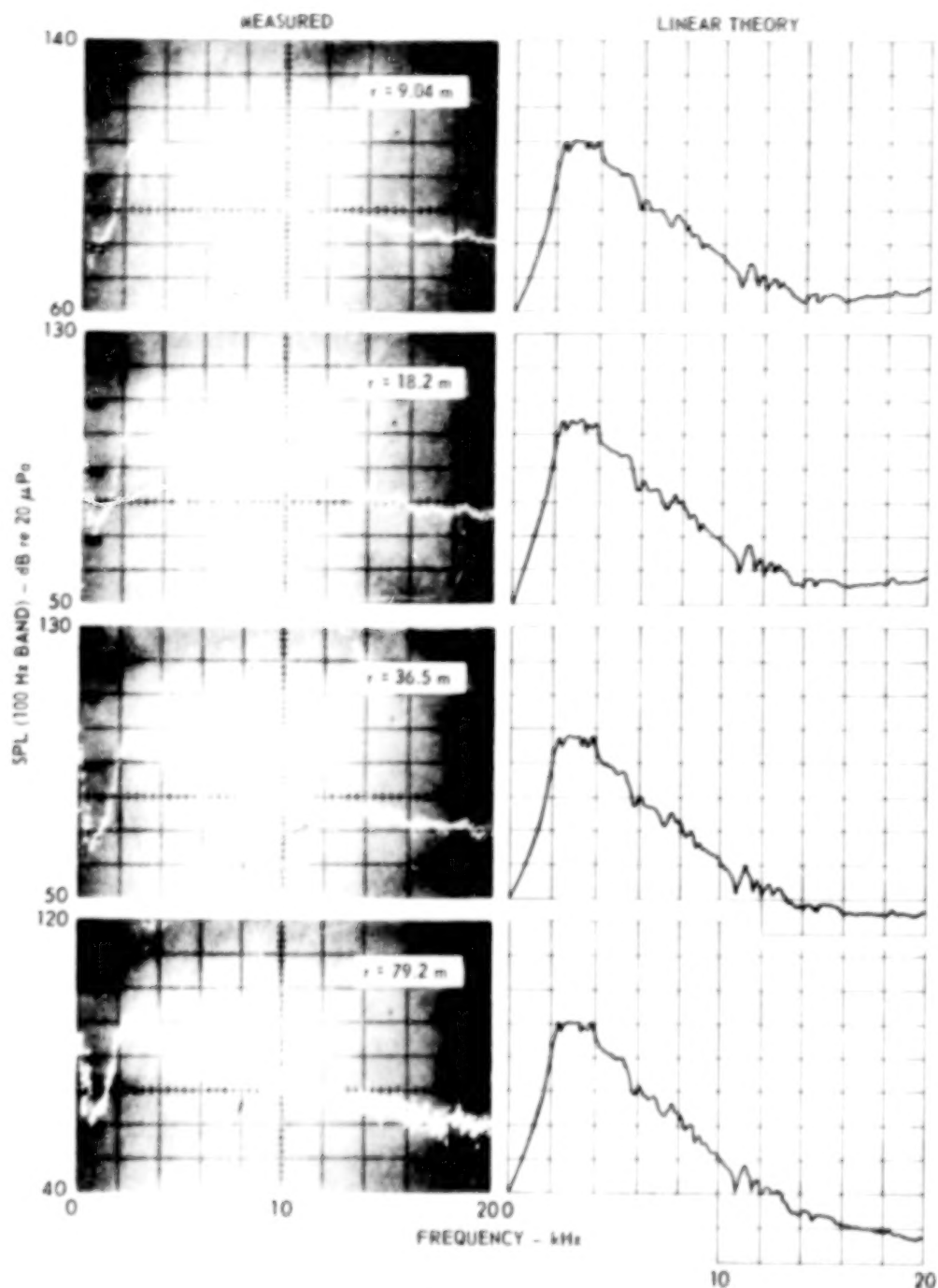LOW LEVEL: OASPL = 132 dB at 1 m
HIGH LEVEL: OASPL = 142 dB at 1 m

75

FIGURE 5-12b

ESTIMATES OF THE EFFECT OF DIFFRACTION
ON FARFIELD SPECTRA (EXPERIMENT AEM3)

THE COMPUTED SPECTRA WERE OBTAINED BY
APPLYING LINEAR HORN AND DIFFRACTION
THEORY TO THE $r = 0.23$ m SPECTRUM OF Fig. 5-12a

$R_0(10$ kHz$) = 7.6$ m, OASPL $= 142$ dB re 20 μPa at 1 m

and diffraction theory to the spectrum measured inside the horn
(r = -0.23 m). The 14-20 kHz portions of the computed spectra are
too high because they are based on nonacoustic signals in the

starting spectrum. That is, the 14-20 kHz portion of the spectrogram at
-0.23 m represents instrumentation noise, not sound. Even discounting the
erroneous prediction at the high end of the spectrum, however, comparison
of the measured and predicted spectra at 9.04 m shows that much distortion
occurred in the nearfield. In the farfield the discrepancy continues to
grow. For example, the discrepancy at 10 kHz is successively 14 dB, 17 dB,
19 dB, and 21 dB as range increases. No sign of any leveling off to a
constant discrepancy appears.

The experiment depicted in Fig. 5-13 is similar to that in Fig.
5-2, but at an intermediate source level. The stairstep appearance of the
nearfield spectra is due to a relatively good resolution of the harmonic bands.
The resolution breaks down as distance increases because the buildup of inter-
modulation components fills in most of the sharp breaks in the spectrum.
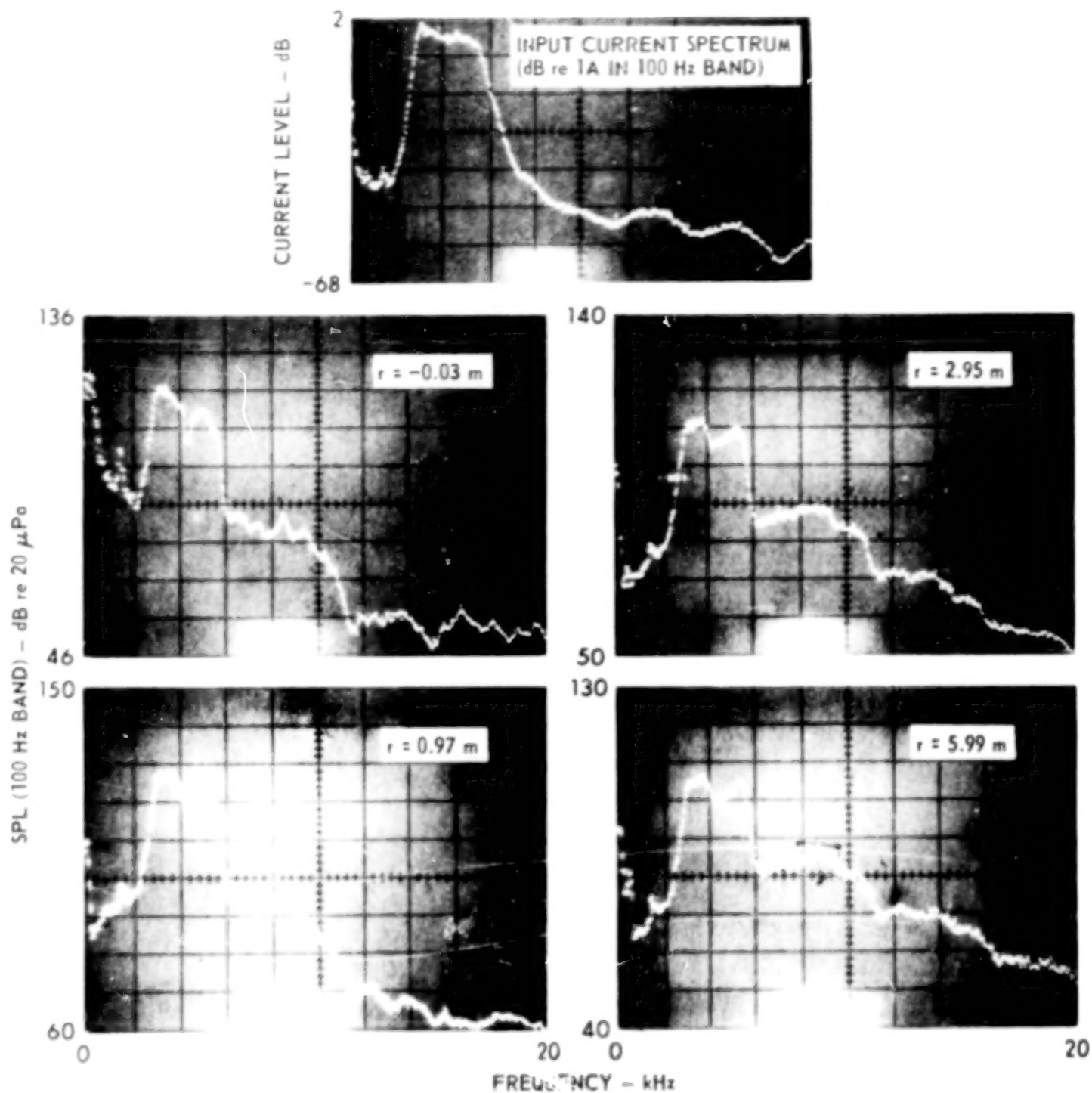
FIGURE 5-13a

NOISE SPECTRUM AS A FUNCTION OF RANGE r (EXPERIMENT AEM9)

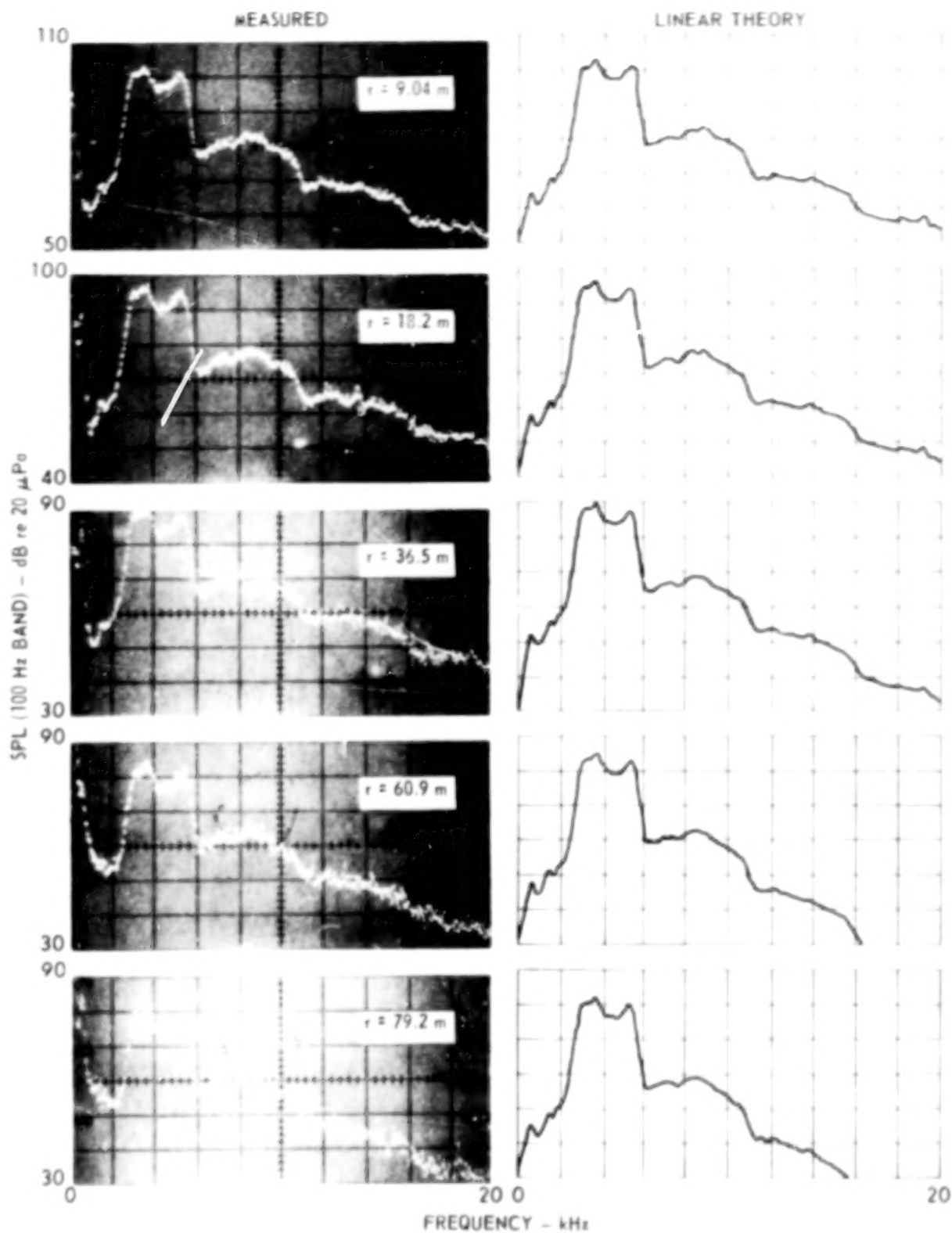R_0 (10 kHz) = 7.6 m, OASPL = 133 dB re 20 μ Pa at 1 m

78

FIGURE 5-13b
NOISE SPECTRUM AS A FUNCTION OF RANGE r (EXPERIMENT AEM9)
$R_0(10 \text{ kHz}) = 7.6 \text{ m}$; OASPL $= 133$ dB re 20 μPa at 1 m

79

DISCUSSION AND ANALYSIS OF EXPERIMENTAL RESULTS

The experimental results are discussed and interpreted in this chapter, and some attempt is made to provide theoretical explanations for the observations. The discussion in Section A is general and covers both near-field and farfield. In Section B the nonlinear theory (for the farfield) described in Chapter 3 is tested by comparing predictions with measurements from Chapter 5.

A. DISCUSSION OF EXPERIMENTAL RESULTS

1. Nearfield Measurements

Four observations may be made regarding the nearfield measurements. First, a tremendous growth of the high frequency end of the noise spectrum occurred in the array nearfield. See, for example, Fig. 5-12. Second, calculations showed that the growth of the high frequency end of the spectrum far exceeded that expected on the basis of linear diffraction theory. See Figs. 5-3 and 5-12. Third, on the other hand, the most intense portion of the spectrum was well described by the linear diffraction theory calculation. This observation is not inconsistent with the previous two. Only a small decrease, e.g., a small fraction of a decibel, in the intense portion of the spectrum is required to produce significant high frequency growth. Fourth, the high level data showed much more high frequency growth than did the low level data (see, for example, Fig. 5-2). On the basis of these observations, we conclude that the high frequency growth is a result of nonlinear propagation distortion. The fact that the

spectrum becomes so broad so rapidly is not surprising. Although the pro-
pagation distance is short, typically 9 m or less, the amplitude remains
high while the wave is in the nearfield.

    2.   Farfield Measurements

    The nonlinear effects noticed in the farfield measurements were
similar to those observed for the nearfield data. In all cases high
frequency growth was evident; in some cases it was strong. Linear
theory worked well for the intense, middle portion of the spectrum.
A very limited amount of low frequency growth took place. The distortion
that occurred was therefore of the Stage I type. The noise in our
experiments was not intense enough to produce Stage II distortion.

    As noted in Chapter 1, it is commonly believed that while nonlinear
effects may be important close to a jet engine, where the noise is very
intense, at some large distance they become unimportant because the SPL
has reached the "small-signal range." Linear theory may be relied on
thereafter. This premise is now tested, insofar as it can be tested
by our experimental data. Consider, for example, Fig. 5-11, which shows
a discrepancy of about 15 dB between the 20 kHz levels measured and pre-
dicted at $r = 79.3$ m. The linear theory prediction is of course based on
using 9.14 m as the value for r_o, i.e., taking the spectrum at 9.14 m as the
starting spectrum. If r_o is doubled, that is, if the linear theory pre-
diction is begun with the spectrum at 18.3 m, one finds that the discrepancy
at $r = 79.3$ m is reduced only a little, to 12 dB. Even if r_o is doubled
again, which means starting the prediction with the 36.6 m spectrum, the
discrepancy at $r = 79.3$ m is still 9 dB. In other words, at no distance

within our experimental range did divergence from linear theory predictions cease. In Chapter 5, the data shown in Fig. 5-4 were also used to make this point.

Although our experimental evidence supports the notion about the high frequency noise that, in Pernet's words, "once nonlinear, always nonlinear,"[*] we have no measurement beyond approximately 80 m. It might be argued, therefore, that if we had made measurements at 200 m, or 500 m, or 1000 m, we would eventually have encountered small-signal behavior. There is, however, sound theoretical basis for expecting that small-signal behavior will never be established, no matter how great the distance from the source. The theoretical reasoning is similar to that in Chapter 2 except that here no specific frequency dependence for α is assumed. Consider sinusoidal spherical waves whose amplitude at the reference distance r_o is p_{10}. If the source level is not too high, the second harmonic pressure amplitude p_2 is accurately given by the perturbation solution[5,27]

$$p_2 = \left(\frac{p_{10}^2 \beta k r_o^2}{2 r_o \rho_o c_o^2} \right) e^{-\alpha_2 r + 2\alpha_1 r_o} \int_{r_o}^{r} \frac{e^{(\alpha_2 - 2\alpha_1)\lambda}}{\lambda} d\lambda , \quad (6-1)$$

where α_1 and α_2 are the small-signal attenuation coefficients at the fundamental and second harmonic frequencies, respectively. The asymptotic form of Eq. 6-1, valid for $(\alpha_2 - 2\alpha_1)r \gg 1$, is

$$p_2 = \frac{\beta k p_{10}^2}{2 \rho_o c_o^2 (\alpha_2 - 2\alpha_1)} \left(\frac{r_o}{r} \right)^2 e^{-2\alpha_1(r - r_o)} . \quad (6-2)$$

Equation 6-2 is remarkable in two respects. First, the spreading factor seems to be r^{-2}, not r^{-1}. Second, the apparent absorption coefficient is $2\alpha_1$, not α_2. Since generally $\alpha_2 > 2\alpha_1$ ($\alpha_2 = 4\alpha_1$ for a thermoviscous medium), the nonlinearly generated second harmonic eventually decays more slowly than

[*] D. F. Pernet, personal communication to D. T. Blackstock (1977).

82

would have been expected from linear theory. Moreover, no distance is ever reached at which the small-signal behavior $[p_2 \sim r^{-1}\exp(\alpha_2 r)]$ is established. The third harmonic is found to behave similarly. At great distance its amplitude varies as $r^{-3}\exp(-3\alpha_1 r)$, not as $r^{-1}\exp(-\alpha_3 r)$. (As noted in Chapter 2, these results are equivalent to $p_2 \sim p_1^2$ and $p_3 \sim p_1^3$, where p_1 is the local amplitude of the fundamental.) Because we have here considered sinusoidal signals, not noise, the analysis is only suggestive. At the same time there is no reason to expect the high frequency noise components to have markedly different properties.

B.   COMPARISON OF DATA WITH NONLINEAR THEORY

In this section we compare measured spectra with those computed using the nonlinear theory described in Chapter 3. In particular, comparison is made with the data from Experiment AEM3 (see Fig. 5-12). The time waveform shown in Fig. 6-1 was constructed from the 9.04 m spectrum by the method described in Chapter 3. The sampling interval Δf was 50 Hz so that the period of the constructed waveform, $1/\Delta f$, was 20 msec. The constructed waveform was then used as the source waveform in the computational procedure described in Chapter 3 A comparison of measured spectra with the computed ones is given in Fig. 6-2; measured spectra are on the left, computed ones on the right. The agreement between measured and computed spectra is good for the spectral peak. For the higher frequency regions, however, the agreement becomes progressively poorer with both increasing frequency and range. The poor agreement at the higher frequencies is typical of that found when other comparisons with data were made. In general, predictions based on the nonlinear model were at best only slightly better than those based on linear theory.
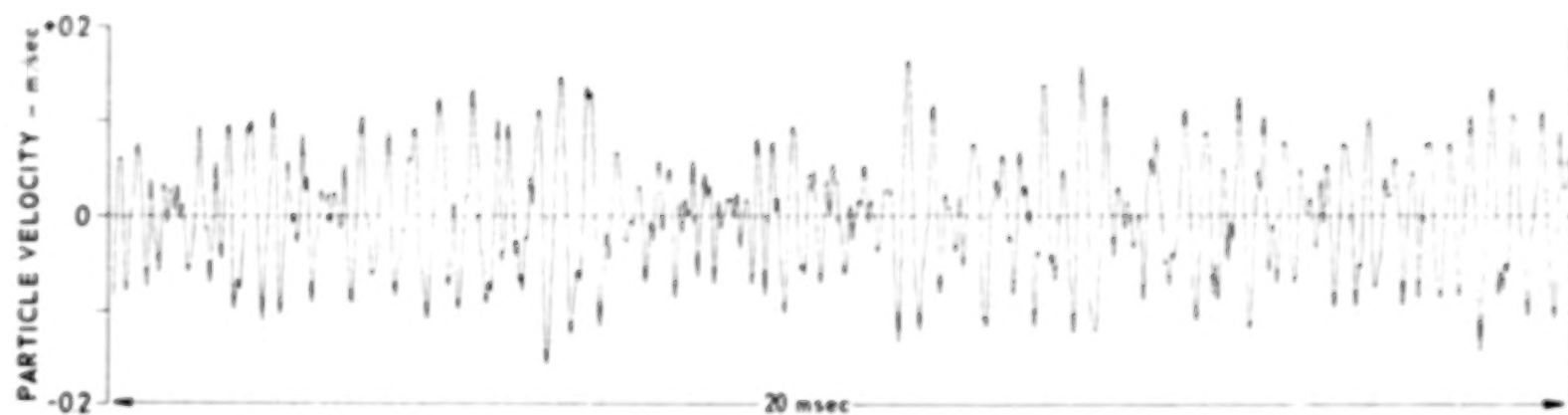
FIGURE 6-1
TIME WAVEFORM CONSTRUCTED FROM THE 9.04 m SPECTRUM
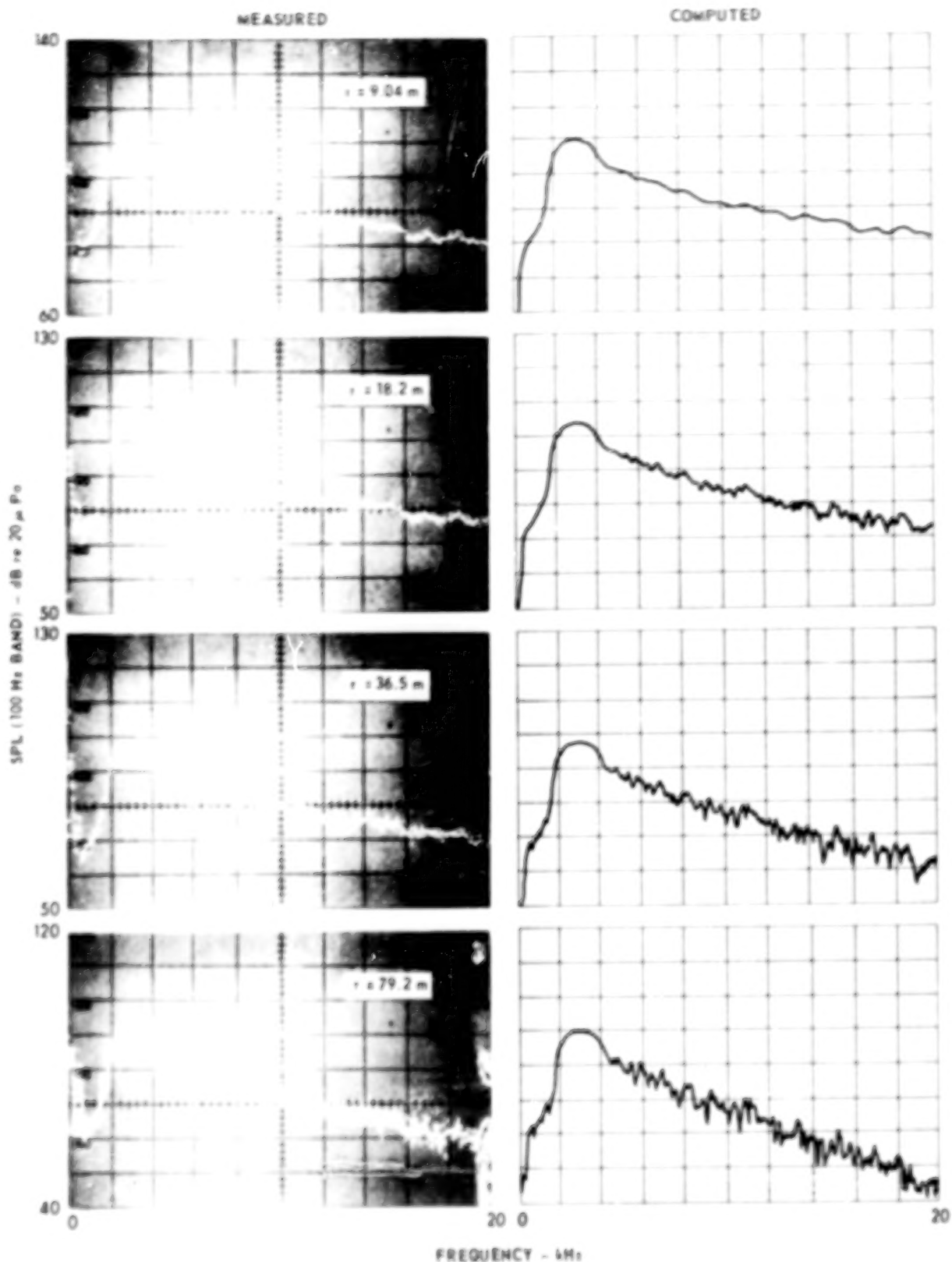**OF EXPERIMENT AEM3**

FIGURE 6-2
COMPARISON OF MEASURED AND COMPUTED NOISE SPECTRA (EXPERIMENT AEm3)
A NONLINEAR THEORY WAS USED TO OBTAIN THE COMPUTED SPECTRA (SEE TEXT)

TABLE OF CONTENTS

We feel that the failure of the predictions based on our model of nonlinear theory is not due to any error in nonlinear theory per se. After all, direct application of the theory gave predictions that were in excellent agreement with measurements in Phase I. It seems likely that our model failed because our method of constructing the source waveform was too simple. It will be recalled that the source spectrum, e.g., the 9.04 m spectrum shown in Fig. 6-2, was represented as a group of closely spaced line components, each having a random phase. No other property of the source noise was specified. Yet the source noise does have a special character by virtue of the distortion it has suffered in traveling through the horn and through the nearfield. In particular, the spectral region above the original noise band (the original band was 2-4 kHz for the noise shown in Fig. 6-2) is made up of distortion components (harmonics and intermodulation products) generated by nonlinear interactions in the original band. There is thus a closer connection between the high frequency components and the original band components than there would have been had the high frequency components been generated independently. One property that ought to be considered, for example, is the phase coherence between components in the original band and those at higher frequencies. By neglecting phase coherence when we constructed the source waveform, we eliminated the possibility that subsequently generated higher frequency components could add in phase to components already present. This would help explain why the predicted spectra fall below the measured spectra at high frequency (Fig. 6-2).

The simplest way to correct the error in our prediction model would be to use a direct recording of the noise signal at $r = r_o$ as the input waveform for the computer program.

86

Previous conclusions in this chapter regarding the role of nonlinear effects in our experiments are, of course, in no way affected by the success or failure of our nonlinear propagation model. The conclusions were established independent of such a model and hence stand alone.

CHAPTER 7

APPLICATION TO JET NOISE

The relevance of our results for actual jet aircraft noise is discussed
in this chapter. Because the noise in our experiments is approximately
one decade higher than typical jet noise, some scaling must be done before
comparisons can be made.

A. SCALING LAWS FOR NONLINEAR PROPAGATION DISTORTION

As was pointed out in Chapter 2, when ordinary absorption is not
important, the distortion of two different sinusoidal waves is the same
if the amplitude-frequency product is the same for each (see the dis-
cussion following Eq. 2-1). We now seek a generalization of this rule
for waves of arbitrary waveform.

The derivation given here is similar to that in Ref. 13. We start
with the Earnshaw solution, Eqs. 3-7. For convenience Eq. 3-7b is
repeated here

$$t' = \tau - \beta u(\tau) x/c_o^2 \quad . \tag{7-1}$$

It will be recalled that t' is the retarded arrival time of a wavelet
whose particle velocity is u. The parameter τ is the value of t' at $x=0$.
For simplicity of notation in what follows we use the unprimed symbol
t in place of t'. In Fig. 7-1 the distortion of a wave is traced. Two
particular wavelets are identified by their particle velocities u_1 and
u_2 and their values of τ (t_{10} and t_{20}, respectively). Application of
Eq. 7-1 to these two wavelets gives

$$t_1 = t_{10} - \beta u_1 x/c_o^2$$

and

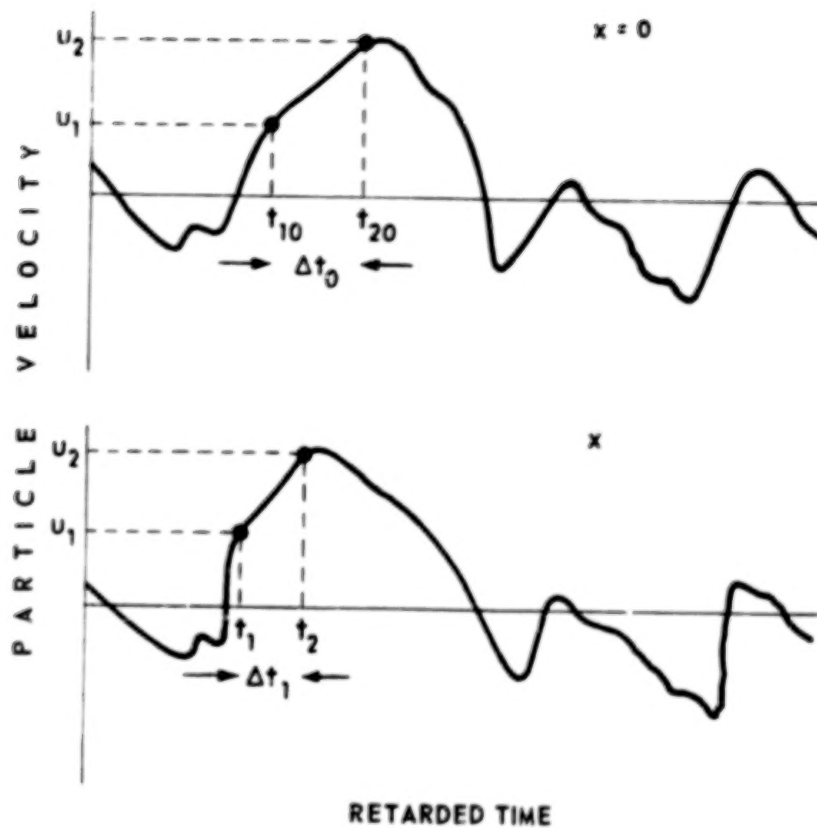$$t_2 = t_{20} - \beta u_2 x/c_o^2 \quad . \tag{7-2}$$

88

FIGURE 7-1
PROGRESSIVE DISTORTION OF AN ARBITRARY WAVEFORM

The time separation of the two wavelets $\Delta t = t_2 - t_1$ is therefore

$$\Delta t = \Delta t_0 - \beta \Delta ux/c_0^2 \quad , \tag{7-3}$$

where $\Delta t_0 = t_{20} - t_{10}$ is the original separation and $\Delta u = u_2 - u_1$. The fractional change in separation of the two wavelets $\delta = (\Delta t_0 - \Delta t)/\Delta t_0$ is

$$\delta = \beta \Delta ux/c_0^2 \Delta t_0 \quad . \tag{7-4}$$

The value of δ tells us how close one wavelet has come to the other and is therefore a measure of the distortion of the wave. For instance, $\delta = 1$ implies the second wavelet has caught up to the first one. It will be seen that δ can be doubled by doubling the amplitude of the wave (because u is then doubled) or by time compressing the wave by a factor of two (because Δt_0 is then halved). Time compressing by a factor of two means doubling the frequency of every component in the spectrum. Alternatively, if the amplitude is doubled and the frequency halved, the degree of distortion will remain the same. Thus for random signals as well as for periodic ones, it is the product of amplitude and frequency that determines the degree of distortion. For spherical waves the expression for δ may be found by replacing x in Eq. 7-4 by $r_0 \ln(r/r_0)$. The frequency-amplitude scaling is not, however, affected by this change.

B. COMPARISON OF MEASUREMENTS WITH JET DATA

Spectra from two of our propagation experiments, JBL9 and AEM3, are compared with spectra of KC-135A aircraft (ground runup, single engine, measurement angle 30° off the jet axis) in Fig. 7-2.* The distance for the comparison was 250 ft, or 76.2 m (the data had to be extrapolated backward about 3 m, a correction of 0.3 dB, in order to make the comparison). The spectral

---

*The KC-135A data was kindly furnished by John N. Cole, Aerospace Medical Research Laboratory, W-PAFB, Ohio.

FIGURE 7-2
COMPARISON OF ACTUAL JET NOISE SPECTRA WITH SCALED SPECTRA
(SCALED DOWN BY A FACTOR OF 10 IN FREQUENCY, SCALED UP 20 dB
IN LEVEL) FROM EXPERIMENTS AEM3 AND JBL9

RANGE = 76.2 m

peaks for our data were approximately a decade above those frr the KC-135A.
For ease of comparison, therefore, we have scaled our spectra down in
frequency by a factor of 10 and up in spectrum level by 20 dB in accordance
with the scaling law given in Section A. If it is assumed that the two
noises had similar statistical properties at their respective sources,
for example, if both were Gaussian, then it is reasonable to compare them
for their susceptibility to nonlinear propagation distortion.
It will be seen that the level of KC-135A noise is roughly 10 dB higher
in the mid- and high-frequency regions than our noise. By demonstration,
our noise was definitely affected by nonlinearity. The implication is
that even stronger nonlinear effects were at work during the propagation
of the KC-135A noise. Moreover, although the KC-135A is a very noisy
aircraft, many other current aircraft produce noise whose spectrum levels
are higher than our scaled spectra. One therefore concludes that nonlinear
effects are probably common in jet noise.

CHAPTER 8

SUMMARY

A series of experiments has been carried out on the propagation of finite-amplitude noise outdoors. The purpose of the study was to determine the extent to which nonlinear effects influence the propagation of noise from a controlled source in the outdoor environment. A secondary purpose was to develop, if possible, a theoretical model for the noise propagation. A ground-mounted electroacoustic source transmitted broadband, octave band, or 1/3 octave band noise in the frequency range 2-10 kHz. The source level (overall sound pressure level) of the noise was in the range 121-145 dB re 20 µPa at 1 m. The propagation path was vertical and parallel to an 85 m tower, whose elevator carried the traveling microphone. The maximum propagation distance was about 80 m. The experiments were done at night during the months June through September 1977. The meteorological conditions (ground level) were as follows: temperature range 23-31°C, relative humidity range 55-90%, and wind speed range 0-24 km/h.

The measurements were compared with theoretical predictions based on linear theory. Spherical spreading, atmospheric attenuation, and, as appropriate, source diffraction were accounted for in these predictions. Predictions based on nonlinear theory were also attempted, but the particular model was based on an assumption about the noise distortion in the transmitter nearfield. As it turned out, this assumption was not justified in our experiments.

Use of an amplitude-frequency scaling law made it possible to compare the noise from our experiments with noise from a KC-135A aircraft. The importance of nonlinear effects in actual jet noise could thus be estimated.

The primary conclusions are these.

1. A strong generation of high frequency noise caused by nonlinear effects was found in all the high intensity noise experiments. A very limited amount of low frequency noise was also generated. The intense, middle part of the spectrum deviated little if any from expectations based on linear theory. These observations indicate that although shocks formed in the noise waveform, distortion did not reach the stage at which shock merging was important.

2. The spectral distortion occurred in both the transmitter nearfield and farfield. Moreover, the distortion in the nearfield was over and above the spectral changes associated with diffraction.

3. At no measurement point was small-signal behavior established for the high frequency noise. Theoretical calculations for tone signals support the proposition that the nonlinearly generated high frequency noise never achieves a farfield where small-signal behavior is established.

4. Comparison of the measured spectra with predictions from a model based on nonlinear theory showed poor agreement for the high frequency noise. The failure of our predictions was not due to an error in the nonlinear theory per se, but rather due to an inadequate description of the source noise waveform. In the future, use of a directly recorded input waveform should be tried.

5. Comparison of our scaled experimental measurements with actual jet spectra show that the spectrum levels encountered in our experiments are well within the jet noise range. Indeed, the noise

measured from a KC-135A jet is roughly 10 dB higher in spectrum level than our scaled noise. One therefore concludes that nonlinear effects are probably common in jet noise.

The report also contains some information about outdoor propagation of finite-amplitude tones. Tone experiments done as a forerunner to those on noise are reviewed. Additional data on tones taken during the course of the noise study are also described. Theoretical analyses of propagation of very weak and very strong tones are presented.

APPENDIX A

THEORETICAL RESULTS FOR FINITE-AMPLITUDE

SPHERICAL WAVES[2]

I.   WEAK WAVES - A PERTURBATION SOLUTION OF BURGERS' EQUATION

Our purpose here is to obtain a theoretical prediction valid for weak spherical waves in a thermoviscous fluid. Several other researchers have obtained results valid for the weak-wave problem.[5, 27-29] Pernet and Payne,[5] for example, extended the phenomenological approach Thuras et al [30] had used for plane waves. Blackstock and Willette[29] started with the Burgers' equation for spherical waves and obtained a perturbation solution valid to third order in the source Mach number ϵ. The work we present here is an extension of the perturbation solution to fifth order in ϵ.

The Burgers' equation for spherical waves is (see, for example, Ref. 31)

$$\frac{1}{r}\frac{\partial(rp)}{\partial r} - \frac{\alpha}{\omega^2}\frac{\partial^2 p}{\partial t'^2} = \frac{\beta}{\rho_o c_o^3}p\frac{\partial p}{\partial t'} \quad , \tag{A-1}$$

where α is the thermoviscous absorption coefficient at angular frequency ω and $t'=t-(r-r_o)/c_o$ is the retarded time. Let the boundary condition be

$$p(r_o,t) = p_{10}\sin \omega t \quad . \tag{A-2}$$

If the dimensionless quantities $V=(r/r_o)(p/\rho_o c_o^2)$, $y=\omega t'$, and $\zeta=\beta k r_o$ are introduced, Eqs. A-1 and A-2 become

$$\frac{\partial V}{\partial r} - \alpha\frac{\partial^2 V}{\partial y^2} = \frac{\zeta}{r} V\frac{\partial V}{\partial y} \quad , \tag{A-3}$$

and

$$V(r_o,y) = \epsilon \sin y \quad , \tag{A-4}$$

respectively. We seek a solution of Eq. A-3 in the form of a perturbation

96

series. That is, we suppose a solution of the form

$$V = \sum_{n=1}^{\infty} \epsilon^n v^{(n)} \tag{A-5}$$

exists. Substituting Eq. A-5 into Eq. A-3, we obtain

$$\sum_{n=1}^{\infty} \epsilon^n \left[\frac{\partial v^{(n)}}{\partial r} - \alpha \frac{\partial^2 v^{(n)}}{\partial y^2} - \frac{\zeta}{r} \sum_{i+j=n} v^{(i)} \frac{\partial v^{(j)}}{\partial y} \right] = 0 \qquad . \tag{A-6}$$

In order that Eq. A-6 be satisfied for arbitrary values of ϵ, the bracketed term must vanish for each value of n. The result is the following infinite set of linear, inhomogeneous differential equations:

$$\frac{\partial v^{(n)}}{\partial r} - \alpha \frac{\partial^2 v^{(n)}}{\partial y^2} = \frac{\zeta}{r} \sum_{i+j=n} v^{(i)} \frac{\partial v^{(j)}}{\partial y} \qquad . \tag{A-7}$$

The equations must be solved in sequence. For example, the source (inhomogeneous) terms for the second order solution $v^{(2)}$ depend on $v^{(1)}$. The source terms for the third order solution $v^{(3)}$ depend on $v^{(2)}$ and $v^{(1)}$. We now proceed to solve the first five equations.

The first order equation is

$$\frac{\partial v^{(1)}}{\partial r} - \alpha \frac{\partial^2 v^{(1)}}{\partial y^2} = 0 \qquad . \tag{A-8}$$

The solution satisfying the boundary condition Eq. A-4 is

$$v^{(1)} = e^{-\alpha(r-r_0)} \sin y \qquad . \tag{A-8a}$$

This is the familiar solution of linear acoustics. The second order equation is

$$\frac{\partial v^{(2)}}{\partial r} - \alpha \frac{\partial^2 v^{(2)}}{\partial y^2} = \frac{\zeta}{r} v^{(1)} \frac{\partial v^{(1)}}{\partial y}$$

$$= \frac{\zeta}{2r} e^{-2\alpha(r-r_0)} \sin 2y \qquad , \tag{A-9}$$

whose solution is

$$v^{(2)} = \frac{\zeta}{2} e^{-4\alpha(r-r_0)} I_{22} \sin 2y \quad , \tag{A-9a}$$

where

$$I_{22} = \int_{r_0}^{r} \frac{e^{2\alpha(r'-r_0)}}{r'} dr' \quad .$$

We shall have occasion to write down several integrals of the form $\int F(r) r^{-1} \exp(\alpha r) dr$ and adopt the following convention. The integral I_{mn} is associated with the contribution of the mth order solution to the nth harmonic.

The third order equation is

$$\frac{\partial v^{(3)}}{\partial r} - \alpha \frac{\partial^2 v^{(3)}}{\partial y^2} = \frac{\zeta}{r} \left[\frac{\partial(v^{(1)} v^{(2)})}{\partial y} \right],$$

$$= \frac{\zeta^2}{4r} I_{22} e^{-5\alpha(r-r_0)} [3 \sin 3y - \sin y] \quad . \tag{A-10}$$

Its solution is

$$v^{(3)} = -\frac{\zeta^2}{4} I_{31} e^{-\alpha(r-r_0)} \sin y + \frac{3\zeta^2}{4} I_{33} e^{-9\alpha(r-r_0)} \sin 3y \quad , \tag{A-10a}$$

where

$$I_{31} = \int_{r_0}^{r} \frac{I_{22}(r') e^{-4\alpha(r'-r_0)}}{r'} dr' \quad ,$$

and

$$I_{33} = \int_{r_0}^{r} \frac{I_{22}(r') e^{4\alpha(r'-r_0)}}{r'} dr' \quad .$$

We see that the third order solution contains not only a third harmonic term but also one that represents a correction to the amplitude of the fundamental. This correction denotes loss caused by nonlinear effects.

The fourth order equations and solution are listed below.

$$\frac{\partial v^{(4)}}{\partial r} - \alpha \frac{\partial^2 v^{(4)}}{\partial y^2} = \frac{\zeta}{r}\left[v^{(2)} \frac{\partial v^{(2)}}{\partial y} + \frac{\partial(v^{(1)}v^{(3)})}{\partial y}\right]$$

$$= \frac{\zeta^3}{4r}\left[\left(-I_{31}\, e^{-2\alpha(r-r_0)} - 3I_{33}\, e^{-10\alpha(r-r_0)}\right)\sin 2y\right.$$

$$\left. + \left(I_{22}^2\, e^{-8\alpha(r-r_0)} + 6I_{33}\, e^{-10\alpha(r-r_0)}\right)\sin 4y\right]. \qquad \text{(A-11)}$$

$$v^{(4)} = \frac{\zeta^3}{4}\left[- (I_{42}+3I'_{42})\, e^{-4\alpha(r-r_0)}\sin 2y\right.$$

$$\left. + (I_{44}+ 6I'_{44})\, e^{-16\alpha(r-r_0)}\sin 4y\right]. \qquad \text{(A-11a)}$$

$$I_{42} = \int_{r_0}^{r} \frac{I_{31}(r')\, e^{2\alpha(r'-r_0)}}{r'}\, dr' \quad .$$

$$I'_{42} = \int_{r_0}^{r} \frac{I_{33}(r')\, e^{-6\alpha(r'-r_0)}}{r'}\, dr' \quad .$$

$$I_{44} = \int_{r_0}^{r} \frac{I_{22}^2(r')\, e^{8\alpha(r'-r_0)}}{r'}\, dr' \quad .$$

$$I'_{44} = \int_{r_0}^{r} \frac{I_{33}(r')\, e^{6\alpha(r'-r_0)}}{r'}\, dr' \quad .$$

Because of the rather formidable algebra involved, the only part of the fifth order solution that was calculated was the contribution to the fundamental. This contribution is denoted $v^{(5)}_{\text{fund}}$. The results are

listed below.

$$\frac{\partial v^{(5)}}{\partial r} - \alpha \frac{\partial^2 v^{(5)}}{\partial y^2} = \frac{\zeta}{r} \left[\frac{\partial \left(v^{(1)} v^{(4)} \right)}{\partial y} + \frac{\partial \left(v^{(2)} v^{(3)} \right)}{\partial y} \right] \qquad . \qquad \text{(A-12)}$$

$$v^{(5)}_{\text{fund.}} = \frac{\zeta^4}{8} e^{-\alpha(r-r_o)} \left[I_{51} - \frac{3}{2} I'_{51} \right] \qquad . \qquad \text{(A-12a)}$$

$$I_{51} = \int_{r_o}^{r} \left[I_{42}(r') + 3 I'_{42}(r') + \frac{I_{22}(r') \, I_{31}(r')}{2} \right] \frac{e^{-4\alpha(r'-r_o)}}{r'} \, dr' \quad .$$

$$I'_{51} = \int_{r_o}^{r} \frac{I_{22}(r') \, I_{33}(r') \, e^{-12\alpha(r'-r_o)}}{r'} \, dr' \qquad .$$

As may be seen from the higher order results, the solutions are easy to write down in terms of the integrals I_{mn}. It is the calculation of these integrals which is indeed a arduous task.

Let us now put our results in terms of the normalized harmonic amplitudes $B_n = (r/r_o)(p_n/p_{10})$. Defining $\sigma_o = \epsilon \zeta$, we obtain

$$B_1 = e^{-\alpha(r-r_o)} \left[1 - \frac{\sigma_o^2}{4} I_{31} + \frac{\sigma_o^4}{8} \left(I_{51} - \frac{3}{2} I'_{51} \right) \right] \qquad , \qquad \text{(A-13)}$$

$$B_2 = e^{-4\alpha(r-r_o)} \left[\frac{\sigma_o}{2} I_{22} - \frac{\sigma_o^3}{4} \left(I_{42} + 3 I'_{42} \right) \right] \qquad , \qquad \text{(A-14)}$$

$$B_3 = e^{-9\alpha(r-r_o)} \left[\frac{3\sigma_o^2}{4} I_{33} \right] \qquad . \qquad \text{(A-15)}$$

100

and

$$B_4 = e^{-16\alpha(r-r_o)} \left[\frac{\sigma_o^3}{4} (I_{44} + 6I'_{44}) \right] \quad . \qquad (A-16)$$

We note here that in the limit as $\alpha r \to 0$, the expressions for the B_n given in Eqs. A-13 to A-16 reduce to the corresponding expressions found using lossless theory directly. The details are given in Ref. 2.

In many cases where a perturbation solution is useful, some distortion is evident in the source waveform $V(r_o, y)$. Commonly this distortion is primarily second harmonic (especially if it is due to nonlinear propagation distortion in the nearfield). We shall now determine how the presence of an "initial" second harmonic signal changes the lower order perturbation results. Suppose that, in place of Eq. A-4, the boundary condition is

$$V(r_o, y) = \epsilon \left[\sin y + a \sin(2y + \phi) \right] \quad , \qquad (A-17)$$

where a and ϕ are the relative amplitude and phase of the second harmonic, respectively. The first order perturbation solution satisfying this boundary condition is

$$V^{(1)} = e^{-\alpha(r-r_o)} \sin y + a \, e^{-4\alpha(r-r_o)} \sin(2y + \phi) \quad . \qquad (A-18)$$

The second order equation, Eq. A-9, has a source term proportional to $V^{(1)}(\partial V^{(1)}/\partial y)$. Hence, it is easily seen that $V^{(2)}$ contains contributions to the first, second, third, and fourth harmonics. The expression for $V^{(2)}$ is

$$V^{(2)} = -\frac{a\zeta}{2} e^{-\alpha(r-r_o)} I_{21} \sin(y + \phi) + \frac{\zeta}{2} e^{-4\alpha(r-r_o)} I_{22} \sin 2y$$

$$\qquad\qquad (A-19)$$

$$+ F(r) \sin(3y + \phi) + G(r) \sin(4y + 2\phi) \quad ,$$

where

$$I_{21} = \int_{r_o}^{r} \frac{e^{-4\alpha(r'-r_o)}}{r'} \, dr' \, .$$

We note here that the second harmonic component of $V^{(2)}$ is not affected by the "initial" second harmonic. To second order, therefore, the expressions for p_1 and p_2 are

$$p_1 = p_{10} e^{-\alpha(r-r_o)} \left(1 + \left(\frac{a\sigma_o}{2}\right)^2 I_{21}^2 - a\sigma_o \, I_{21} \cos \varphi \right)^{1/2} \, , \quad (A-20)$$

and

$$p_2 = p_{10} e^{-4\alpha(r-r_o)} \left(a^2 + \frac{\sigma_o^2}{4} I_{22}^2 + a\sigma_o I_{22} \cos \varphi \right)^{1/2} \, . \quad (A-21)$$

A comparison of Eqs. A-20 and A-21 with experimental data is given in Chapter 2. Further comparison of Eq. A-21 with measured data is given in Appendix D.

The asymptotic values $(\alpha r \to \infty)$ of the harmonic amplitudes p_n are particularly interesting. From Eqs. A-13 to A-16, the asymptotic values for the first four harmonics are

$$(p_1)_{asm} = p_{10} \left(\frac{r_o}{r}\right) e^{-\alpha(r - r_o)} \, , \quad (A-22a)$$

$$(p_2)_{asm} = p_{10} \left(\frac{r_o}{r}\right)^2 \left(\frac{\Gamma}{4}\right) e^{-2\alpha(r - r_o)} \, , \quad (A-22b)$$

$$(p_3)_{asm} = p_{10} \left(\frac{r_o}{r}\right)^3 \left(\frac{\Gamma}{4}\right)^2 e^{-3\alpha(r - r_o)} \, , \quad (A-22c)$$

and

$$(p_4)_{asm} = p_{10} \left(\frac{r_o}{r}\right)^4 \left(\frac{\Gamma}{4}\right)^3 e^{-4\alpha(r - r_o)} \, . \quad (A-22d)$$

As in the plane wave case (see Chapter 1) the apparent absorption coefficient is $n\alpha$, not $n^2\alpha$. In addition the apparent geometrical spreading is as r^{-n}, not r^{-1}. The harmonic decay rates given in Eqs. A-22 are, however, slower than those predicted using linear theory. That is, for $n>1$, $r^{-n}\exp(-n\alpha r)$

ultimately represents a slower rate of decay than $r^{-1}\exp(-n^2\alpha r)$. In other words, the higher harmonic sound never establishes a farfield where traditional small-signal laws take over.

In conclusion, we have presented a fifth order perturbation solution of Burgers' equation. Although the integrals involved become increasingly complicated for the higher order results, the low order results should be useful for a great many weak-wave problems.

II. STRONG WAVES - SOLUTION OF THE AMPLITUDE DECAY RATE EQUATION

Rudnick[33] originally proposed a model for the decay of the peak amplitude of a plane, sawtooth wave. The total decay rate for the peak amplitude was taken to be the decay rate due to ordinary absorption plus the decay rate due to nonlinear effects. We call this an "amplitude decay model" to distinguish it from various intensity decay models (see, for example, Ref. 21). Blackstock developed analogous equations for the fundamental pressure amplitude for both plane and spherical waves.[*]
It was assumed that the decay rate dp_1/dr of the fundamental pressure amplitude p_1 is the sum of the decay rate due to absorption $(dp_1/dr)_{abs.} = -\alpha p_1$ and the decay rate $(dp_1/dr)_{f.a.}$ of a spherically spreading sound wave of finite amplitude. The latter decay rate may be found as follows. If the boundary condition is given by Eq. A-2, the value of p_1 in the sawtooth region $(\sigma \geq 3)$ in the absence of absorption is (from the weak-shock solution[32])

$$p_1 = \frac{r_c}{r}\frac{2p_{10}}{1 + \sigma} \qquad . \tag{A-23}$$

From this equation we obtain

[*] D. T. Blackstock, unpublished research (1971).

103

$$\left(\frac{dp_1}{dr}\right)_{f.a.} = \frac{r_o}{r^2} \frac{2p_{10}}{1+\sigma} - \frac{\beta\epsilon k r_o^2}{r^2} \frac{2p_{10}}{(1+\sigma)^2}$$

(A-24)

$$= -\frac{1}{r} p_1 - \frac{\beta\epsilon k}{2p_{10}} p_1^2 \quad.$$

By supposition the total decay rate dp_1/dr is then

$$\left(\frac{dp_1}{dr}\right) = \left(\frac{dp_1}{dr}\right)_{abs.} + \left(\frac{dp_1}{dr}\right)_{f.a.}$$

(A-25)

$$= -\alpha p_1 - \frac{1}{r} p_1 - \frac{\beta\epsilon k}{2p_{10}} p_1^2 \quad.$$

We now wish to solve Eq. A-25 subject to the condition that the solution reduce to the weak-shock solution (Eq. A-23) as $\alpha \to 0$. The form of the solution for the plane wave case suggests that we try a solution of the form

$$p_1 = \frac{r_o}{r} \frac{A \, e^{-\alpha(r-r_o)}}{1 + f(r)} \quad,$$

(A-26)

where A is a constant and the function $f(r)$ is to be determined. Substitution of Eq. A-26 into Eq. A-25 leads to the following form of $f(r)$:

$$f(r) = \frac{A \, \beta\epsilon k r_o}{2p_{10}} e^{\alpha r_o} \int_{\alpha r_o}^{\alpha r} \frac{e^{-\lambda}}{\lambda} d\lambda \quad.$$

(A-27)

The choice $A = 2p_{10}$ yields the weak-shock solution, Eq. A-23, as $\alpha \to 0$.
If the definition of the exponential integral $E_1(a)$ (see, for example, Ref. 34),

$$E_1(a) = \int_a^\infty \frac{e^{-\lambda}}{\lambda} d\lambda \quad,$$

is used, the expression for p_1 becomes

$$p_1 = \frac{r_o}{r} \cdot \frac{2p_{10}\, e^{-\alpha(r-r_o)}}{1 + \beta\epsilon kr_o\, e^{\alpha r_o}[E_1(\alpha r_o)-E_1(\alpha r)]} \qquad . \qquad\text{(A-28)}$$

Equation A-28 is simple to evaluate in practice. The exponential integral $E_1(\alpha r)$ may be read from tables or evaluated by certain series representations. See, for example, Ref. 34, which gives a six term approximation

$$E_1(\alpha r) = -\ln(\alpha r) + \sum_{i=0}^{5} a_i(\alpha r)^i \qquad , \qquad\text{(A-29)}$$

having a maximum percentage error of 9×10^{-5} for the range $0 \leq \alpha r \leq 1$.

Equation A-28 was tested by comparing it with freefield propagation data taken using a siren operating at 6.1 kHz in air (see Ref. 1 or Chapter 2 for a description of the siren). Because of the relatively high acoustic power output of the siren (approximately 600 W of acoustic power with a 40° beamwidth between the 3 dB down points), the characteristic sawtooth waveshape was already in evidence at a propagation distance of approximately 2 m. Our measured boundary condition was therefore a sawtooth wave at a given distance r_m from the source. To use Eq. A-28 we must compute from our measured data the amplitude p_{10} and effective source radius r_o of a sinusoid which would yield the measured sawtooth wave at range r_m. The weak-shock solution may be used for this purpose provided $\alpha r \ll 1$. The smallest value of r for which Eq. A-23 is valid is the one for which $\sigma=3$. Let p_{1m} be the measured value of the fundamental amplitude at range r_m. Combining Eqs. A-23 and 2-1 (with $\sigma=3$, $r=r_m$, and

105

$p_1 = p_{1m}$), we obtain

$$r_o = r_m \exp(-3/2 \beta \varepsilon_m k r_m)$$ (A-30)

and

$$p_{10} = 2 p_{1m} r_m / r_o \quad ,$$ (A-31)

where $\varepsilon_m = p_{1m} / \rho_o c_o^2$.

Figure A-1 shows the results of a comparison of Eq. A-28 with the measured data. The absorption coefficient α was measured by means of a small-signal experiment done under similar conditions and found to be 0.0059 Np/m, a value consistent with the value computed according to Ref. 22. The values of p_{1m} and r_m were 2.29×10^3 μbar and 2.19 m, respectively. The values of p_{10} and r_o computed from Eqs. A-30 and A-31 were, respectively, 1.1×10^5 μbar and 0.09 m. The solid curve is the linear theory prediciton; the dashed curve represents the solution of the amplitude decay equation. The latter is seen to provide a good fit to the data.

In summary the model proposed here, although ad hoc, does seem to provide a good description of the experimental data. Further experimental verification of this model may be found in Ref. 1 or Chapter 2. The model should be useful in spherical wave problems whenever the source is strong enough to produce a sawtooth wave.
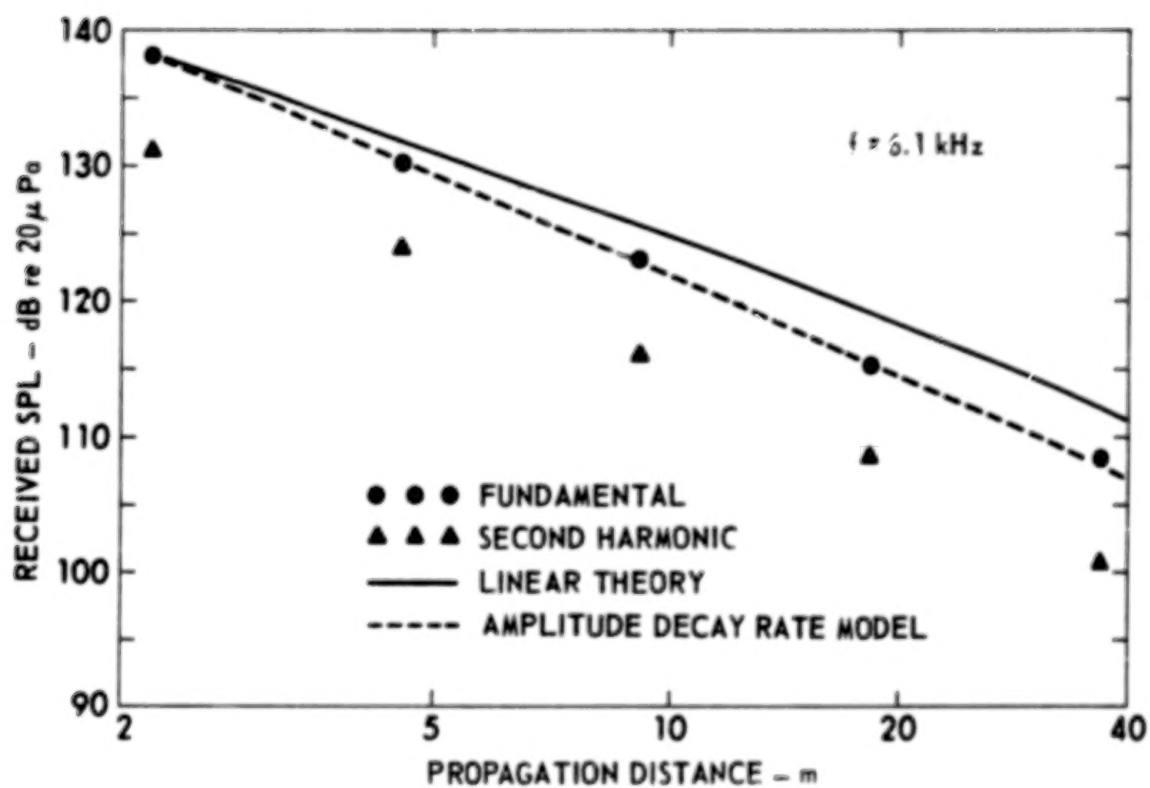
FIGURE A-1
COMPARISON OF THE AMPLITUDE DECAY
RATE MODEL WITH PROPAGATION DATA

AMPLITUDE DENSITY OF A FINITE-AMPLITUDE WAVE*

Theoretical results are given here for the amplitude density of a wave subject to nonlinear propagation distoriton. Rudenko and Chirkin found an expression for the amplitude distribution of an initially narrow-band Gaussian process.[11] They couch the problem in terms of a complete statistical description of the noise. We give results here valid for an arbitrary waveform prior to shock formation.

Figure B-1 shows the waveform of an arbitrary signal at $x=0$. The probability $P(u, u + \Delta u)$ of observing wavelets having particle velocity amplitudes between u and $u + \Delta u$ is

$$P(u, u + \Delta u) = \sum_{i=1}^{N} \Delta t_i / T \quad , \tag{B-1}$$

where T is the sample length, N is the number of intervals Δt_i, and the $\{\Delta t_i\}$ are as shown in Fig. B-1. The probability density $p(u)$ is defined by

$$p(u) = \lim_{\Delta u \to 0} \frac{P(u, u + \Delta u)}{\Delta u} \tag{B-2}$$

Substitution of Eq. B-2 into Eq. B-2 leads to the expression

$$p(u, 0) = \frac{1}{T(0)} \sum_{i=1}^{N} \pm \frac{(-1)^{i+1}}{(\partial u / \partial t)_i} \quad , \tag{B-3}$$

where the zero in the argument denotes $x=0$. The factor $(-1)^{i+1}$ is necessary to convert the slopes $(\partial u / \partial t)_i$, which are alternately positive and negative, into all positive numbers (all the Δt_i in Eq. B-1 are positive).

*The text of this appendix has been submitted to the Journal of the Acoustical Society of America for publication as a Letter.
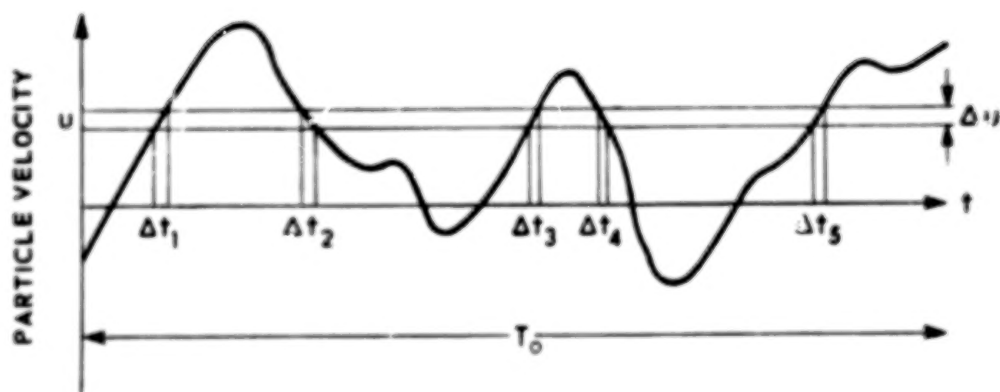
FIGURE B-1
DETERMINATION OF THE AMPLITUDE DENSITY
FOR THE INITIAL WAVEFORM

The + sign is to be used if the first term is positive, the - sign if the first term is negative. Equation B-3 shows that the initial amplitude density is determined by the collection of slopes $(\partial u/\partial t)_i$ of wavelets whose amplitude is u. Special note must be taken of what is meant by sample length. We take T to be the time interval between the two end wavelets in the sample, those at t=0 and t=T(0) in Fig. B-1. The disadvantage of this definition is that the time interval T may shorten or lengthen slightly with distance (as the two end wavelets migrate from their initial positions in the waveform). The advantage is that the particular wavelets included in the sample are always the same. If T were chosen to be a fixed time interval, some wavelets would in general be lost, or new wavelets would enter, at the ends.

Now let the signal travel to point x, distorting as it goes. The new density $p(u,x)$ is

$$p(u,\ x)\ =\ \frac{1}{T(x)}\ \sum_{i=1}^{N}\ \pm\ \frac{(-1)^{i+1}}{(\partial u/\partial t')_i}\ , \qquad (B-4)$$

where $T(x)$ is the new duration of the sample waveform, $t' = t - x/c_o$ is the retarded time, and c_o is the small-signal sound speed. Because of the distortion, the wavelets u are at new positions on the retarded time axis. Thus in general both the waveform slopes and the sample duration are different.

In order to determine the amplitude density of the distorted wave at point x, a description of the waveform there must be found. Given the initial waveform

$$u(0,t)\ =\ g(t)\ , \qquad (B-5)$$

the solution appropriate for plane progressive waves in a lossless fluid is[31]

$$u(x,t) = g(\tau) \quad , \tag{B-6a}$$

where

$$\tau = t' + \beta x u(\tau)/c_o^2 \quad , \tag{B-6b}$$

and β is the coefficient of nonlinearity. Applying Eqs. B-6 to the waveform of Fig. B-1, we see that the duration $T(x)$ of the distorted sample waveform is

$$T(x) = T_o - \delta T \quad , \tag{B-7a}$$

where T_o has been used as short for $T(0)$, δT is given by

$$\delta T = \beta x [u(T_o) - u(0)]/c_o^2 \quad , \tag{B-7b}$$

and $u(0)$ and $u(T_o)$ are the particle velocity values at the endpoints of the initial waveform. The waveform slopes at point x may also be determined from Eqs. B-6. One obtains

$$\frac{1}{\partial u/\partial t'} = \frac{1}{\partial u/\partial \tau} - \frac{\beta x}{c_o^2} \quad ,$$

or, because the slope in the τ system is the same as the initial slope (see Eqs. B-5 and B-6a)

$$\frac{1}{\partial u/\partial t'} = \frac{1}{\partial u(0,t)/\partial t} - \frac{\beta x}{c_o^2} \quad . \tag{B-8}$$

The expression for the density $p(u,x)$ may now be evaluated. Substitution of Eqs. B-7 and B-8 in Eq. B-4 leads to

$$p(u,x) = \frac{1}{T_o - \delta T} \sum_{i=1}^{N} \pm \frac{(-1)^{i+1}}{[\partial u(0,t)/\partial t]_i} \pm \frac{\beta x [(-1)^N - 1]}{2(T_o - T)c_o^2} \tag{B-9}$$

because the constant $-\beta x/c_o^2$ in Eq. B-8 cancels out for every pair of terms in the series. Only if N is odd is there an odd constant left

111

over, and its presence is accounted for by the final term on the right-hand side of Eq. B-9.

Comparing Eqs. B-3 and B-9, we see that

$$p(u, x) = \frac{p(u, 0)}{1 - \delta T/T_o} \pm \frac{\beta x[(-1)^N - 1]}{2(T_o - \delta T)c_o^2} \quad . \tag{B-10}$$

It may be seen that for a large class of cases $p(u,x)=p(u,0)$, that is, the amplitude density remains constant as the signal propagates. For example, if $u(0)=u(T_o)$, then δT vanishes and there is no leftover term (because the number N is even). Even if δT has a nonzero value, $p(u,x)$ may be made arbitrarily close to $p(u,0)$ by choosing T_o sufficiently large. In either case the amplitude density does not change with distance, so long as shocks do not form. For example, the sample noise waveforms considered in this report are periodic and continuous (see Chapter 3). The amplitude densities for these signals would not, therefore, be expected to change with distance.

A geometrical explanation of the constancy of the amplitude density may be found by examining Fig. B-2. The initial waveform is shown in Fig. B-2a. Figure B-2b shows the distorted waveform at point x. The size of Δu compared to u has been exaggerated for the sake of illustration. For a fixed value of u and Δu, the probability that the particle velocity lies between u and $u + \Delta u$ is proportional to the sum of the intervals Δt_i shown in Fig. B-2. As the wave distorts, the interval Δ_{10} is shortened by an amount porportional to Δu. The interval Δt_{20}, however, is lengthened by the same amount, so that $\Delta t_{10} + \Delta t_{20} = \Delta t_1 + \Delta t_2$. Thus the shortening of intervals on the left side of waveform peaks is compensated for by the lengthening of intervals or the right side of the peaks.
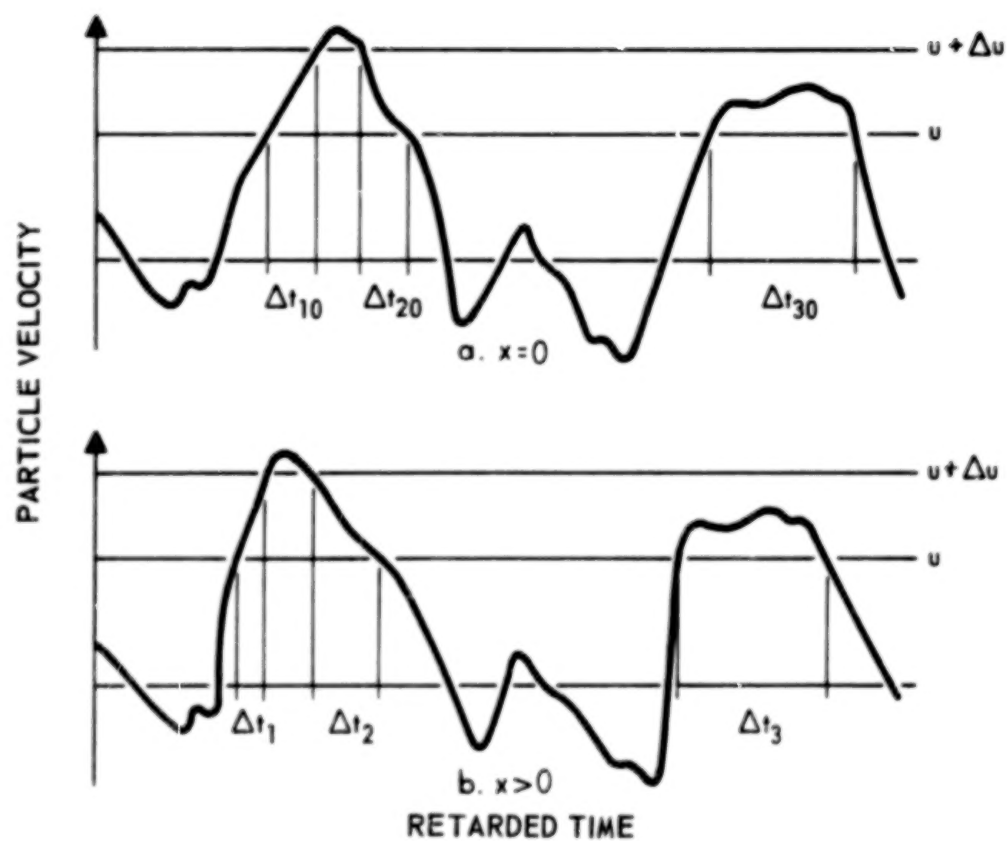
112

FIGURE B-2
EFFECT OF PROPAGATION DISTORTION
ON THE AMPLITUDE DENSITY

This illustration may be extended to show why $p(u,x)$ must change after shocks form. The limiting value of Δt_1 is zero, the value reached when wavelets in the window on the left-hand side of the peak form a shock. The companion interval Δt_2 is not correspondingly limited; it continues to increase after $\Delta t_1 = 0$. The sum $\Delta t_1 + \Delta t_2$ therefore departs from constancy as soon as the wavelets included in Δt_1 form a shock.

The conclusion that the amplitude density does not change prior to shock formation would seem to be at odds with the results of Rudenko and Chirkin, who find that the amplitude density of an originally narrowband Gaussian noise changes over arbitrarily small distances. The discrepancy is only apparent, however, not real. Rudenko and Chirkin deal with signals having arbitrarily large peak values (hence arbitrarily large slopes) so that shocks form immediately. Our method should be applicable to "clipped" signals with finite slopes, where the shock formation distance has a nonzero value.

APPENDIX C

MEASURED RANDOM FLUCTUATIONS IN SHORT-TERM SPL FOR TONE SIGNALS

As was mentioned in Chapter 4, considerable averaging was necessary to obtain the data presented in this report. Gusting winds and other inhomogeneous medium effects caused severe fluctuations in short-term sound pressure level. [By "short-term sound pressure level" we mean that the measurement averaging time is large compared to the period of the transmitted signal but small compared to the characteristic time of fluctuations caused by inhomogeneous medium effects.] We present here some recordings of the fluctuation in the short-term SPL as a function of time for several ranges. The experimental arrangement is the same as that used for the noise experiments. The input to the array for these measurements was, however, a sine wave of fixed frequency and amplitude. The amplitude was low enough that nonlinear effects were not important.

A typical set of measurements is shown in Fig. C-1. The ordinate is short-term SPL in a 50 Hz band (for all measurements reported here the filter was centered at the source frequency) and the abscissa is time. The quantity $2\theta_{HP}$ is the half-power (3 dB down) beamwidth of the source at the given source frequency. At 1.05 m the received level is nearly constant. At the two greater distances, however, there are significant fluctuations in level. Even though conditions were calm, peak to peak (p-p) fluctuations of 4 dB exist at 21.2 m. Figure C-2 shows data taken under windier conditions. Again the fluctuations are seen to increase with distance, becoming approximately 10 dB (p-p) at 18.3 m. Finally, measurements taken with a narrower beamwidth source are shown in Fig. C-3. In Fig. C-3a a plot of the long-term (30 sec) SPL versus range is shown. The solid curve is a prediction based on spherical spreading and atmospheric
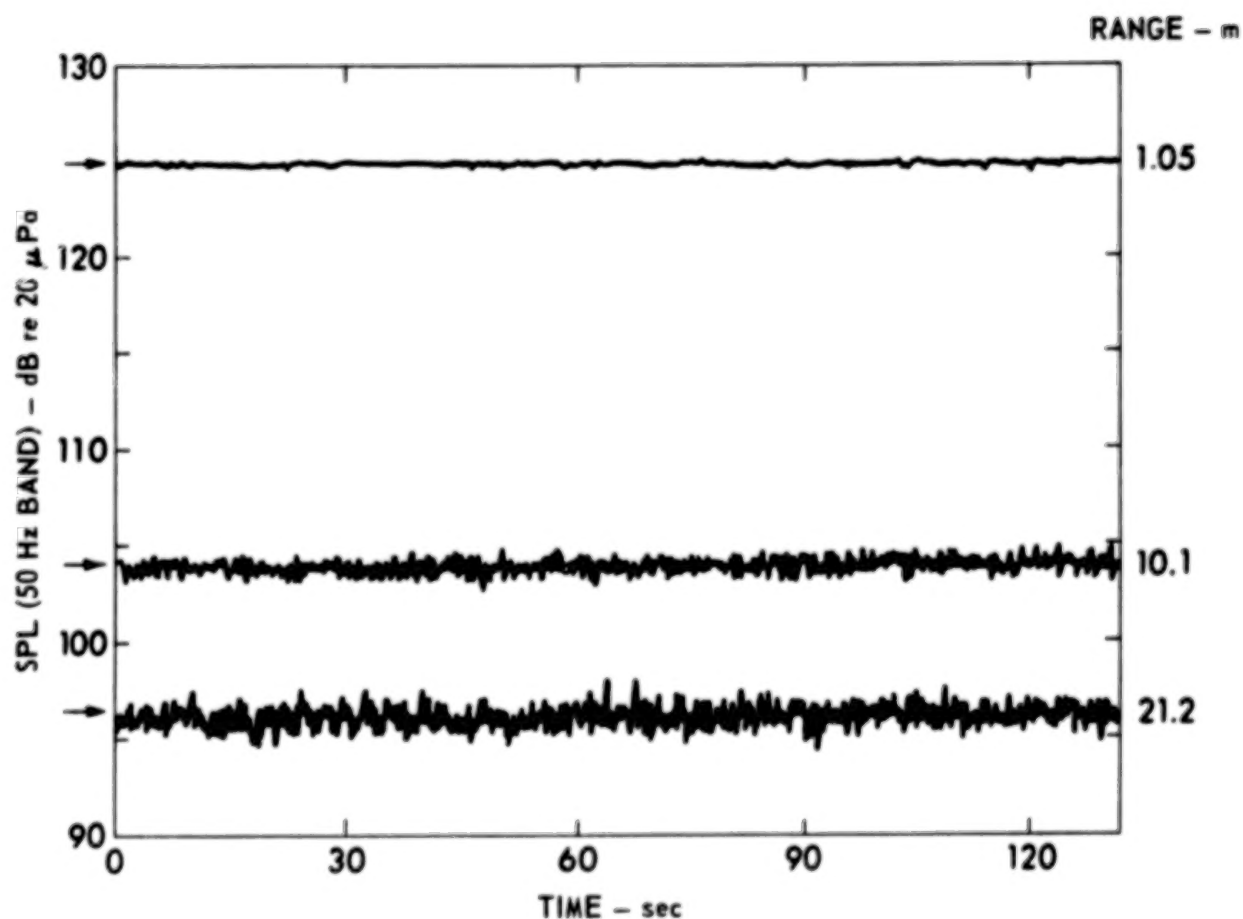
115

FIGURE C-1
MEASURED SHORT-TERM (87 msec) AVERAGE SPL AT VARIOUS DISTANCES
FROM AN 8.111 kHz SOURCE ($2\,\theta_{HP} = 16°$). THE ARROWS INDICATE LEVELS
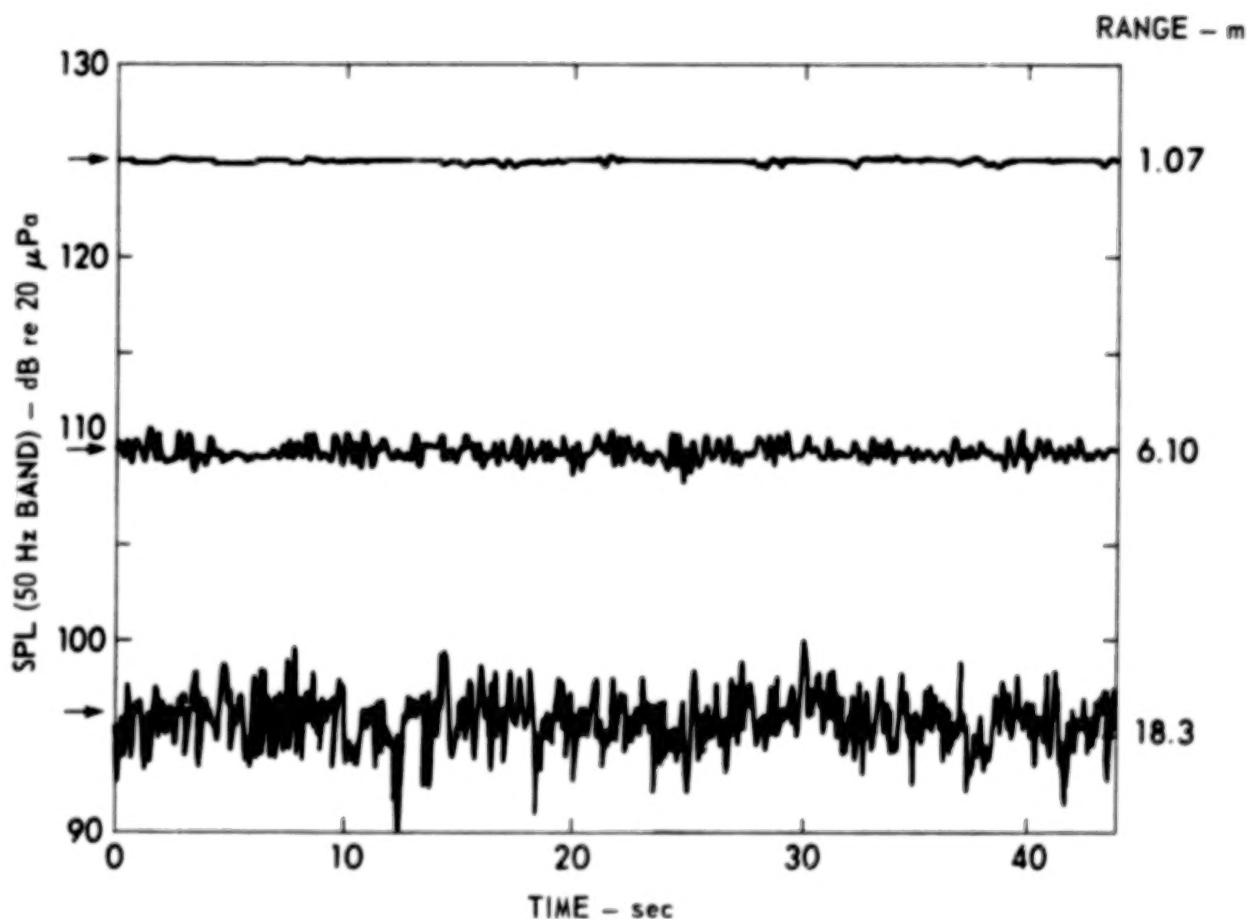PREDICTED FROM SPHERICAL SPREADING AND ATMOSPHERIC ABSORPTION.
CALM CONDITIONS

FIGURE C-2
MEASURED SHORT-TERM (87 msec) AVERAGE SPL AT VARIOUS
DISTANCES FROM A 6.45 kHz SOURCE (2 θ_{HP} = 21°).
THE ARROWS INDICATE 30 sec AVERAGE LEVELS.
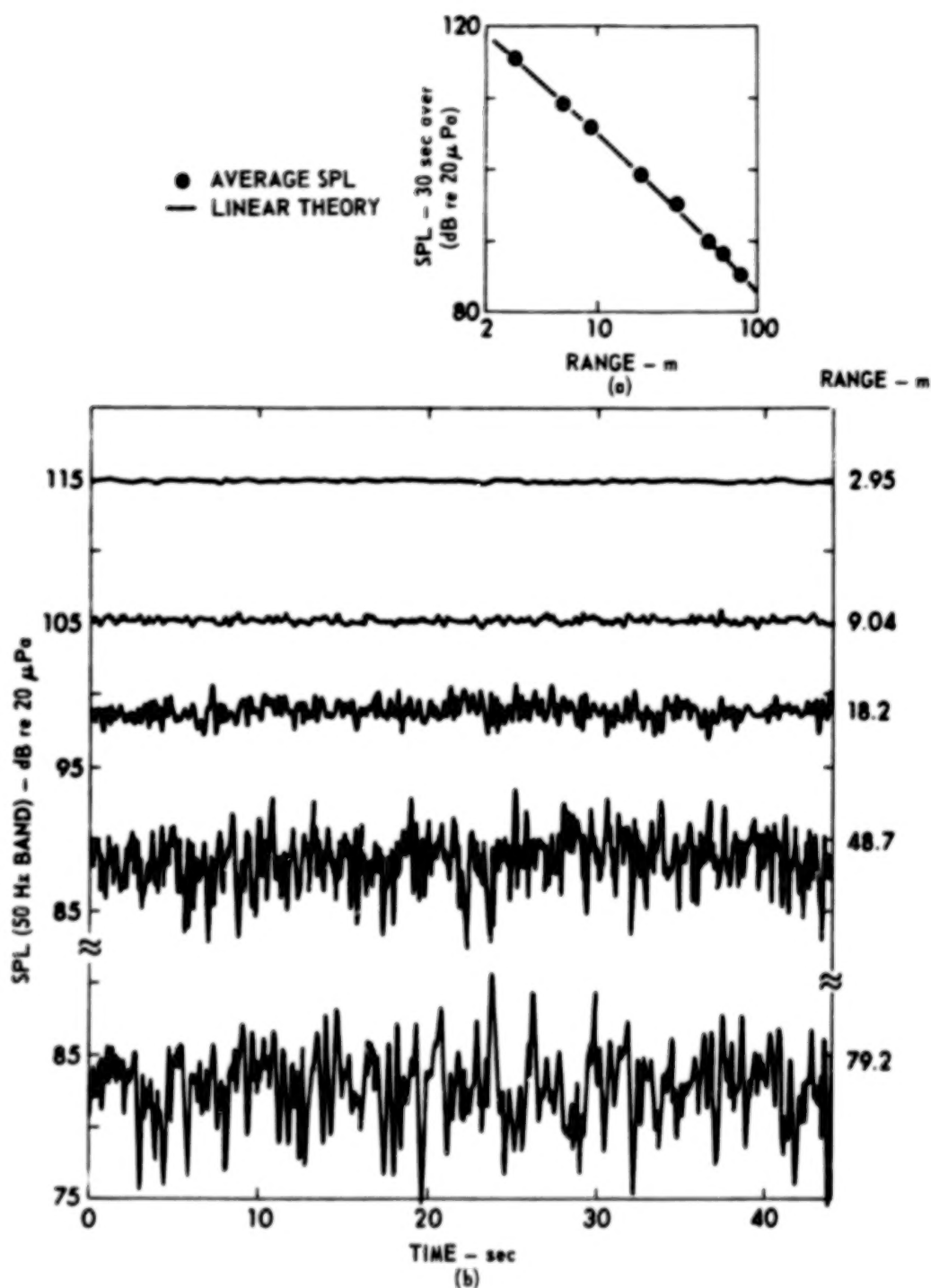WINDS GUSTING UP TO 20 km/h.

FIGURE C-3
(a) LONG-TERM AVERAGE (30 sec) SPL AS A FUNCTION OF RANGE.
(b) MEASURED SHORT-TERM (87 msec) AVERAGE SPL AT VARIOUS
DISTANCES FROM A 3.55 kHz SOURCE (2 $\theta_{HP} \doteq 8.8°$).
WINDS GUSTING TO 25 km/h

attenuation. In Fig. C-3b the fluctuations in level are shown at several ranges. Despite the fact that the fluctuations in level increase to approximately 17 dB (p-p) at the greatest distance, the 30 sec average levels (Fig. C-3a) are in excellent agreement with the linear theory curve. This observation is the basis for comparing our measured spectra with theoretical predictions for a homogeneous medium (see Chapter 5). In other words, if sufficient averaging times are used, a homogeneous medium theory seems to provide valid theoretical predictions for our experiments.

PROPAGATION EXPERIMENTS WITH TONES

In the course of evaluating the AEM array for use as a noise source, we made some propagation measurements with tone signals. The experimental arrangement was basically the same as that described in Chapter 4. The results given here were previously reported in Ref. 35.

The AEM array is a rectangular array composed of 20 individual square exponential horns, each driven by a separate 35 W horn driver. Each horn flares exponentially from a round throat 2.5 cm in diameter to a square mouth of side length 11.4 cm. The horn length is 35 cm. The horns are bolted together to form a 4 element by 5 element array with sides of 45.7 and 57.2 cm, respectively. The array is designed to be used as a fog horn. Its frequency response is approximately 250 Hz to 5400 Hz.

The results of six propagation experiments (AEM 5, 6, 1, and 2 in Table 4.1) for which the electrical input was a pure tone are shown in Figs. D-1 to D-6. The experiments were performed at three frequencies—1.5, 3.55, and 5.33 kHz—each corresponding to a relative peak in the array response. For each frequency, measurements were made at two different source levels, one 16-19 dB lower than the other. In each case the harmonic distortion components, as well as the fundamental, were measured as a function of propagation distance. The fundamental is identified by the symbol p_1, the second harmonic by p_2, and so on. Each solid curve is a linear theory prediction (spherical spreading and ordinary absorption). The effective source radius r_o was taken to be the first measurement distance greater than the Rayleigh distance $R_o(f_1)$, where f_1 is the transmitting frequency. See Table 4.1 for the actual values of $R_o(f_1)$ for each experiment. For values of the range r less than
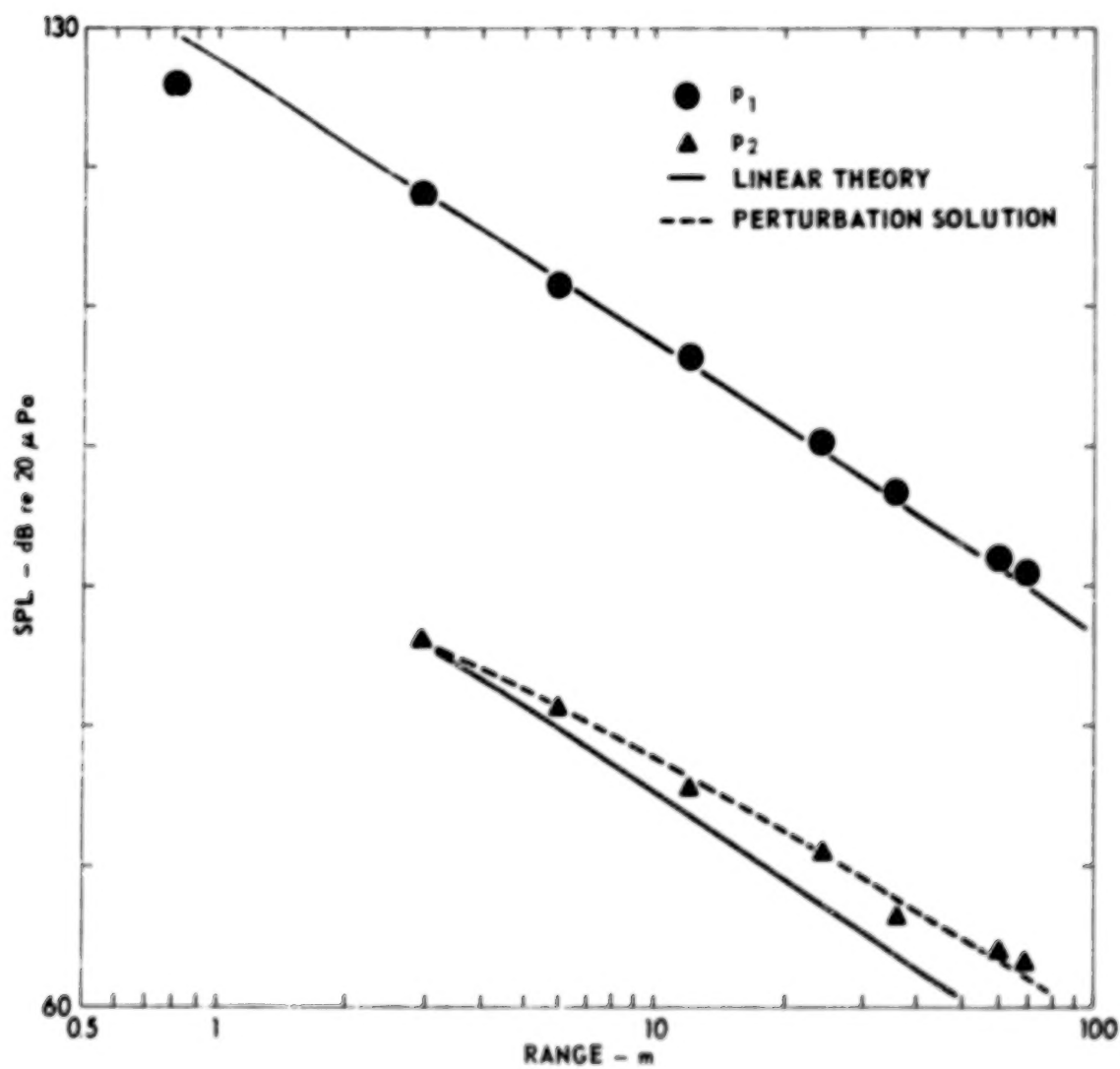
FIGURE D-1
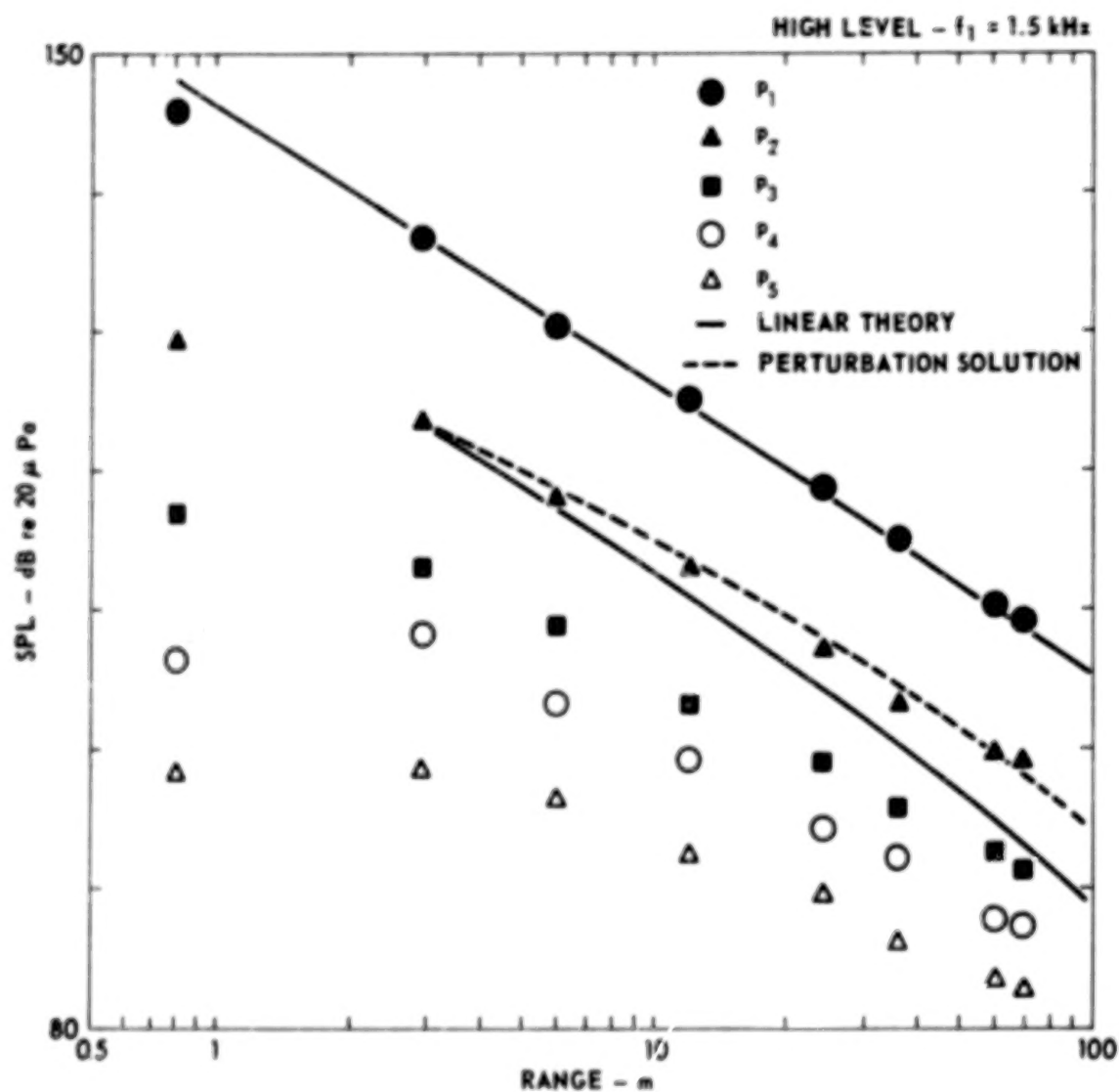PROPAGATION CURVES FOR AEM ARRAY
AEM5 (LOW LEVEL)
$f_1 = 1.5$ kHz

FIGURE D–2
PROPAGATION CURVES FOR AEM ARRAY
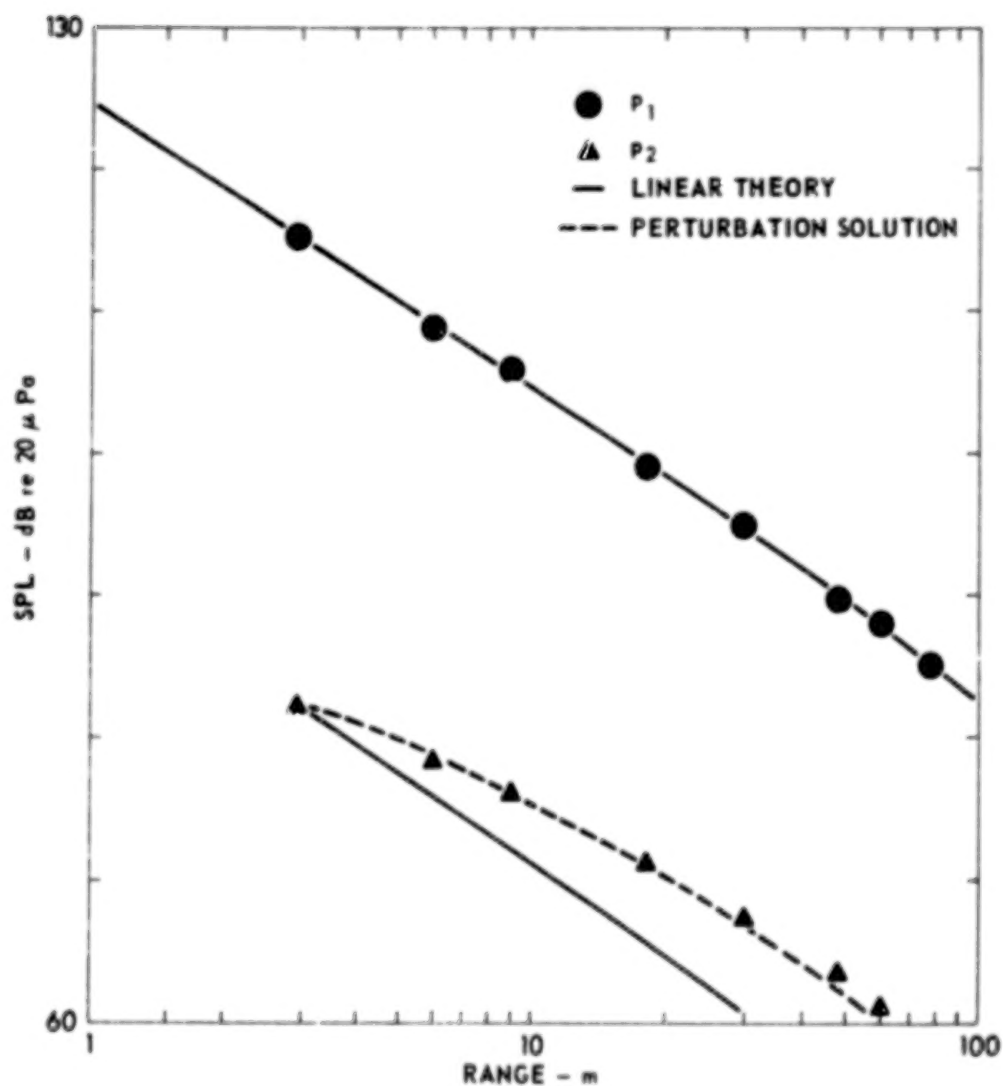AEM5 (HIGH LEVEL)
f_1 = 1.5 kHz

FIGURE D-3
PROPAGATION CURVES FOR AEM ARRAY
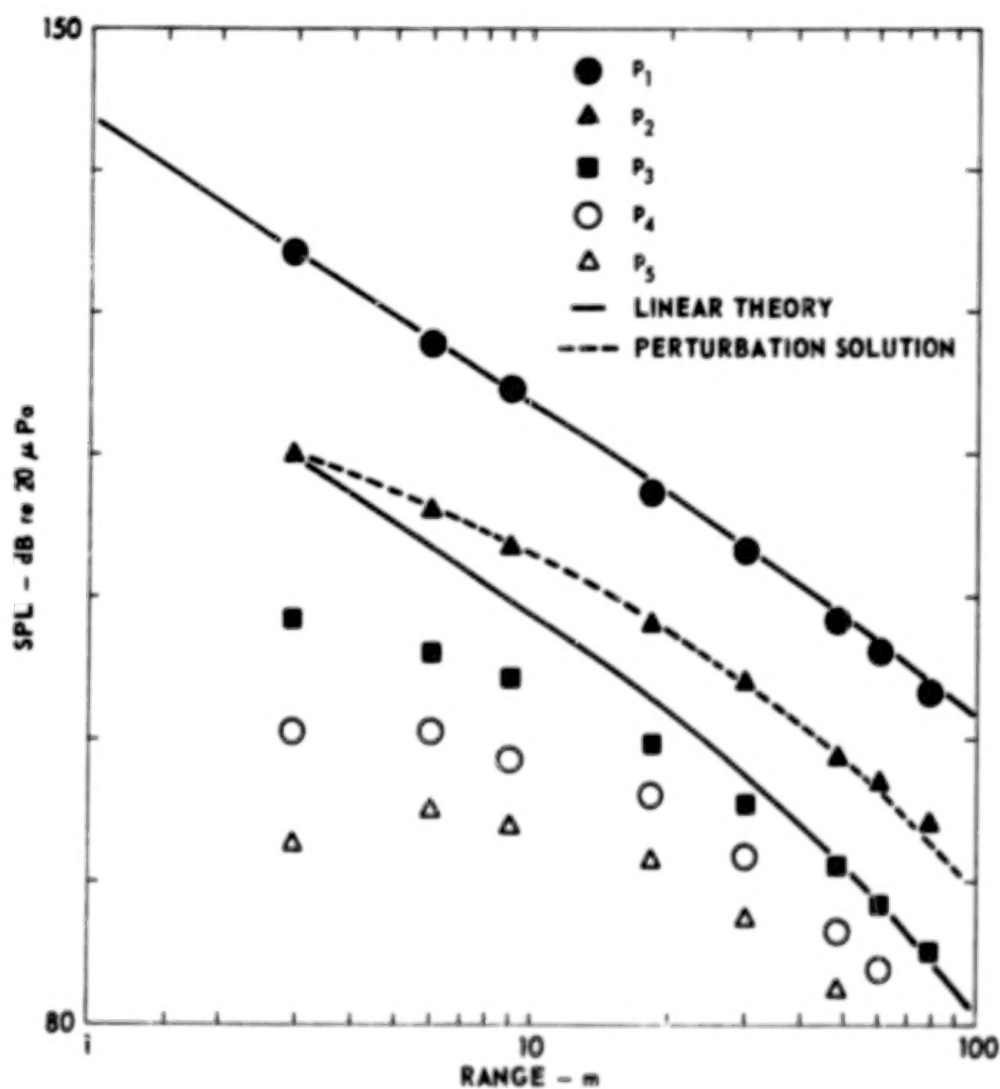AEM6 (LOW LEVEL)
$f_1 = 3.55$ kHz

FIGURE D-4
PROPAGATION CURVES FOR AEM ARRAY
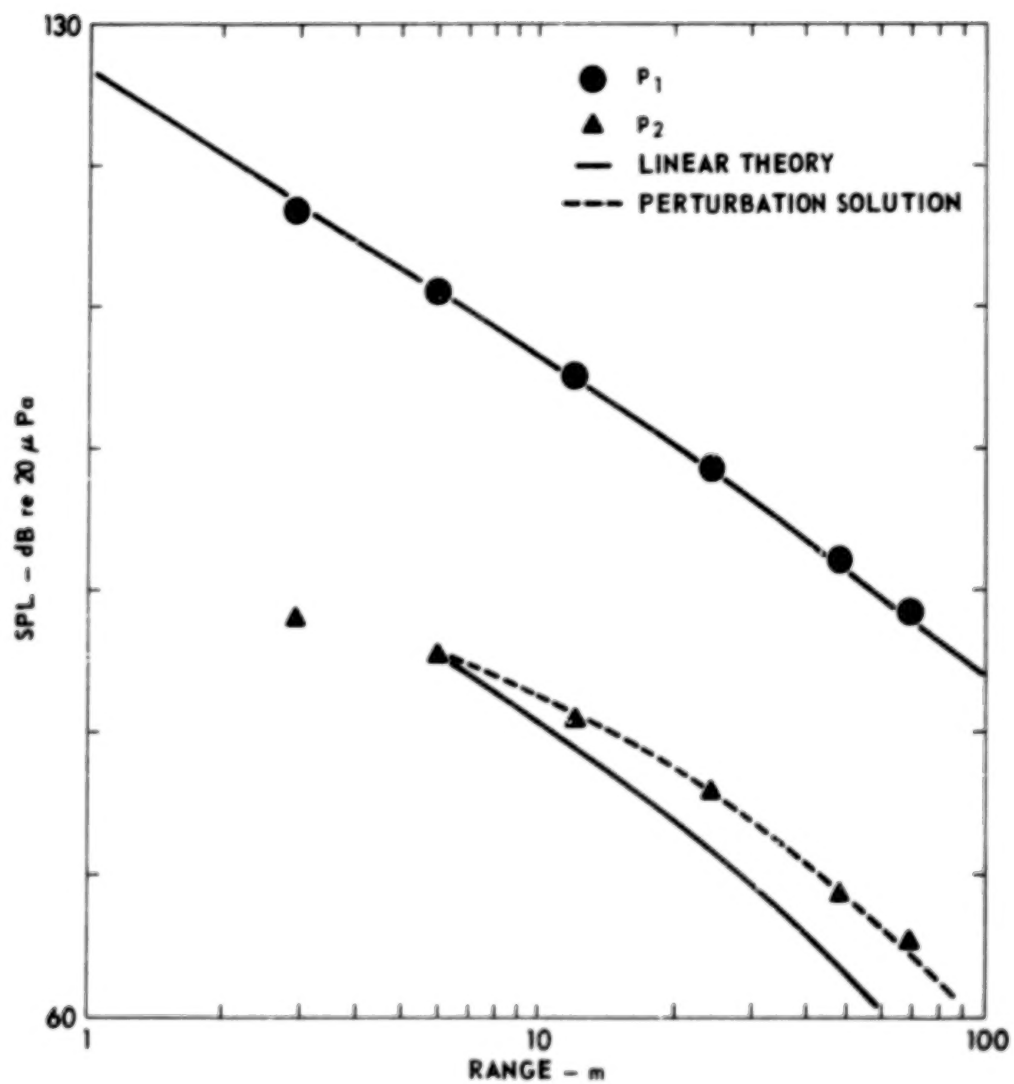AEM6 (HIGH LEVEL)
f_1 = 3.55 kHz

FIGURE D-5
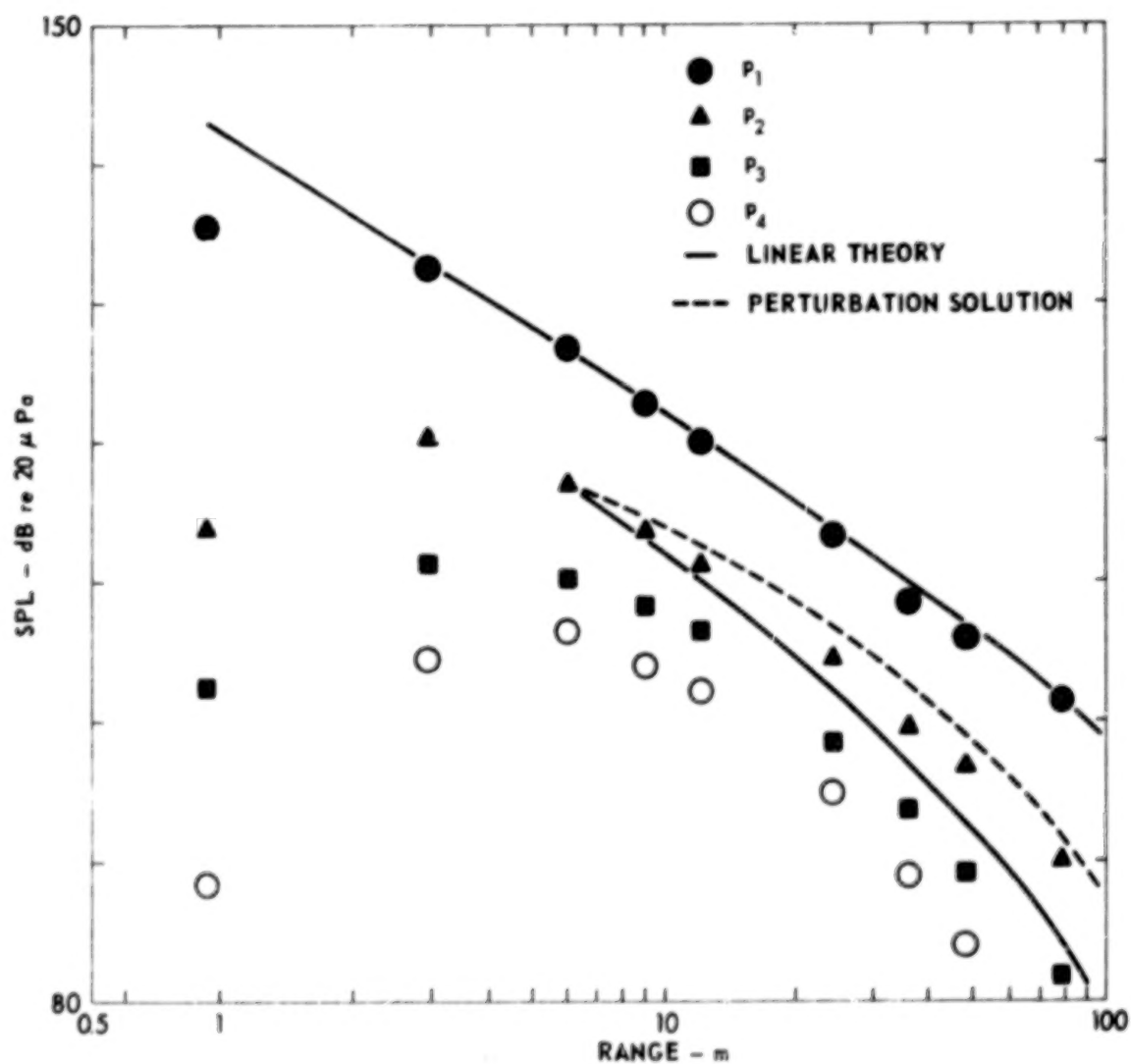PROPAGATION CURVES FOR AEM ARRAY
AEM1 (LOW LEVEL)
f_1 = 5.33 kHz

FIGURE D-6
PROPAGATION CURVES FOR AEM ARRAY
AEM2 (HIGH LEVEL)
$f_1 = 5.33$ kHz

R_o, the solid curve is an extrapolation of the farfield data. The dashed curves are predictions of the second harmonic amplitude based on a perturbation solution of Burgers' equation (Eq. A-21). The phase angle ϕ between the fundamental and second harmonic was taken to be zero. [The phase angle for the data in Fig. D-6 was measured and found to be approximately zero. Time waveforms were not measured for the data of Figs. D-1 to D-5.]

Three conclusions may be drawn from the data in these figures. First, for the low level tones, harmonic distortion is small. For the high level tones, however, many harmonics are generated along the propagation path and some are prominent. For example, in the high level test at 5.33 kHz, the second harmonic comes as close as 9 dB to the fundamental. Second, in all cases the measured value of p_1 was in good agreement with the linear theory prediction. These two results are not inconsistent. Only a small decrease in SPL of the fundamental (usually only a fraction of a decibel) is required to produce significant harmonic structure. Third, the second harmonic levels predicted from Eq. A-21 are in excellent agreement with the data in Figs. D-1 to D-5. The reason for the departure of the prediction from the measured data in Fig. D-6 may be that the signal is too intense to be handled with the second order perturbation analysis. Some additional discussion of this point is given below.

Typical time waveforms observed during the high level experiment at 5.33 kHz are shown in Fig. D-7. The progressive distortion of the wave with range is apparent. Referring to Fig. D-6, we see that the second harmonic has grown 13 dB relative to the fundamental over the propagation distance from 0.97 to 24.3 m. The asymmetry of the last three waveforms (sharp peaks, rounded troughs) is common and is caused by diffraction effects (see Ref. 1 or Chapter 2).
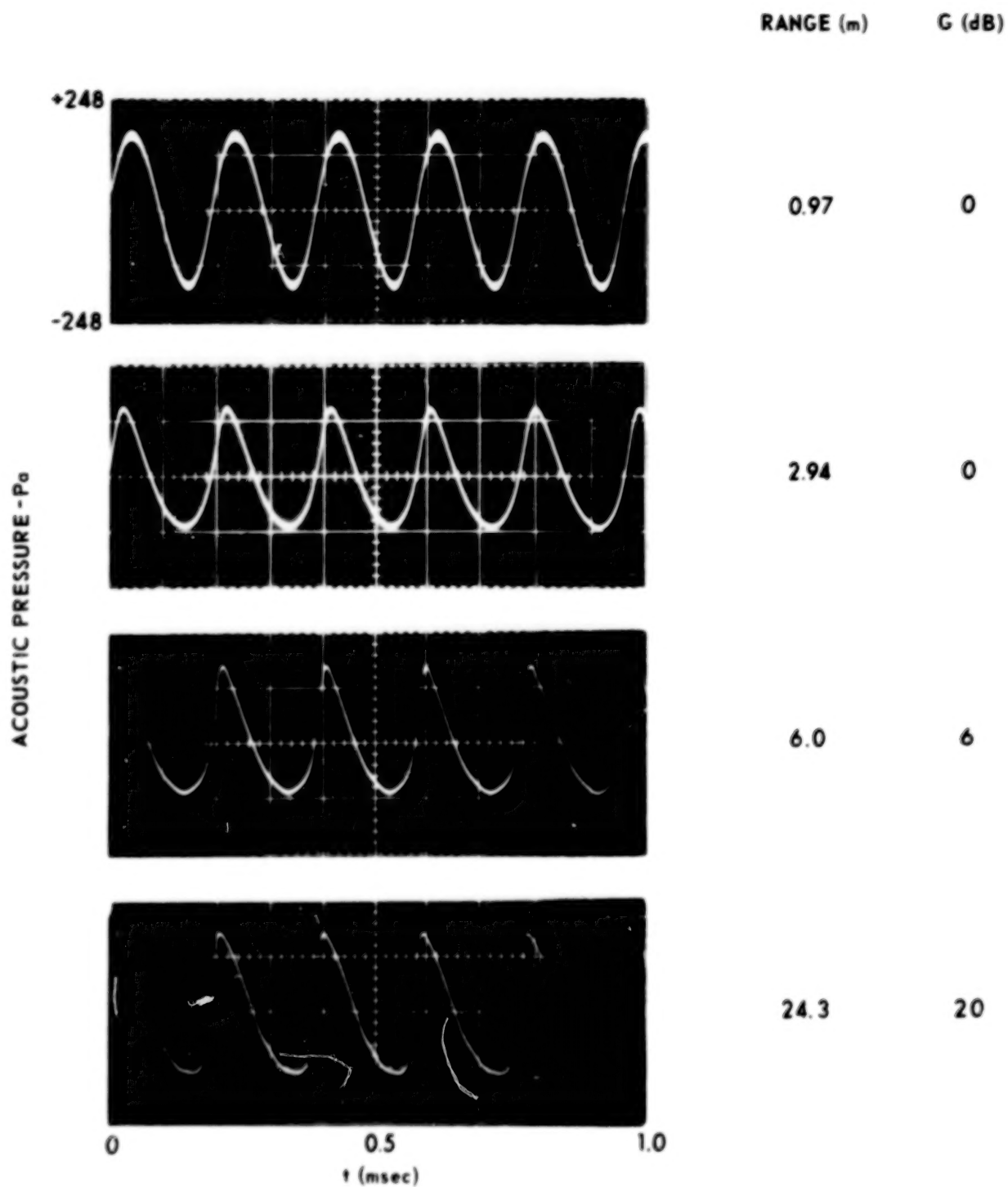
FIGURE D-7
MEASURED TIME WAVEFORMS FOR f = 5.33 kHz,
EXPERIMENT AEM2. G STANDS FOR OSCILLOSCOPE GAIN.

An a priori estimate of the importance of nonlinear effects in the tone experiments may be found from the SFL chart shown in Fig. D-8 (see Chapter 2). The points shown were computed for the data given in Figs. D-1 to D-6. The position of the points below the lower curve is consistent with our finding that nonlinear effects did not cause much extra attenuation of the findamental component. Notice, however, that the point for the high level experiment at 5.33 kHz falls on the lower curve, which marks the threshold of conditions for moderate nonlinear effects. It is therefore not surprising that the second order perturbation solution failed to provide a good fit for the second harmonic data in Fig. D-6.

Beam patterns for the fundamental component were measured at a range of 18.2 m for both low and high level electrical input (Fig. D-9). In each case the measured levels were normalized with respect to levels on the array axis. The solid curve is the pattern (computer by using linear theory) for a rectangular piston of dimensions equal to those of the array. Three comments may be made about the beam pattern measurements. First, the measurements were most difficult near the pattern nulls, where slight deviations in the beam caused by atmospheric inhomogeneities led to large changes in the received level. Second, except for a slight asymmetry, both the low and high level data agree well with the computed patterns for the major lobe. Third, the beam patterns measured at low and high levels differ at most by only 1 dB. Because the maximum difference in the low and high level data would be expected to be less than the extra attenuation suffered on axis for the high level signal, which has already been found to be miniscule, we conclude that nonlinearity had little effect on the beam pattern of the fundamental component.
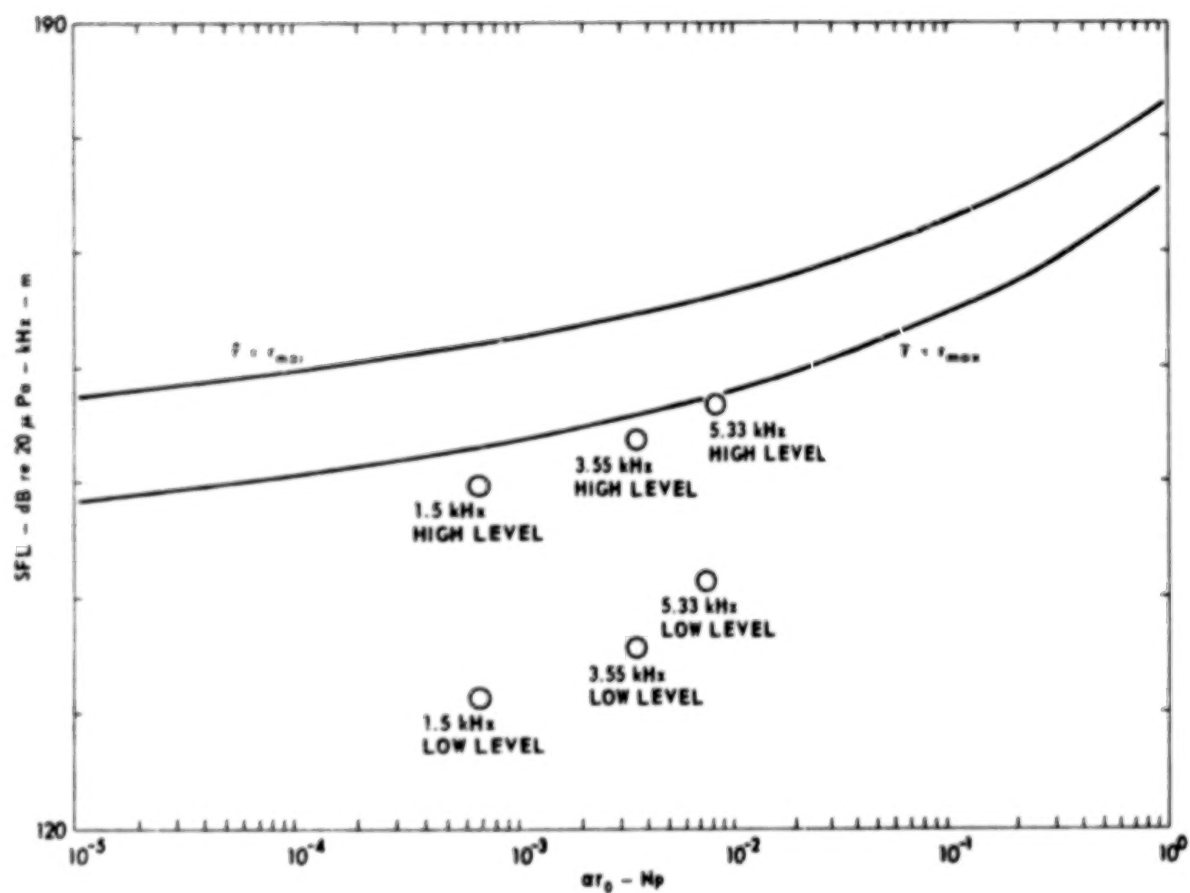
FIGURE D-8
DESIGN CURVE TO ASSESS THE IMPORTANCE OF NONLINEARITY
ON SPHERICAL WAVE PROPAGATION IN AIR

FIGURE D-9
MEASURED HIGH AND LOW LEVEL BEAM PATTERNS FOR
AEM ARRAY AT 5.33 kHz. SOLID CURVE IS COMPUTED
FOR A RECTANGULAR PISTON (LINEAR THEORY).
MEASUREMENTS TAKEN AT A RANGE OF 18.2 m.

In summary, high and low level tests with tones were carried out with the AEM array. Propagation, waveform, and beam pattern measurements were made. Although considerable harmonic distortion developed, little extra attenuation of the fundamental component occurred in the farfield. A theoretical prediction for the second harmonic, where applicable, was found to be in good agreement with measured data. Beam patterns (at the fundamental frequency) at low and high levels were found to be practically the same. Both of these experimental finds are consistent with a priori estimates of the importance of nonlinearity based on use of the SFL chart.

REFERENCES

1. M. A. Theobald, "Experimental Study of Outdoor Propagation of Spherically Spreading Periodic Acoustic Waves of Finite Amplitude," Technical Report ARL-TR-77-5, Applied Research Laboratories, The University of Texas at Austin (January 1977)(ADA 039 020). Also available as NASA CR-153396.

2. D. A. Webster, "Saturation of Plane Acoustic Waves and Notes on the Propagation of Finite-Amplitude Spherical Waves," Technical Report ARL-TR-77-4, Applied Research Laboratories, The University of Texas at Austin (January 1977)(ADA 035 694). Also available as NASA CR-154111.

3. D. F. Pernet and R. C. Payne, "Propagation of Finite-Amplitude Sound Waves in Tubes," Aero Report Ac 43, National Physical Laboratory, Teddington, England (November 1969).

4. D. F. Pernet and R. C. Payne, "Propagation of Finite-Amplitude Noise in Tubes," Aero Report Ac 48, National Physical Laboratory, Teddington, England (March 1971).

5. D. F. Pernet and R. C. Payne, "Non-Linear Propagation of Signals in Air," J. Sound. Vib. $\underline{17}$, 383-396 (1971).

6. F. M. Pestorius, "Propagation of Plane Acoustic Noise of Finite Amplitude," Technical Report ARL-TR-73-23, Applied Research Laboratories, The University of Texas at Austin (August 1973)(AD 778 868).

7. F. M. Pestorius and D. T. Blackstock, "Propagation of finite-amplitude noise," in Finite-Amplitude Wave Effects in Fluids, Proceedings of the 1973 Symposium, Copenhagen, edited by L. Bjørnø (IPC Science and Technology Press, Ltd., Guildford, England, 1974), pp. 24-29.

8. D. F. Pernet and R. C. Payne, "The Amplitude Distributions of Non-Linear Signals," Acoustics Report Ac 70, National Physical Laboratory, Teddington, England (January 1975).

9. O. V. Rudenko and A. S. Chirkin, "Nonlinear transformation of random wave-field spectra," Sov. Phys. Doklady $\underline{19}$, 64-66 (1974).

10. O. V. Rudenko and S. I. Soluyan, Theoretical Foundations of Nonlinear Acoustics, (Nauka Press, Moscow, 1975). English translation by R. T. Beyer (Plenum Publishing Corp., New York, 1977), Chapter 10.

11. O. V. Rudenko and A. S. Chirkin, "Statistics of discontinuous noise waves in nonlinear media," Sov. Phys. Dokl. $\underline{20}$, 748-750(1975).

12. K. A. Naugol'nykh and S. A. Rybak, "Spectrum of acoustic turbulence," Sov. Phys. JETP $\underline{41}$, 39-41 (1975).

REFERENCES (cont'd)

13. F. M. Pestorius, S. B. Williams, and D. T. Blackstock, "Effect of nonlinearity on noise propagation," in Proceedings, Second Inter-agency Symposium on University Research in Transportation Noise, North Carolina State University, 5-7 June 1974, edited by G. Banerian and W. F. Reiter, Vol. I, pp. 448-460.

14. D. T. Blackstock, "Nonlinear propagation distortion of jet noise," in Proceedings, Third Interagency Symposium on University Research in Transportation Noise, University of Utah, 12-14 November 1975, edited by G. Banerian and P. Kickinson, pp. 389-397.

15. S. A. Akhmanov and A. S. Chirkin, Statistical Phenomenae in Nonlinear Optics, (Izd. MGU, 1971, in Russian).

16. C. H. Allen and I. Rudnick, "A powerful high frequency siren," J. Acoust. Soc. Am. 19, 857-865 (1947).

17. C. H. Allen, "Finite Amplitude Distortion in a Spherically Diverging Sound Wave in Air," Ph.D. Dissertation, The Pennsylvania State University (1950).

18. Y. Shin, "Attenuation of Repeated Spherical Shock Waves," Technical Report No. 22, Department of Physics, University of California, Los Angeles, California (1963), (AD 413 346).

19. See, for example, J. A. Shooter, T. G. Muir, and D. T. Blackstock, "Acoustic saturation of spherical waves in water," J. Acoust. Soc. Am. 55, 54-62 (1974).

20. M. A. Theobald. D. A. Webster. and D. T. Blackstock, "The importance of finite-amplitude distortion in outdoor propagation experiments," in Abstracts, 7th International Symposium on Nonlinear Acoustics, Virginia Polytechnic Institute and State University, 19-21 August 1976, edited by A. H. Nayfek and J. E. Kaiser, pp 218-221.

21. H. M. Merklinger, R. H. Mellen, and M. B. Moffett, "Finite amplitude losses in spherical sound waves," J. Acoust. Soc. Am. 59, 755-759 (1976). These authors use the term "scaled source level" for the quantity we call SFL.

22. American National Standard Method for the Calculation of the Absorption of Sound by the Atmosphere ASA Standard S1.23 (1978) (Proposed ANSI Standard S1.26).

23. O. V. Rudenko, S. I. Soluyan, and R. V. Khokhlov, "Nonlinear theory of paraxial sound beams," Sov. Phys. Dokl. 20, 836-837 (1975). See also N. S. Bakhvalov, I. M. Zhileikin, E. A. Zabolotskaya, and R. V. Khokhlov, "An acoustic beam in a nonlinear medium," Proceedings of the 6th International Symposium on Nonlinear Acoustics, Moscow, 1975, R. Khokhlov, ed. (Moscow University Press, Moscow, 1976), Vol. I, pp. 88-96.

REFERENCES (cont'd)

24. D. A. Webster and D. T. Blackstock, "Finite-amplitude saturation of plane sound waves in air," J. Acoust. Soc. Am. 62, 518-523 (1977).

25. D. A. Webster and D. T. Blackstock, "Collinear interaction of noise with a finite-amplitude tone," J. Acoust. Soc. Am. 63, 687-693 (1978).

26. Instructions and Applications for 4138 Condenser Microphones, Brüel and Kjaer, Copenhagen, 1967.

27. M. H. Safar, "The propagation of spherical acoustic waves of finite amplitude in fresh and sea water," J. Sound Vib. 13, 1-7 (1970).

28. K. A. Naugol'nykh, "Propagation of spherical sound waves of finite amplitude in a viscous, heat-conducting medium," Sov. Phys. Acoust. 5, 79-84 (1959).

29. D. T. Blackstock and J. G. Willette, "The Effect of Nonlinear Propagation Distortion on High-Power, Low-Frequency Sonars" (U), Technical Report ARL-TR-71-11, Applied Research Laboratories, The University of Texas at Austin (29 March : 71), Appendix. CONFIDENTIAL

30. A. L. Thuras, R. T. Jenkins, and H. T. O'Neil, "Extraneous frequencies generated in air carrying intense sound waves," J. Acoust. Soc. Am. 6, 173-180 (1935).

31. D. T. Blackstock, "Nonlinear Acoustics (Theoretical)," in Amer. Inst. Phys. Handbook, 3rd edition, D. Gray, ed. (McGraw-Hill Book Co., Inc., New York, 1972), pp 3-183 to 3-205.

32. D. T. Blackstock, "Connection between the Fay and Fubini solutions for plane sound waves of finite amplitude," J. Acoust. Soc. Am. 39, 1019-1026 (1966).

33. I. Rudnick, "Measurements of the Attenuation of a Repeated Shock Wave," Technical Report No. 3, Soundrive Engine Company, Los Angeles, California (1953).

34. M. Abramowitz and I. Stegun, Handbook of Mathematical Functions, National Bureau of Standards Applied Mathematics Series 55, (U. S. Government Printing Office, 1964).

35. D. A. Webster, D. E. Alexander, and D. T. Blackstock, "High power tests of AEM array," Supplement to E. L. Hixson and H. L. Kuntz, "A study of broad band high level audio systems," Quarterly Progress Report for Contract DOT-CG-63441-A, U.S. Coast Guard (October 1977).

1. Report No. NASA CR-2992	2. Government Accession No.	3. Recipient's Catalog No.
4. Title and Subtitle EXPERIMENTAL INVESTIGATION OF OUTDOOR PROPAGATION OF FINITE-AMPLITUDE NOISE		5. Report Date August 1978
		6. Performing Organization Code
7. Author(s) Don A. Webster David T. Blackstock		8. Performing Organization Report No. ARL-TR-78-31
		10. Work Unit No.
9. Performing Organization Name and Address Applied Research Laboratories The University of Texas at Austin PO Box 8029 Austin, TX 78712		11. Contract or Grant No. NAS1-14160
		13. Type of Report and Period Covered Contractor Report
12. Sponsoring Agency Name and Address National Aeronautics and Space Administration Langley Research Center Hampton, VA 23665		14. Sponsoring Agency Code

15. Supplementary Notes

Langley Technical Monitor: John M. Seiner

Final Report

16. Abstract   Experiments on the propagation of finite-amplitude noise outdoors have been
made. These experiments constitute Phase II of a research program to study outdoor prop-
agation of finite-amplitude acoustic waves. The intended application is to aircraft noise.
In this report Phase I, which was done with intense tones, is first reviewed. Eleven
noise experiments and associated theory are then discussed. The source, a conventional
electroacoustic transmitter, was mounted on the ground and pointed upward in order to avoid
ground reflection effects. The propagation path was parallel to a radio tower 85 m tall,
whose elevator carried the receiving microphone. The source emitted broadband, octave
band, or 1/3 octave band noise in the frequency range 2-10 kHz. Source level was in the
range 121-145 dB re 20 μPa at 1 m. The measurements were compared with predictions based
on linear theory. The linear theory model included spherical spreading, atmospheric
attenuation, and, if appropriate, source diffraction. The observations and conclusions
are as follows: (1) At the higher source levels nonlinear propagation distortion caused
a strong generation of high frequency noise over the propagation path. For example, at
70 m for a frequency 2-3 octaves above the source noise band, the measured noise was up
to 30 dB higher than the linear theory prediction. (2) The generation occurred in both
the nearfield and the farfield of the transmitter. (3) At no measurement point was small-
signal behavior established for the high frequency noise. Calculations support the
contention that the nonlinearly generated high frequency noise never becomes small-signal
in its behavior, regardless of distance. (4) When our measured spectra are scaled in
frequency and level to make them comparable with spectra of actual jet noise, our spectra
are found to be well within the jet noise range. It is therefore entirely possible that
nonlinear distortion affects jet noise.

17. Key Words (Suggested by Author(s)) Noise Nonlinear acoustics High-intensity sound Outdoor propagation Spectral distortion Spherical waves	18. Distribution Statement UNCLASSIFIED- Unlimited Subject Category 71

19. Security Classif. (of this report) UNCLASSIFIED	20. Security Classif. (of this page) UNCLASSIFIED	21. No. of Pages 138	22. Price* $7.25

90

50

END